Universidad Autónoma de Madrid

Chemical Reactions on Metallic Surfaces

Dissertation for the Degree of Doctor of Physical Science
Department of Condensed Matter Physics

Luigi Terracciano
Madrid, July 2015

Abstract

The properties of molecular and hybrid nanostructures on surfaces are strongly influenced by intermolecular and molecule-surface interactions. This thesis contributes to a deeper understanding of the role they play in the formation of molecular complexes focusing on the structural, electronic and catalytic properties of the resulting nanostructures. By means of Variable Temperature Scanning Tunneling Microscopy and X-ray Photoemission Spectroscopy, we have conducted experiments in three different field of surface science.

In the first part, it will be studied distinct supramolecular structures obtained by intermixing of organic acceptor molecule, with two different nature donor species: one organic molecules and one metallic element. A dissertation on supramolecular self-assembly, coordination networks and charge transfer complexes on a noble metal surface will be exposed.

Then, will be discussed and analyzed the results obtains on the heteroepitaxial growth of metals. It will be studied the mechanisms underlying the growth as well the thermodynamical and kinetic aspects that influence it. On the other hand we observe a modification of the metal growth behavior in presence of a pre-adsorbed molecular layer, which play an active role in the process.

Last experiments involve the chemical reactions of organic molecules using the surface itself as a catalyst. The organic surface chemistry represents an innovative method to obtain large organic molecules covalently connected each other via bottom-up approach. Such structures present several advantages with respect to the weak-bond supramolecular strucutes held together by no-covalent forces.

Resumen

Las propiedades de nano estructuras moleculares y hibridas están fuertemente afectadas por interacciones intermoleculares y interacciones moléculas-substrato. Esta tesis contribuye a un más profundo conocimiento del papel jugado de dichas interacciones en la formación de complejos moleculares, enfocándose en las propiedades estructúrales, electrónicas y catalíticas de las nanoestructuras así formadas. Mediante *Variable Temperature Scanning Tunneling Microscopy* and *X-ray Photoemission Spectroscopy*, hemos llevado al cabo experimentos sobre tres distintos campos de investigación de la ciencia de las superficies.

En la primer parte, se estudiará diferentes estructuras supramoleculares obtenidas mesclando una molécula orgánica aceptora de electrones con dos especies donoras de distintas natura: una es otra molécula orgánica, la otra es un elemento metálico. Una disertación sobre el autoensamblaje supramolecular, redes de coordinación y complejos de transferencia de carga estará bien discutida.

Luego se discutirán y analizarán los resultados obtenidos en el crecimiento heteroepitaxial de los metales. Se estudiarán además los mecanismos por debajo del crecimiento y los aspectos termodinámicos y cinéticos que influyen en las modalidades de crecimiento.

Los últimos experimentos involucran las reacciones químicas se moléculas orgánicas usando la superficie misma como catalizador. La química orgánica en superficies representa un nuevo y innovador método para obtener grandes molákulas covalentemente enlazadas entre sí mismas con estrategia *bottom-up*. Estas estructuras presentan muchas ventajas con respecto a las estructuras supramolecular estabilizadas con débiles fuerzas no covalentes.

Contents

1 Introduction **1**

2 Experimental setup and techniques **3**
2.1 Scanning Tunneling Microscopy (STM) 3
2.1.1 STM working principle 3
2.1.2 Theory of the STM 5
2.2 X-ray Photoelectron Spectroscopy (XPS) 7
2.2.1 XPS working principle 7
2.2.2 Physics with XPS 9
2.3 TIREMISU UHV System 11
2.4 The Au(111) reconstructed surface 14
Bibliography 16

3 Charge transfer through organic and hybrid structures on Au(111) 19
3.1 Introduction 19
3.2 Organic acceptor molecule: TCNQ on Au(111) 20
3.3 2D-Metal Organic Coordination Network 24
3.3.1 MOCN: TCNQ+Fe on Au(111) 24
3.4 2D-Charge Transfer complexes 29
3.4.1 Organic donor molecule: TTF on Au(111) 30
3.4.2 Charge transfer complex TTF-TCNQ on Au(111) 33
3.5 Discussion 39
3.6 Conclusions 43
Bibliography 45

4 Modification of metallic growth on Au(111) surface. 51
4.1 Introduction to heteroepitaxial growth 51
4.2 Growth of Fe on Au(111) 55
4.2.1 Thermodynamic and kinetic effects 57
4.2.2 Structural phase transition 64
4.2.3 Effect of annealing 65
4.3 Growth of Fe on Au(111) precovered with TCNQ monolayer . . . 71
4.4 Conclusions 79
Bibliography 81

5 Organic Surface Chemistry: two examples on Au(111) 87
5.1 Introduction 87
5.2 The polyester condensation 88
5.2.1 TPB and TMC molecules 90
5.2.2 Formation of Surface Covalent Organic Frameworks . . . 91
5.3 Carbon homo and hetero atom bonds 95
5.3.1 Hierarchical organic reactions on Au(111) 97
5.3.2 Glaser coupling vs Huisgen cycloaddition 101
5.3.3 Discussion 105
5.4 Conclusion 108
Bibliography 109

6 Summary 113

Conclusiones Generales 117

Chapter 1

Introduction

Technological progress is key to improving world living standards as shown by the work of Nobel laureate Robert Solow in 1987. Nowadays we live in an increasingly technological world with electronic devices occupying a central part of our lives. The fabrication methods of silicon-based microelectronics have been refined to produce ever smaller devices and has solved many of the challenges associated with our increased use of high-performing electronic devices, but will soon reach their fundamental limits.

A promising alternative route to even more technological devices is represented by organic materials. In fact, the ability of chemists to design, manipulate and synthesize new molecules with specific properties makes possible to create structures with novel characteristics impossible to replicate with silicon. The potential applications span a broad range of fields, including medicine and biomedical research, environmental health, information and communications. Because of their lower cost and higher throughput manufacture, carbon-based electronic devices also hold the potential to expand our electronic world in ways unimaginable when Moore made his famous prediction about the density of chips as function of time. In fact these small molecules and polymers represent systems with nanometre dimensions which open the new field of *Nanotechnology*. Commonly accepted definition of nanotechnology is the manipulation of matter with at least one dimension sized from 1 to 100 nanometers, the quantum-realm scale.

To fabricate and then integrate organic or hybrid nanomaterials into electronic devices, a detailed knowledge the physics of these systems at such low dimensionality is necessary . In particular, detailed knowledge about both the

connections among the molecules and the interaction with the supporting substrate, is required to tailor the properties of the molecular devices. Electronic, optical and magnetic bulk properties of these new material, in fact, are greatly influenced at the interface and in particular to metal interface where the electric signal has to be collected.

In this thesis we present experimental studies in different specific field of the surface science. The systems will be investigated with high-resolution STM under ultra-high vacuum (UHV) conditions. The STM results will be supported by X-Ray photoelectron spectroscopy (XPS), which will provide a complete a complementary investigation of geometrical and electronic properties.

Within this scenario, this thesis is organizing as follow:

Chapter 2 provides a brief introduction to scanning tunneling microscopy (STM) and X-ray photoelectron spectroscopy (XPS). Also the experimental set-up used in this thesis will be described.

Chapter 3 is focused on the study of charge transfer in different supramolecular structures obtained by intermixing of organic acceptor molecule with two different donor species. One specie is a metallic element, which leads to the self-organization of extended Metal-Organic Coordination Network (MOCN). The other specie is another organic molecule which exhibits a strong donor character.

Chapter 4 is devoted to the study of heteroepitaxial growth of thin films on natural templated metal substrates. The possibility to control the morphology of thin films by changing the deposition parameters and mediating the growth with organic specie will be analyzed.

Chapter 5 is centered to the study of chemical reactions that relatively complex organic adsorbates can undergo on metallic surfaces, in particular to the role of the reactivity of surfaces that can promote or hinder some specific and well know reactions in gas phase.

Chapter 6 summarizes the results presented in this thesis.

Chapter 2

Experimental setup and techniques

In this chapter we will describe the setup used in the course of this work to carry out the experiments. Before we will give a brief discussion of the main techniques used: Scanning Tunneling Microscopy (STM) and X-ray Photoelectron Spectroscopy (XPS). The combined STM+XPS approach allows us a deeper comprehension of experimental data since they provide a full characterization from geometric and electronic point of view respectively of the physical processes under investigation.

2.1 Scanning Tunneling Microscopy (STM)

The STM is a well-established technique to investigate structures and morphologies of metal surfaces in real space with atomic resolution. It was developed in 1981 by G. Binning and H. Rohrer [1] leading them to the Nobel Prize in Physics in 1986 "for their design of the scanning tunneling microscope" [2].

2.1.1 STM working principle

The working principle of the STM is based on the quantum mechanical tunneling effect. A very sharp metallic tip is approached towards a metallic surface and kept a distance of few Ångströms (typically 5-10 Å) (fig. 2.1(a)). The application of a potential difference between the tip and the sample results

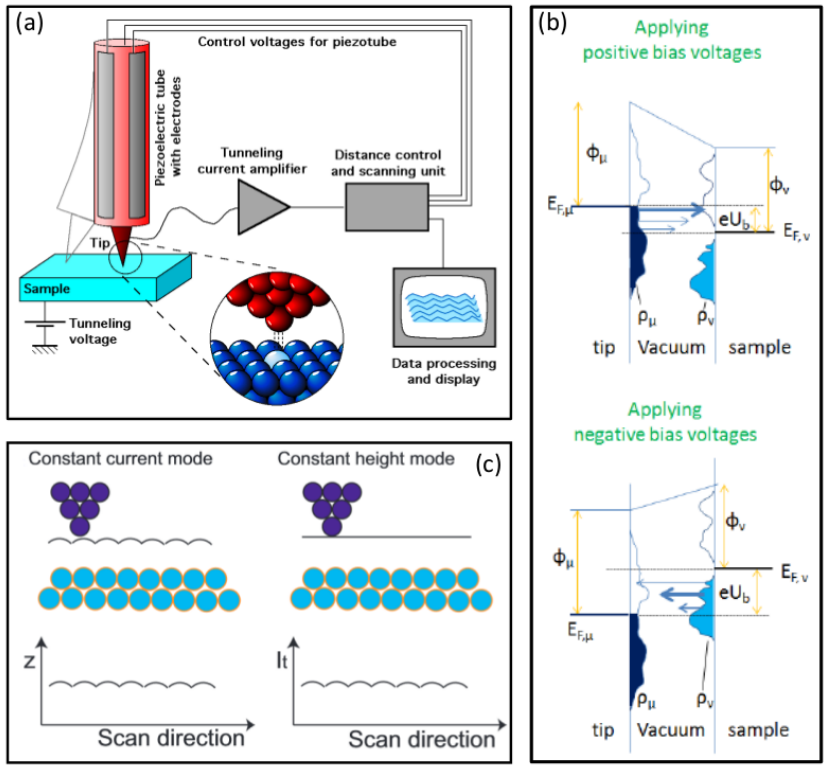

Figure 2.1: *(**a**)Scheme of the working mechanism of an STM (image from Wikipedia). The movements of the XY scanning piezos and the vertical Z height are controlled by a computer; (**b**) Energy diagram of the tunnel effect between tip and sample applying a different sign bias voltage; (**c** Constant current and constant height scanning modes)*

in the flow of a small tunneling current through the vacuum barrier that decay exponentially with the tip-surface distance z [3]. If the bias voltage (U_b) applied to the sample is positive, electrons from occupied states of the tip up to its Fermi level ($E_{F,\mu}$) tunnel into empty states of the sample in an energy window between ($E_{F,\nu}$) and $E_{F,\nu} + eU_b$. With a negative bias voltage the tunneling direction is inverted and electrons tunnel, in this case, from the occupied states of the surface towards the tip [4] (fig. 2.1(b)). The tip scans the surface along the X and Y direction, both within the surface plane. The fine in-plane movements of

the tip is achieved with piezo-electric materials which expand and contract by applying a voltage and can thus position the tip precisely over the surface[5]. Different measuring modes exist. In the constant current mode the feedback loop adjusts the distance between the tip and the surface at each point for keeping constant an initial tunneling current value. The record of the feedback signal applied to the z-direction piezo as a function of the tip lateral position results in a a map of the surface topography. An alternative scanning mode is the so-called constant height mode. In this case bias voltage and tip-sample distance are kept constant during the two-dimensional scan (fig. 2.1(c)). The variations observed in the tunneling current represent the surface image. For this mode it is necessary to have a flat surface otherwise the tip might crush into steps or impurities.

2.1.2 Theory of the STM

According to the generalized Tersoff-Hamann model of an STM tunneling junction with a spherical tip [6] based on Bardeen formalism [7], the current flowing between the two electrodes in first-order perturbation theory can be expressed as:

$$I \propto \frac{4\pi e}{\hbar} \exp^{-2kz} \int_{E_F}^{E_F+eU_b} \rho_\mu(E - eU_b)\rho_\nu(E)T(E, eU_b)\, dE \qquad (2.1)$$

where $k = \sqrt{2m\Phi_{eff}}/\hbar$ is the inverse decay length inside a vacuum barrier with Φ_{eff} local work function, ρ_μ and ρ_μ represent, respectively, the tip and surface density of states and $T(E, eU_b)$ is a transmission coefficient. In a first approximation, reasonable for small bias, we can assume constant ρ_μ and T. Within this assumption the tunneling current depends mainly on tip-sample distance and the density of surface states[1].

The adsorption of molecules on metallic substrate modifies their electronic structure depending on the nature of the molecules-substrate interactions [8] as shown in figure 2.2 In gas phase, the quantized energy levels in consist in δ resonances at determined energy values, and the molecules are characterized by a HOMO-LUMO gap (fig. 2.2a). Scanning at energies close to their Fermi levels no tunneling current should appears, since no tunneling of electrons would occur inside the gap and the molecules will appears transparent to the tip. However, the interaction with the surface broadens the molecular levels and results in

[1] Usually the transmission coefficient is expressed as $T(z, E, eU_b) = T(E, eU_b) \times \exp^{-2kz}$. Here we have separated the terms in order to explicit such approximation

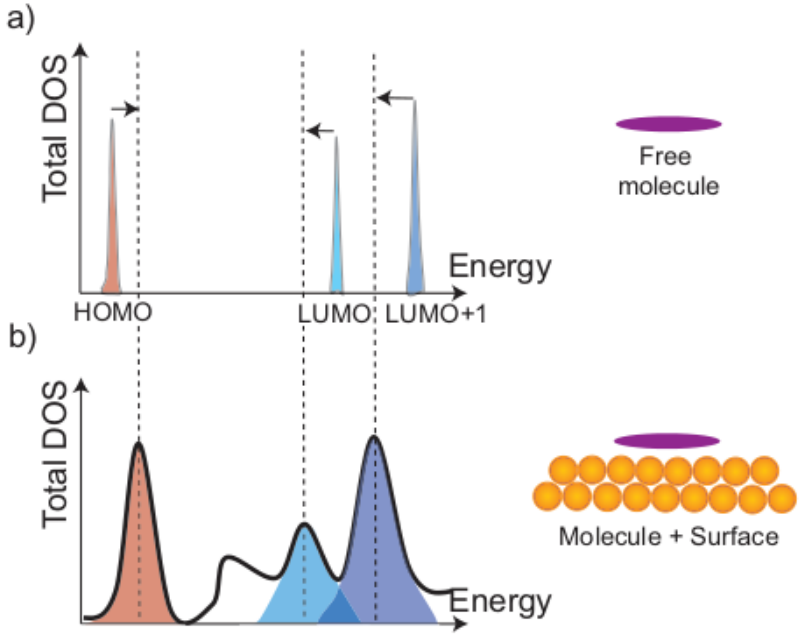

Figure 2.2: *(**a**)Molecular orbitals of molecules in gas phase consist in δ resonances. (**b**)When deposited on a surface the molecular levels shift by charge transfer processes and broaden due to interaction with the substrate*

the formation of extended tails that contribute to tunneling process at energies close to E_F (fig. 2.2b). In consequence, molecules can be imaged as featureless protrusions by the STM image close to E_F. When the eU_b applied between tip and surface reaches the energy of the orbital we are scanning, the topography image may show intramolecular resolution. Therefore, STM images are not a pure topography map but include also electronic information of both the molecule and the underlying surface. In cases of weakly adsorbed molecules, the resonant tunneling through the HOMO/LUMO becomes the predominant contribution to the current and the topography image resemble the spatial shape of the free-molecules orbitals[9].

On the other hand we have to keep in mind that the orbitals have no physical meaning and they are not observable physical quantities. In fact an orbital is wavefunction solution of Schröedinger equation whose modulus squared repre-

sents a probability[2], that is not a observable physical quantity such as momentum or position. What physically STM does is to remove or inject electrons in the real system depending on the sign of the voltage bias U_b. Electrons tunnel through the vacuum when there is a resonance between potential difference tip-sample and an ionization potential of the sample. Therefore STM image represents isopotential ionization surface $V(x, y) = U_b = const.$ In Hartee-Fock theory, Koopmans' theorem states that the difference between the energy of ionized molecules obtained removing (injecting) an electron from (to) orbital ψ_i and the energy of neutral molecules is equal to $-\epsilon_i$, the negative of the respective orbital energy [10]. It means that the energy (eU_b) of first ionization is equal to the energy of HOMO (LUMO), the energy of second ionization is equal to HOMO-1 (LUMO+1),.... From this equivalency between energy of ionization and energy of orbitals, we can can say that STM images represent molecular orbitals.

2.2 X-ray Photoelectron Spectroscopy (XPS)

The X-ray Photoelectron Spectroscopy (XPS), also known as Electron Spectroscopy for Chemical Analysis (ESCA), is a powerful technique to investigate the chemical composition of the surface. It was developed by Kay Siegbahn and his research group in the mid-1960. In the 1981 Siegbahn was awarded the Nobel Prize in Physics "for his contribution to the development of high-resolution electron spectroscopy" [11].

2.2.1 XPS working principle

The working principle of XPS is based on the photoelectric effect which was first detected by Hertz in 1887 and explained by Einstein in 1905. When a surface is illuminated with photons, an electron may absorb all its energy and be able to escape the solid (photoemitted electron), as schematically depicted in fig. 2.3(a). Therefore photoemission spectroscopy is employed to monitor the occupied levels.
The cross section for the photo-ionisation process is given by[12]

$$\sigma \propto \sum_f \left| \langle f | \hat{\mathbf{A}} | i \rangle \right|^2 \delta(\hbar\omega + E_i - E_f) \tag{2.2}$$

[2]the probability that the molecules are in the quantum state described by the orbital

where the excitation process is described by generic operator $\hat{\mathbf{A}}$ (we will not specified it for the aim of this section) to the initial state $|i\rangle$ that describes the sample before electron ejection and has a total energy $E(N)$. The final state $|f\rangle$ is composed both by the electron transferred to the vacuum with energy E_{kin} and the sample with total energy $E(N-1)$ after electron ejection. Thus $E_i = E(N)$ and $E_f = E_{kin} + E(N-1)$. The identification of the electron's binding energy E_B in the sample as

$$E_B = E(N-1) - E(N) \tag{2.3}$$

leads to the photoelectrical law which relates the measured kinetic energy E_{kin} to E_B:

$$h\nu = E_{kin} + E_B \tag{2.4}$$

In the case of metals, the binding energy is most conveniently refereed to the Fermi level, which is the same for all parts of the instrument since they share a common ground (fig. 2.3(b)). This leads to a modification of equation 2.4 by the introduction of the work function ϕ, defined as the difference between the vacuum level (E_0) and the Fermi level (E_F):

$$h\nu = E_{kin} + E_B + \phi \tag{2.5}$$

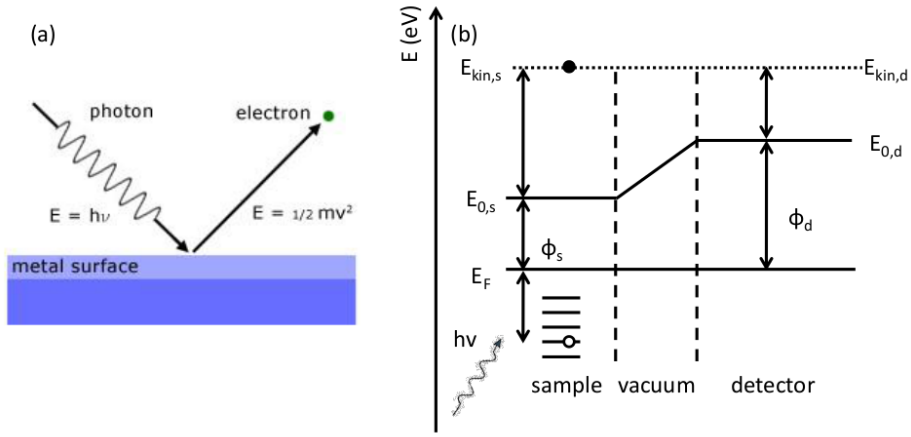

Figure 2.3: *(a)Schematics of the photoemission process; (b)Energy diagram of the detected photoelectrons.*

The emitted photoelectrons are measured with a detector as a function of their kinetic energy. It has to be taken into account that the detection "changes the energy" (fig. 2.3(b)). In fact a photoelectron is emitted with his own kinetic energy ($E_{kin,s}$) that depend of the sample ϕ_s:

$$h\nu = E_B + E_{kin,s} + \phi_s \tag{2.6}$$

On the other hand, energy conservation leads to:

$$E_{kin,s} + \phi_s = E_{kin,d} + \phi_d \tag{2.7}$$

Combining the expressions the measured binding energy of an element is expressed as:

$$E_B = h\nu - E_{kin,d} - \phi_d \tag{2.8}$$

2.2.2 Physics with XPS

X-rays generate photoelectrons from inner core levels with kinetic energy in a range where high surface sensitivity can be obtained. The inelastic mean free path (IMFP) of electrons, inside inorganic as well as organic materials, is typically shorter than several nanometer in a range of (1; 1000) eV [13, 14]. Every element has a characteristic binding energies, in fact the core level binding energies of two neighboring elements in the periodic table vary more than 100 eV (i.e. $E_{BN1s} - E_{BC1s} = 120eV$). With the core levels of the different elements well-separated, XPS spectra give information about the chemical elements present on the surface under investigation. Moreover, the area underlying a XP spectrum gives an idea of the amount of the element present on the surface. This allows XPS also for quantitative analysis. When comparing intensity ratios of peaks originating from different elements, it has to be taken into account the photoionization cross sections. In physics the concept of cross section (σ) is the probability per area unit that an event occurs. In this case the event is the emission of photoelectron upon the absorption of a photon (photoionization process). The photoionization cross section is characteristic for each element and for each level we are considering the photoelectrons are emitted from and depends on wavelength of the incident photons.
Even though the core levels typically do not take part in chemical bonding themselves, their binding energies are strongly affected by the chemical environment, which is the specific combination of all direct bond partners of an atom. For example the binding energy of C 1s level in C-O bond will be different from C-N since the different partners have different electronegativity that will influence

the distribution of the charge. This will provoke the shift of the binding energy peak that can be detected. The direction of the shift towards lower or higher binding energies (with respect to a reference) gives important information not only about the chemical environment but also about other physical process, i.e. charge transfer. In fact an extra presence of electron into an existing bond leads to a decrease of the binding energy of the photoemitted electrons belonging to the elements involved in the bond. This is because, in case of negative ionization, the electrons feel less the presence of the attractive positive nuclei and it is less costly remove them. On the other hand, if an electron is removed from an existing bond, the reduced electron density increases the attractive interaction of the nuclei and, therefore, the binding energy will increase.
Sometimes at the higher binding energy side of a core level, displaced by some eV, there is an additional feature with less intensity. In the description of the photoemission process involving high kinetic energies, we have assumed that the excitation and de-excitation process are instantaneous (Sudden approximation [12]). i.e. the many-particle wavefunction of the ionized sample does not have time to adjust to the new core potential during ionisation so it is non-relaxed. $|N-1\rangle$ is thus not an eigenstate of the system after ionisation, but can be expressed in terms of the (relaxed) eigenstate $|i\rangle$:

$$|N-1\rangle = \sum_i |i\rangle \langle i|N-1\rangle \tag{2.9}$$

This equation shows that the photoemission spectrum is composed of a number of lines that correspond to the eigenstate $|i\rangle$ with an intensity determined by the overlap integrals $\langle i|N-1\rangle$. The highest-kinetic energy line (the main line of XP spectrum) represents the most relaxed final state and has the largest intensity, while the so.called shake-up and satellites at lower kinetic energy (and so to higher binding energy) commonly have very small intensities.
On the other hand, the hole created when the electron is ejected can be filled by different relaxation processes. One of these mechanism is the Auger process: the inner hole is filled by an external electron of the atom, resulting in a release of energy, as shown in figure 2.4. This energy can be released in the form of an emitted photon, but also by another electron ejected outside the sample. This new electron is called the Auger electron, and its energy is given by:

$$E_{kin}(KL_1L_{23})E_K - E_{L1} + E_{L23} \tag{2.10}$$

which depends on the atom type and its chemical environment as well. Thus XP and Auger electron spectroscopy, although they both involve photoemitted

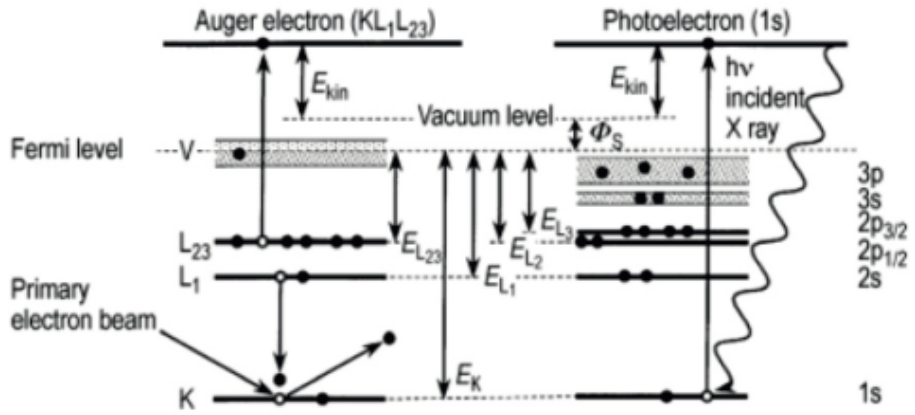

Figure 2.4: *Schematic diagram of the electron emission Auger process (left side) and photoelectron process (right side) in a solid. Electrons involved in the emission process are indicated by open circles. Image taken from the Ref.[15]*

electrons, are based on different physical processes. An important difference is that the kinetic energy of the Auger electron does not depend on the energy of the incident photon.
Finally, high kinetic energy electrons can alter the XPS spectrum. The photoelectrons can transfer part of the kinetic energy through inelastic collisions, to excite resonance structure, i.e. on the surface or adlayer. That is the case of bulk and surface plasmon as we will show in chapter 5.

2.3 TIREMISU UHV System

The presented experimental results have been obtained in the TIREMISU ("TIme REsolved MIcroscopy of SUrfaces") group in the surface science laboratory (LASUAM) of "Universidad Autonoma de Madrid". The setup of the UHV system consists of three Ultra-High Vacuum (UHV) chambers, namely preparation chamber, STM chamber and XPS chamber, as illustrated in figure 2.5.

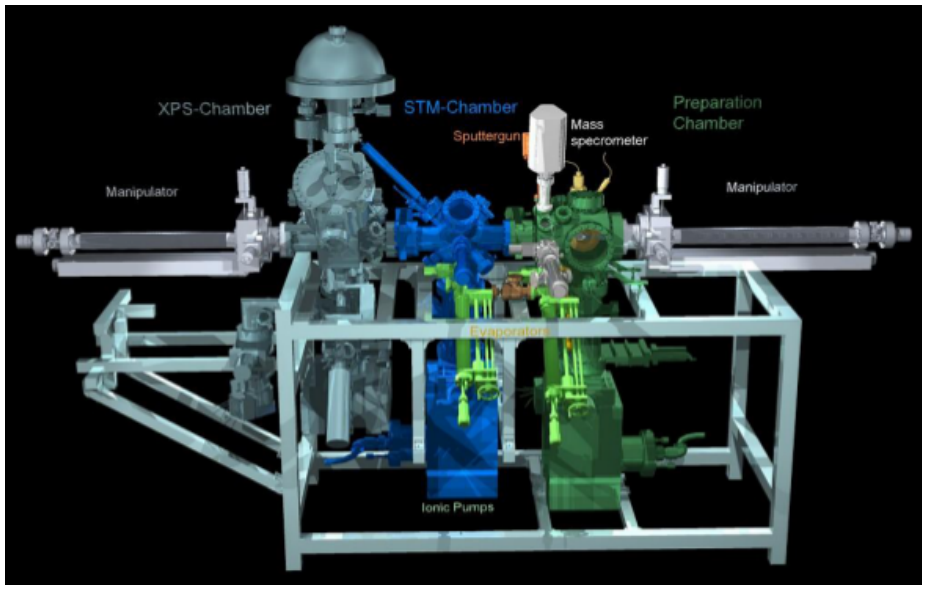

Figure 2.5: *(a)Schematics of TIREMISU system. In green the preparation chamber, in blue the STM chamber, in gray the XPS chamber.*

Preparation chamber

This chamber is schematically coloured in fig. 2.5 in dark green. It is connected to a load lock system for the introduction of external samples in the chamber. The preparation chamber is equipped with the standard UHV preparation tools: mass spectrometer, sputter ion-gun, a Knusden cell evaporator (light green in fig. 2.5), an home made evaporator for metals. In this chamber was also present a LEED system. The manipulator allows to transfer a sample to the neighboring STM chamber. A turbo and a ionic pump enable a base pressure $< 10^{-10}$ mbar.

STM chamber

The STM chamber is indicated in blue in fig. 2.5. The microscope used in this thesis work is the commercial STM Aarhus 150, designed by Professors Flemming Besenbacher, Erik Lægsgaard, and Ivan Stensgaard at the University of Aarhus, Denmark, and purchased from SPECS GmbH. It is a Variable

Temperature VT-STM, in a range of $\sim$ 90 to 400 K. Cooling the sample down is possible by pumping liquid nitrogen through a cooling circuit that sits in a linear motion feedthrough that also clamps the STM while not in operation. Integrated heating Zener diodes allow to keep the piezo scanner always at room temperature. This system permits, on one hand, the possibility to work with only one length scale calibration, but on the other hand it makes the system more sensitive to drift due to the temperature difference between the tip and the sample. The STM Aarhus 150 allows a direct deposition of organic material while scanning thanks to three optical accesses drilled in the aluminum block. This is useful for a cold deposition while the STM block, and thus the sample, are kept at low temperature, avoiding phenomena like diffusion or temperature dependent transition. For this reason there is a Knusden cell evaporator placed in front of the microscope. The chamber is also equipped with a parking to store up to six samples, a leak valve for deposition of liquid phase molecules and a transfer bar. Also in this chamber a base pressure $< 10^{-10}$ mbar is assured by a ionic pump.

XPS chamber

The last XPS chamber is evidenced in gray in fig. 2.5. The XPS system contains:

- X-ray source (SPECS XR 50 M).
  The complete X-ray source package consists of the X-ray source module XR-50 M, the power supplies XRC 1000 M and cooling unit CCX 60. If solid state material (the anode) is bombarded with high energy electrons (13.5 keV in our case) an ionization process of electron core levels occurs. If these vacancies are refilled by electrons from energetically higher levels, characteristic X-ray radiation or Auger electrons will be generated. Besides these two processes, also radiation with a continuous frequency spectrum (Bremsstrahlung) will be produced by retarded electrons. The used source has a twin anode that enables the production of two different photon energies: Al Kα radiation at 1486.74 eV or Ag Lα radiation at 2984.3 eV. For this thesis only Al Kα radiation was used.

- X-ray monochromator (SPECS FOCUS 500).
  This is a commercial ellipsoidal quartz crystal monochromator and is used reduce the line width of the x-ray source. In fact, the X-ray source emits radiations in a broad range of energies in the direction of the crystal. Only

the photons that adjust the Bragg's condition:

$$2d \sin\theta = n\lambda \tag{2.11}$$

with appropriate wavelength λ and incident angle θ are elastically scattered through the crystal and focused on the sample (n is the diffraction order). For Al Kα radiation, this monochromator gives an intrinsic energy resolution of FWHM = 167 meV

- Hemispherical Energy Analyzer (SPECS PHOIBOS 150).
  This is a high resolution spectrometer consisting of an electrical transfer lens system at the entrance, a hemispherical energy analyzer and five exchangeable channeltrons. The work function has been determined to be 4.51 ± 0.03 eV. Several pairs of entrance slits and exit slits can be used to optimize the energy resolution and the angular spread of the photoelectrons.
  In our case, the overall resolution is given by the full width at half maximum intensity (FWHM) of the $3d_{5/2}$ peak of silver reference single crystal that is 0.8 eV at a pass energy of 10 eV (400 W, 15 kV, Aluminum anode). All the data presented in this thesis were obtained resting a Shirley background type and the peaks deconvoluted with Lorentzian distributions.

A motorized manipulator allows the optimization of XPS signal and the transfer to STM chamber. The base pressure $< 10^{-10}$ is provided by turbo and ionic pump.

2.4 The Au(111) reconstructed surface

The surface used throughout this thesis is Au(111). Gold is the only fcc metal where the close-packed (111) surface has been observed to reconstruct. The surface is uniaxially contracted (4.2%) along the $[1\bar{1}0]$ directions where there are 23 atoms for every 22 sites. As a consequence of this inclusion of an "extra" row, the surface layer is stressed and ridges appear. These domain walls (also known as "soliton wave") are dislocation lines that separate fcc bulk-like stacking regions (ABC) from hcp regions (ABA), creating a $(22 \times \sqrt{3})$ unit surface cell. In these dislocation lines the atoms appear 0.15 Å higher (2.6(a)). Such corrugation makes the surface no longer planar. The direction of these lines along the $[11\bar{2}]$ direction rotates periodically by 120°creating the characteristic zig-zag structures[16]. As a consequence, where ridges match the boundaries

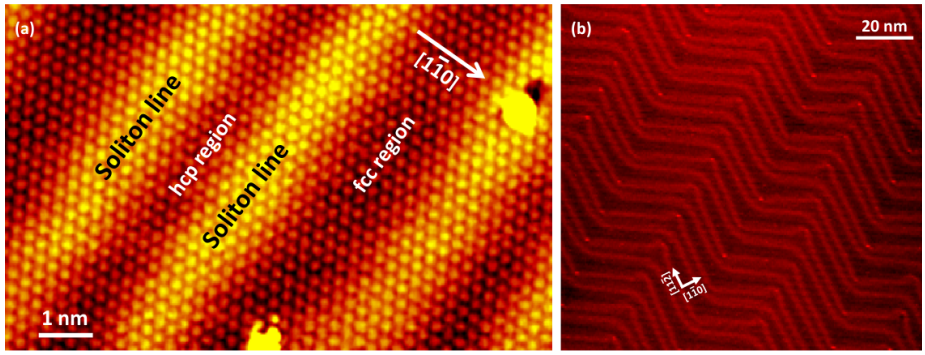

Figure 2.6: *(a) Atomically resolved STM image reveling the atomic arrangement along the* [1$\bar{1}$0] *direction that divides the surface in different regions separated by higher soliton lines (V=-460 mV, I=-12.6 nA). (b) Large STM image showing the Au(111) herringbone reconstruction on the surface (V=-1440 mV, I=-0.430 nA)*

characteristic sites called elbows are formed. The reconstruction of the Au(111) surface is also referred as herringbone reconstruction (2.6(b)).
The average Au-Au bond distances vary depending on the regions: 2.88 Å in the fcc or hcp regions; 2.72-2.75 Å in the ridges and to 2.65-2.68 Å at the elbows[17]. The long periodicity imposed by the herringbone superlattice creates a spatial and energetic rearrangement of the surface states causing a binding energy difference of to -25meV between fcc and hcp regions of the reconstruction[18]. This, together with its inert activity, makes the Au(111) surface an ideal template to investigate the nucleation and growth of adsorbates.

Bibliography

[1] G Binnig, H Rohrer, C Gerber, and E Weibel. Surface studies by scanning tunneling microscopy. *Physical review letters*, 49(1):57–61, 1982.

[2] Nobel Prize for Physics, June 1986.

[3] G. Binnig. Tunneling through a controllable vacuum gap. *Applied Physics Letters*, 40(2):178, 1982.

[4] JI Pascual, C Corriol, G Ceballos, and I Aldazabal. Role of the electric field in surface electron dynamics above the vacuum level. *Physical Review B*, pages 1–7, 2007.

[5] G Binnig and H Rohrer. Scanning tunneling microscopy. *Surface Science*, 126:236–244, 1983.

[6] J Tersoff and DR Hamann. Theory and application for the scanning tunneling microscope. *Physical review letters*, 50(25):1998–2001, 1983.

[7] J. Bardeen. Tunneling from a many-particle point of view. *Physical Review*, 6(2):57 – 59, 1961.

[8] ND Lang. Spectroscopy of single atoms in the scanning tunneling microscope. *Physical Review B*, 34(8):2–5, 1986.

[9] G Binnig and H Rohrer. Surface imaging by scanning tunneling microscopy. *Ultramicroscopy*, 11(2):157–160, 1983.

[10] Brian Harold Bransden and Charles Jean Joachain. *Physics of atoms and molecules*. Pearson Education India, 2003.

[11] Nobel Prize for Physics, June 1981.

[12] Stefan Hüfner. Photoelectron spectroscopy-principles and applications, vol. 82 of springer series in solid-state sciences, 1995.

[13] Shigeo Tanuma, Cedric J Powell, and David R Penn. Calculations of electron inelastic mean free paths for 31 materials. *Surface and Interface Analysis*, 11(11):577–589, 1988.

[14] Shigeo Tanuma, Cedric J Powell, and David R Penn. Calculations of electron inelastic mean free paths. v. data for 14 organic compounds over the 50–2000 ev range. *Surface and Interface Analysis*, 21(3):165–176, 1994.

[15] Henning Bubert, John C Rivière, Heinrich F Arlinghaus, Herbert Hutter, Holger Jenett, Peter Bauer, Leopold Palmetshofer, Laszlo Fabry, Siegfried Pahlke, Alfred Quentmeier, et al. *Surface and Thin-Film Analysis*. Wiley Online Library, 2002.

[16] R.J. Behm J.V. Barth, H. Brune, G. Ertl. Scanning tunneling microscopy observations on the reconstructed Au(111) surface: Atomic structure, long-range superstructure, rotational domains and surface defects. *Physical Review B*, 42(15):9307–9318, 1990.

[17] Xiao-Gang Wen. Quantum orders and symmetric spin liquids. *Phys. Rev. B*, 65:165113, Apr 2002.

[18] W. Chen, V. Madhavan, T. Jamneala, and M. F. Crommie. Scanning tunneling microscopy observation of an electronic superlattice at the surface of clean gold. *Phys. Rev. Lett.*, 80:1469–1472, Feb 1998.

Chapter 3

Charge transfer through organic and hybrid structures on Au(111)

This chapter is focused on the study of different supramolecular structures obtained by intermixing of organic acceptor molecule, tetracyanoquinodimethane (TCNQ), with two different donor species. One is represented by metallic iron atoms, which leads to the self-organization of extended Metal-Organic Coordination Network (MOCN). The other specie is another organic molecule, tetrathiafulvalene (TTF), which exhibits a strong donor character.
It will be studied firstly the structural and electronic properties of individual organic elements adsorbed on Au(111) reconstructed surface, then the intermixed supramolecular structures. The growth of the iron will be studied in the next chapter.

3.1 Introduction

In the past years, a novel route for the cheap production of compounds with atomic precision is the autonomous ordering and assembly of atoms and molecules on atomically well-defined surfaces[1]. After the first reports of 2D supramolecular nano-structures, the idea of using molecules for bottom-up assembly became an established route for the cheap production of functional

nanoarchitectures in the size range of about 1-100 nm, covering the atomic, molecular and macromolecular length scales[2]. In general, the 2D molecular self-assembly on solid surfaces is the result of a combination of intermolecular non-covalent forces, namely hydrogen bonding[3], Van der Waals forces[4] and metal-ligand coordination[5, 6], with molecule-substrate interactions. These interactions govern also the molecular recognition developed either between adsorbed molecules, via functional groups providing geometrical or electronic complementarity[7], and between molecules and substrate[8]. Only when lateral and surface interactions are well balanced, a stable supramolecular structure is sustained on the surface. Thus the controlled adsorption and formation of non-covalent bonds is the key ingredient for fabrication of supramolecular architectures and nanostructures.

3.2 Organic acceptor molecule: TCNQ on Au(111)

The organic molecule 7,7,8,8-tetracyanoquinodimethane (TCNQ, $C_{12}H_4N_4$) was discovered in the 60's by L. M. Melby and coworkers[10] and is considered one of the strongest organic electron acceptors. Figure 3.1 shows the chemical structure of TCNQ. In its neutral state, TCNQ has a central quinoid carbon ring which is connected to four hydrogen atoms and two dicyanomethylene groups

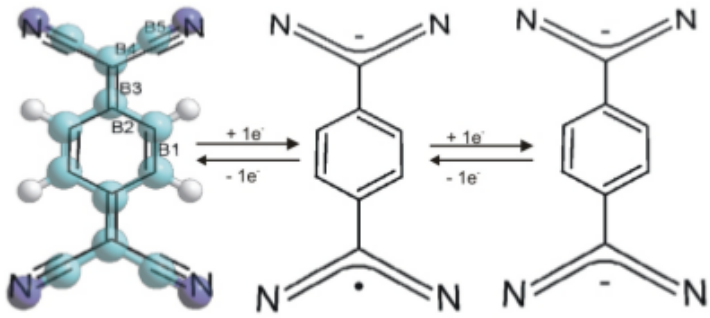

Figure 3.1: *Scheme of the chemical structure of $TCNQ^0$, $TCNQ^{-1}$ and $TCNQ^{-2}$ (dark blue spheres are nitrogen atoms, light blue spheres are carbon atoms and white spheres are hydrogen atoms). When the neutral TCNQ accepts one electron, the extra negative charge is delocalized in one of the two dicyanomethylene groups and causes bond changes, where (B3) goes from double bond to single bond, and a partial aromatization of the central quinoid ring. A second electron is hosted in the other dicyanomethylene group and completes the aromatization process. Image from [9]*

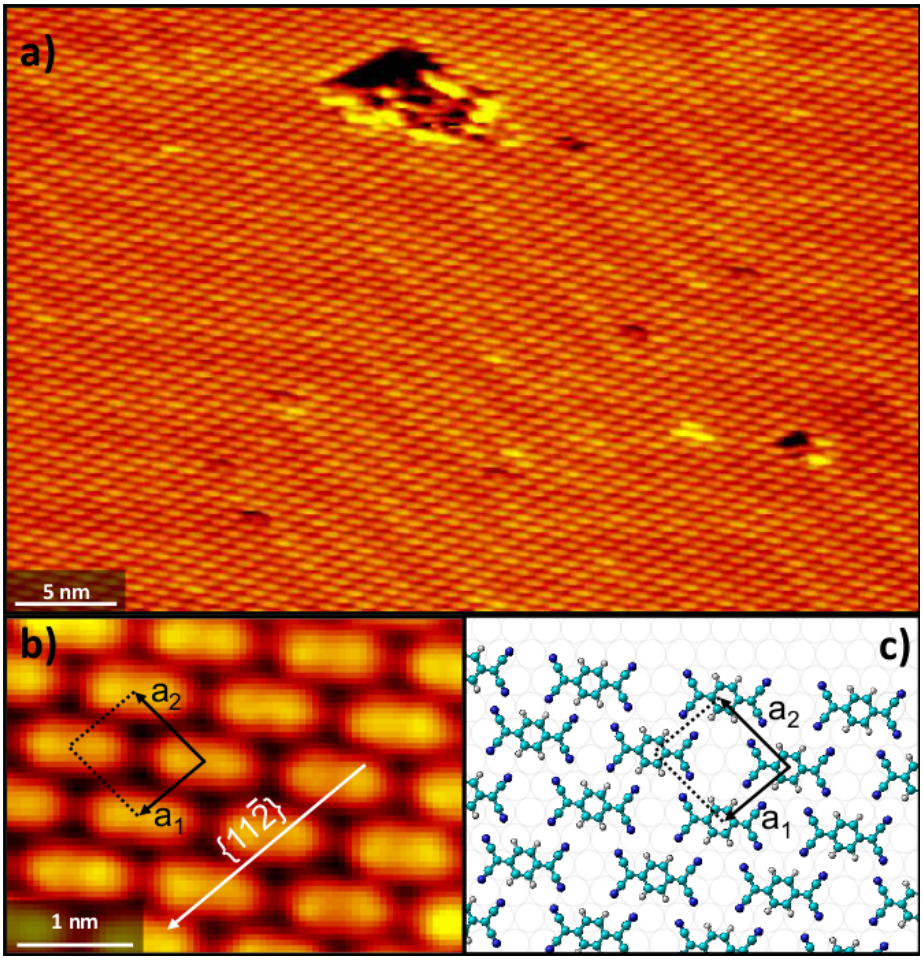

Figure 3.2: *a) Large STM area of a self-assembled domain of TCNQ. The herringbone reconstruction of Au(111) surface is visible through the molecular island (I_t=0.110nA; V_t=450mV). (b) Zoom with intermolecular resolution in a TCNQ islands. The supramolecular structure has a rhombic unit cell with vectors $a_1 \sim a_2 \sim$1nm. The vector a_1 runs along the $[11\bar{2}]$ surface direction and a_2 presents a slight deviation of 5 ° with respect to the perpendicular direction (I_t=0.110nA; V_t=350mV). c) Adsorption model of TCNQ on Au(111) surface.*

(R-C-(C≡N)$_2$). The acceptor properties of TCNQ arise from the strong electrophilic (literally from greek *electron-friend*) behaviour of these terminations. Therefore each TCNQ molecule can accommodate up to two extra electrons. One extra negative charge is delocalized in one of the two dicyanomethylene groups and causes structural and electronic rearrangement. In fact, bond B3 goes from double bond to single bond character (fig.3.1), that leads to a partial aromatization of the central quinoid ring. A second electron is hosted in the other dicyanomethylene group and completes the aromatization process.

Room temperature deposition of TCNQ (crucible held at 75 °C, which leads to a deposition rate of 0.25±0.05 ML/min) onto a Au(111) surface results in the formation of highly ordered TCNQ self-assembled domains that extend over hundreds of $\mathring{A}$ (fig.3.2a). The STM images show, superimposed to the molecular corrugation, the unperturbed pattern of the herringbone reconstructed surface. This is a characteristic fingerprint of a weak form of adsorption to a solid surface, physisorption, characterized by the lack of a true chemical bond between adsorbate and substrate[11]. This weak molecules-substrate interaction is balanced by hydrogen bonds between cyano groups and benzene rings (C≡N$\cdots$H-C), that stabilize the self-assembled structure. Despite this physisorbed state, TCNQ exhibits a certain degree of commensuration with the Au(111) lattice. The TCNQ supramolecular structure has a rhombic unit cell with vectors $a_1 \sim a_2 \sim$1nm (fig.3.2b). The vector a$_1$ runs along the $[11\overline{2}]$ surface direction and a$_2$ presents a slight deviation of 5°with respect to the perpendicular direction. Figure 3.2c shows a simple model that accounts for both this lattice parameters and a commensuration with the underlying gold lattice. As a result, TCNQ molecules alternate two adsorption sites, one with the C atoms of the central ring on Au(111) hollow sites and other where C atoms are distributed on bridge and top sites[12]. In general, the physisorbed state does not favour the natural tendency of TCNQ to accept charge, i.e. from the substrate in this case, as also confirmed in high detailed STM images at very low temperature (around few Kelvin) of similar works, showing that the shape of orbital, at positive voltages, resembles the shape of the LUMO in gas phase[12].
The XPS spectra of nitrogen 1s and carbon 1s core levels are shown in fig.3.3. The spectrum of N_{1s} can be deconvoluted into two peaks: the most intense peak is located at binding energy of 398.9 eV while a second peak is at 2.6 eV towards higher binding energy. This relatively small peak is attributed to an intramolecular electronic excitation process (shake-up satellite, see chapter 2). The most intense peak at 398.9 eV has a FWHM=0.9 eV that indicates an unique chemical environment for nitrogen atoms in TCNQ on Au(111) due to their equivalency in the two dicyanomethylene groups. The XPS spectrum for

C_{1s} shows a broad peak together with a shake-up satellite located once again at 2.6 eV above the main peak. The structure of the main peak reveals that carbon atoms are present in more than one type of chemical environment. Although the resolution does not permits to identify each distinct carbon components at the binding energies of peaks associated with them, a possible deconvolution of the main peak of C_{1s} leads to the identifying of two components that well fit the experimental spectrum: one at 285.9 eV and another at 284.5 eV reflecting, both with FWHM=1.5 eV, with the ratio between the area of these two peaks of $\sim$ 1:1. This suggest two main environment groups for carbon atoms with approximately equal population. Accordingly to similar work[13, 14, 15], we assign the peak at 285.9 eV to the more positive carbons of dicyanomethylene groups (six carbon atoms) and the peak at 284.5 eV to carbons belonging to the benzene ring(six carbon atoms too).
In first approximation and accordingly to the experimental observations and literature works, therefore, we can assume the physisorbed TCNQ molecules almost neutral on Au(111) surface and we can take the values in binding energy as references for the systems in which TCNQ is co-adsorbed with electron donors.

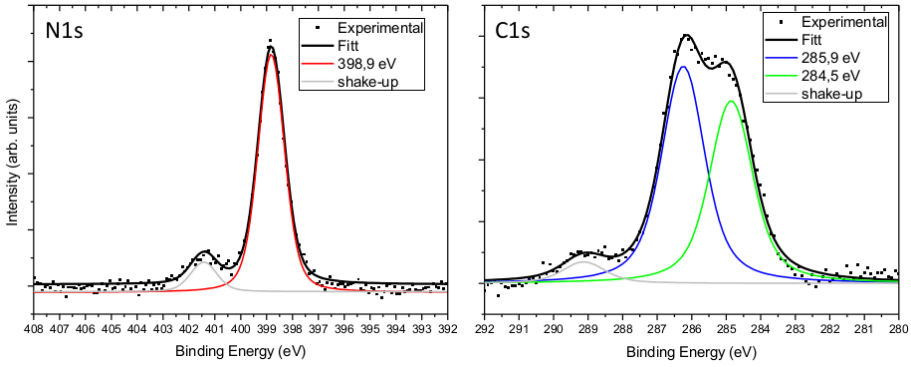

Figure 3.3: *The N1s spectrum is represented by a single peak at 398.9 eV with relative shake-up satellite separated by 2.6eV towards higher binding energy. The C1s spectrum is deconvoluted into two peaks at 285.9 eV and 284.5 eV. Also in C1s region is well visible a shake-up satellite at 288.5eV. According to similar works and to STM observation, these value represent neutral TCNQ on Au(111)*

3.3 2D-Metal Organic Coordination Network

Metal-Organic Frameworks (MOFs) are compounds consisting of a coordinating metal atom (referred as coordination center) ligated to organic molecules (ligands) by coordination bonds. The orbitals overlapping between the central atom and the ligands allows the delocalization of electrons and forms the coordination bond that is rather weak compared to covalent bonds. The delocalization of the electrons involves a synergic process between the donation of electrons from the filled p-orbital or lone electron pair orbital of the ligand into an empty orbital of the metal, and the release, or back-donation, of electrons from d-orbital of the metal in π-symmetry with respect to the metal-ligand axis into the empty π^*-antibonding orbital of the ligand[16]. Given such a coordination environment around the metal centers, the symmetric and rigid extension of the ligand can lead to 1D, 2D, or 3D coordination network with regularly arrayed metal ions [17]. Therefore the latter plays an active role by favoring particular coordination numbers and modes that result in a given stoichiometry, determining the charge and magnetic moment of both the metal center (which depends on the d-orbital occupation for transition metal, f-orbital for lanthanides) and organic ligand. This allows us to control the electronic and magnetic properties of the interface[18].
On surfaces these compounds can differ from their bulk counterparts since molecule-substrate interactions can compete. In the last years, surface assisted metal-coordination bonding was used for the fabrication of molecular architectures of well defined geometry with specific functional properties. Many examples of diverse 2D metal-organic coordination networks (MOCNs) with tunable sizes and topologies[19], suitable for host-guest chemistry[20] and regular arrays of spin centers[21]were demonstrated.

3.3.1 MOCN: TCNQ+Fe on Au(111)

In this section we will discuss a network obtained by evaporation of the strong electron acceptor TCNQ molecules and subsequently deposition of Fe atoms onto the Au(111) surface kept at room temperature. The resulting structure is shown in figure 3.4(a), upon the deposition of $\sim$ 0.15 ML of iron onto precovered TCNQ submonolayer ($\sim$0.90 ML) on Au(111) surface. The cyano groups (C$\equiv$N) of the TCNQ molecules react readily with the metal atoms at room temperature leading to the formation of rectangular superstructure. The statistical analysis of the STM images reveals that the well ordered islands have at least six directions of symmetry with respect to the surface, which indicates

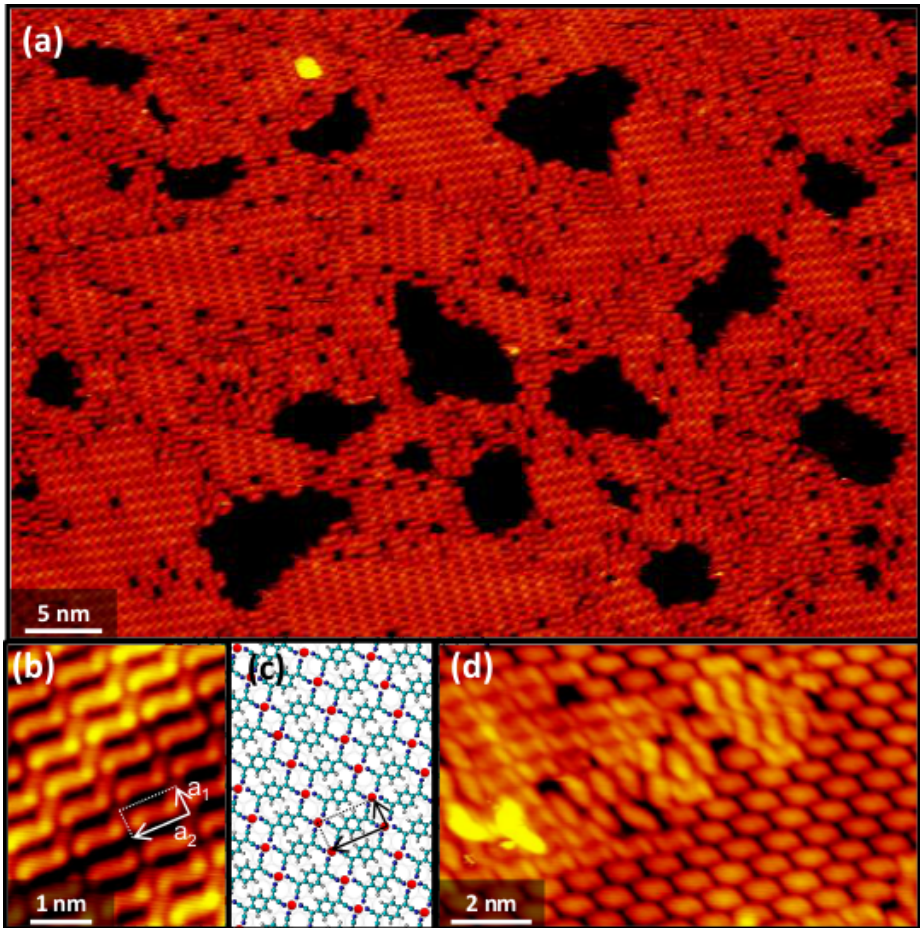

Figure 3.4: *(a) STM image of large area (50x35nm^2) of TCNQ after the deposition of iron leading to the formation of MOCN Fe-TCNQ islands on Au(111) surface (I_t=-0.35nA $V_t = -1440mV$); (b) Detail of MOCN: the supramolecular structure has a rectangular unit cell with vector represented by a_1 ∼0.5 nm and a_2 ∼1 nm superimposed to STM image (I_t=-0.11nA $V_t = -1650mV$); (c) adsorption model of MOCN:Fe-TCNQ on Au(111) surface; (d) detail of area with both un-coordinated and coordinated TCNQ molecules. The difference is of orbital shape reflect different electronic and chemical environment (I_t=-0.27nA $V_t = -1320mV$).*

a certain degree of commensuration with the fcc(111) surface lattice[1]. On the other hand, the islands of the superstructure have a relatively small average area ($\sim$150nm^2). The simultaneous presence of islands with small domain size and an integer multiple of three of orientations with respect to fcc(111) surface suggests that the commensurability of the superstructure, with respect to Au(111) underlying surface, is only locally sustained, in accord with similar work[22, 23]. The 2D-MOCN, in fact, has a rectangular unit cell with vectors $a_1 \approx 5.0 \pm 1.0\mathring{A}$ and $a_2 \approx 10.0 \pm 1.0\mathring{A}$ (fig.3.4(b)). The unit cell contains one TCNQ molecule and one atom iron (fig.3.4(c)), leading to 1:1 stoichiometry. No other structures were observed depositing different stoichiometric ratio between TCNQ and Fe atoms in the formation of the overlayer structure. Therefore within this structure, each Fe center coordinates four TCNQ ligands via the cyano groups. The complete coordination of one monolayer of TCNQ is experimentally observed at a coverage of θ_{Fe}=0.18$\pm$0.05ML, that represents the stoichiometric amount needed to coordinate a complete monolayer of TCNQ on Au(111). The presence of Fe alters significantly the chemical environment of the TCNQ molecules as shown in fig.3.4(d), where it is possible to note a surface area with both un-coordinated and coordinated TCNQ molecules and consequently the clear difference of orbital shape between their orbital shapes.

The XPS spectra of N_{1s} and C_{1s} regions of the MOCN in fig.3.4 are shown in fig.3.5, together with the spectra of TCNQ/Au(111) in order to underline the differences. The addition of Fe atoms significantly lowers the binding energies of N_{1s} and C_{1s} and considerably changes the C_{1s} peak shape. The N_{1s} spectrum can be deconvoluted in the contribution of a main peak centered at 398.4 eV plus a shake-up satellite at higher binding energy. The main peak of N_{1s} in MOCN results shifted 0.5 eV to lower binding energy with respect to N_{1s} of neutral TCNQ/Au(111). It is worth noting that the coordinated nitrogen atoms are all equivalent since the FWHM of this peak is once again $\sim$0.9 eV, as in the case of TCNQ/Au(111), reflecting one and only new chemical environment. The carbon environment also results affected by the coordination bond. In fact the C_{1s} XP spectrum results shifted towards lower binding energy and with different shape with respect to C_{1s} of TCNQ/Au(111). A possible decovolution identifies two main peaks located at 284.1 and 285.6 eV, both with FWHM=1.5 eV, and with the ratio between the area of $\sim$ 2:1. The simultaneous shift towards lower binding energies (see chapter 2) of both N_{1s} and C_{1s} reflects an accumulation of extra negative charge with respect to TCNQ/Au(111). Accordingly to the structural model of fig.3.4(c), the delocalization of an extra

[1] A fcc(111) surface has three high symmetry directions

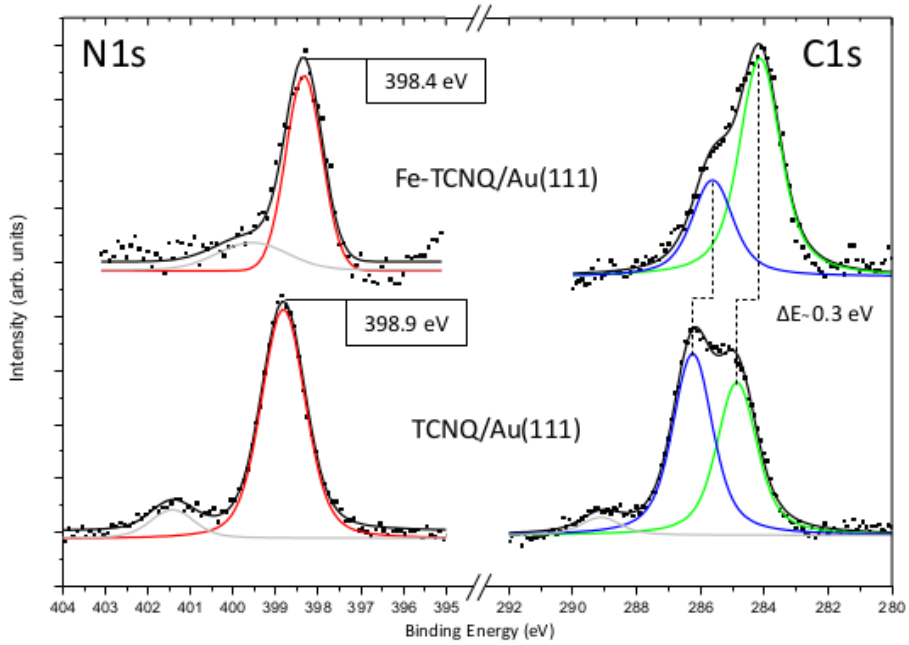

Figure 3.5: *N1s and C1s XP spectra of neutral TCNQ (TCNQ/Au(111) in bottom) and negatively charged TCNQ (Fe-TCNQ/Au(111) upper panel). The shift in binding energy position of N1s in MOCN structure is estimated to be 0.5eV with respect to neutral TCNQ, fingerprint of an extra amount of negative charge throughout the cyano groups. The process of a charge transfer is accompanied by the aromatization of benzene ring of TCNQ molecule and, consequently, by the shift and change of C1s spectrum of MOCN with respect to TCNQ on Au(111) surface.*

amount of negative charge is equal throughout the cyano groups involved in the coordination environment, as also confirmed by the unique chemical environment found for N_{1s} region. As previously discussed, the accommodation of extra negative charge in dicyanomethylene groups is accompanied by partial aromatization of the central quinoid ring, due to the change from double bond to single bond character of the bond B3 positions in fig.3.1. Within this picture, the two symmetric carbon atoms in B3 bond positions feel the same electronic environment of the six atoms of the benzene group, in contrast with the four carbon atoms in the cuano groups. This would create two groups of carbon atoms, one composed by eight atoms (six of ring plus two in B3 position), and

another composed by four atoms (one for each cyano group), that will explain the ratio $\sim$ 2:1 between the two components of the C_{1s} spectrum. Following the same approach of previous case study, we assign the the peak at 285.6 eV to the more positive carbons of cyano groups and the peak at 284.5 eV to carbons belonging to the ring plus the B3 carbon atoms. It is worth noting that the two components of C_{1s} result rigidly shifted towards lower binding energy of $\sim$0.3 eV with the respect to the components in TCNQ/Au(111). Therefore the system the 2D-MOCN Fe-TCNQ/Au(111) shows, from the relative position of both N_{1s} and C_{1s}, an accommodation of extra negative charge with respect to TCNQ/Au(111). Since TCNQ does not accept electrons from gold substrate, the charge transfer is unequivocally due to the formation of of 2D-MOCN and, in particular, to the coordination process of cyano groups with Fe centers.
Figure 3.6, in fact, shows the XPS spectra of pure Fe/Au(111)(bottom) and MOCN Fe-TCNQ/Au(111)(up). For Fe/Au(111) system, the Fe_{2p} XPS signal shows a metallic behaviour with the $Fe_{2p_{3/2}}$ photoemitted line at $\sim$707.0eV and doublet separation of 13.1eV. The MOCN shows a different feature for Fe_{2p}: the shape of spectrum appears like oxidized iron[24], with a shift towards higher

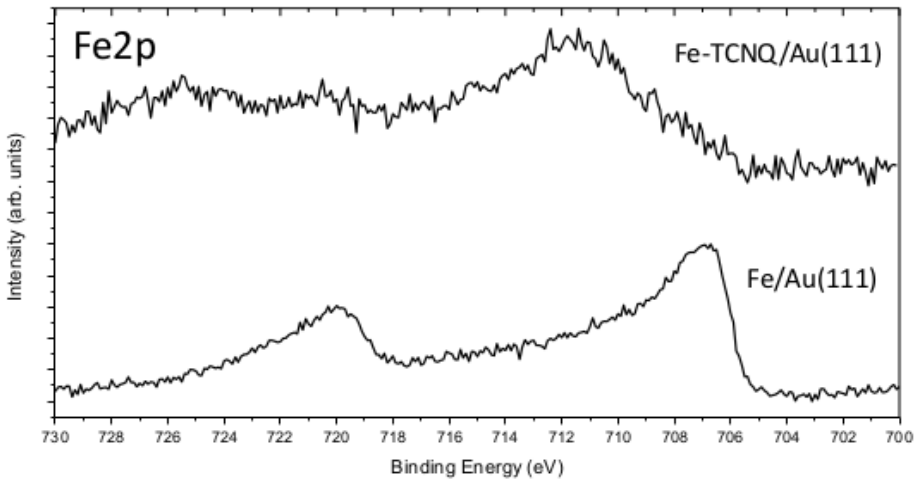

Figure 3.6: *(Fe2p XP spectrum of bare iron (Fe/Au(111) in bottom) and positively charged iron (Fe-TCNQ/Au(111) upper panel. The first has the characteristic metallic shape with shape with $Fe_{2p_{3/2}}$=707.0eV and doublet separation of 13.10 eV. Fe atoms in MOCN appear with characteristic oxidized shape with the peak of $Fe_{2p_{3/2}}$ shifted of 4.4eV towards higher binding energy and doublet separation of 13.6eV)*

binding energy of about 4 eV ($Fe_{2p_{3/2}}$ at 711.4 eV) and doublet separation of 13.6eV. This shift is commonly assigned in literature to +2 or +3 oxidation state of iron[25, 26]. The oxidation process involves the loss of electrons and no presence of oxygen, or any other contaminations, was detected by the XPS survey. Since iron does not result oxidized when deposited on Au(111) surface, we conclude that the interaction with TCNQ molecules provokes the loss of electrons and the increase in oxidation state in Fe atoms through the σ-donation π-backdonation mechanism as discussed above. We are not able to experimentally determine the net amount of negative charge transferred: screening effects or charge dispersion into substrate may alter the XPS spectra. However, the quantity of negative charge experienced by nitrogen in TCNQ molecules in 2D-MOCN with Fe centers results increased with respect to almost neutral TCNQ on Au(111) surface.

3.4 2D-Charge Transfer complexes

Molecular Charge-Transfer (CT) complexes are based on the interaction between two molecular species, namely donor (D, small ionization potential) and acceptor (A, large electron affinity). When both species interact, the charge is redistributed among the compound: the donor molecule oxidizes by the loss of charge and the acceptor is reduced. The generic charge transfer reaction can be written as:

$$mD + nA \rightarrow D_m^{+\delta} + A_n^{-\delta}$$

where m and n are integer numbers and δ is the charge transfer ratio[27]. The process of the charge transfer is schematically shown in fig.3.7(a). I_D is the ionization energy gained by the originally neutral donor molecule after ejecting an electron from HOMO of this molecule. The affinity energy E_A characterizes the energy gained by the originally neutral acceptor molecule when an electron is added to its LUMO.
In some cases, these donor-acceptor interactions mediate the formation of charge-transfer crystalline solids in which organic molecules are stacked in homomolecular rows and stabilized by $\pi-$stacking interactions. In fact the molecules pack rather densely in order to maximize the orbital overlapping between neighboring molecules in which the charge transfer between the donor and the acceptor counterparts occurs[29]. The electronic transport properties of organic charge transfer complexes are strongly connected with the crystal structure of these materials, i.e. with the stacking arrangement of the donor and acceptor molecules in the CT complex. Qualitatively different stacking geometries of the molecules

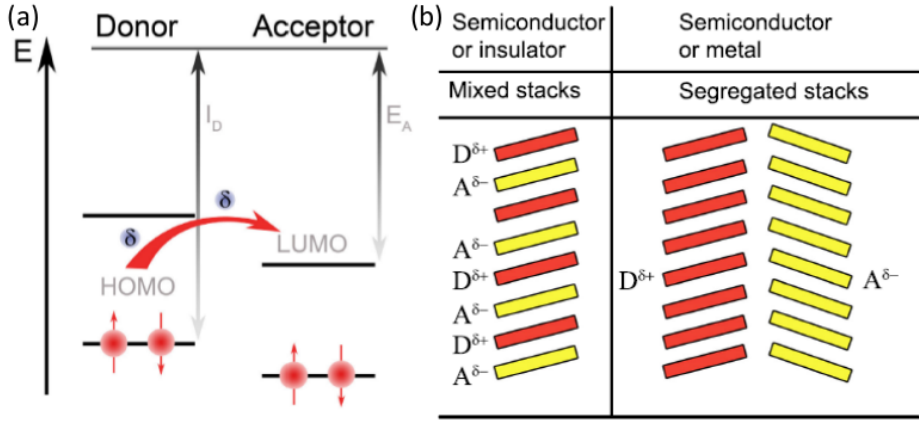

Figure 3.7: *(a)Energy diagram for the donor and the acceptor energy levels. The process of charge transfer is schematically illustrated with the curved arrow; (b)Possible stack structures of donor and acceptor molecules in the organic CT compounds. On the left side: the mixed stack structure; On the right: segregated stacking arrangement variant is presented. Images taken from ref.[28]*

in organic CT complexes are shown in fig.3.7(b). The segregated stack structure of donor and acceptor molecules, with two types of separate stacks, leads to either semiconductor or metallic behavior of the electrical conductivity. Segregated stacks result in partially-filled bands of the overlapping $\pi-$orbitals, as the donors transfer a partial charge to the acceptor stacks. In the case of mixed stacks of donor and acceptor molecules organic CT complexes are insulators.

3.4.1 Organic donor molecule: TTF on Au(111)

The organic molecule tetrathiafulvalene (TTF, $C_6H_4S_4$) was firstly reported by Wudl in 1970[30] and, simultaneously and independently, by Hünig *et al.*[31] and Coffen *et al.*[32] and is a well known donor molecule together with its derivatives[33]. Figure 3.8 shown the chemical structure of TTF which, in its neutral state, is formed by two dithiol-ylidene rings connected by carbon atoms. TTF is a non-aromatic 14π electron system in which oxidation to the radical cation and dication states occurs sequentially and reversibly (fig.3.8)[34].

Deposition at room temperature of TTF (crucible held at room temperature too) onto Au(111) surface leads to a situation different from previous case. From our measurements, we found that TTF molecules diffuse too rapidly onto gold

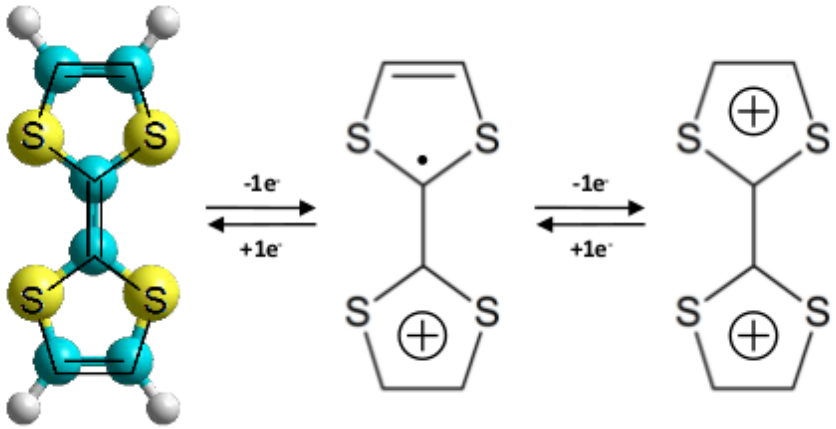

Figure 3.8: *Chemical structures of TTF^0, TTF^{+1} and TTF^{+2} (sulfur atoms in yellow, carbn in light blue and hydrogen atoms in white spheres). The neutral TTF can donate up to two electrons, each from dithiol-ylidene rings, as shown in the oxidation transformations.*

surface even cooling down the sample at ∼90K, leading to low detailed STM images (figure3.9a). From previous works about TTF on Au(111) surface[35, 36], we know that below 0.2 ML TTF does not form supramolecular islands. In other words TTF does not respond to attractive forces, i.e. hydrogen bonding to sulfur atoms[37]. The tendency to avoid nucleation through the formation of nearly periodic molecular array is indicative of a long-range interaction mechanism, different from short-range noncovalent dispersion forces between molecules. At higher coverages, TTF forms zigzag chainlike structures uniformly distributed over the surface. These chains exhibit a labyrinthine pattern as it is rather distinguishable in our STM images. This difference between low and high coverage is characteristic of a 2D system in which there is a competition between long-range repulsion and short-range attraction[38, 39].

Figure 3.10 shows the photoemission spectra of S_{2p} and C_{1s} regions respectively. The spectrum of S_{2p} can be decomposed into two components consisting of a spin-orbit doublet. The $S_{2p_{3/2}}$ is centered at 164.2 eV, with the typical doublet separation for 2p level of sulfur of 1.18 eV[24]. From previous works[35, 36, 40], we know that TTF molecules donate electrons to Au(111) surface. Extrapolated from the limit of a single molecule on the surface, at low

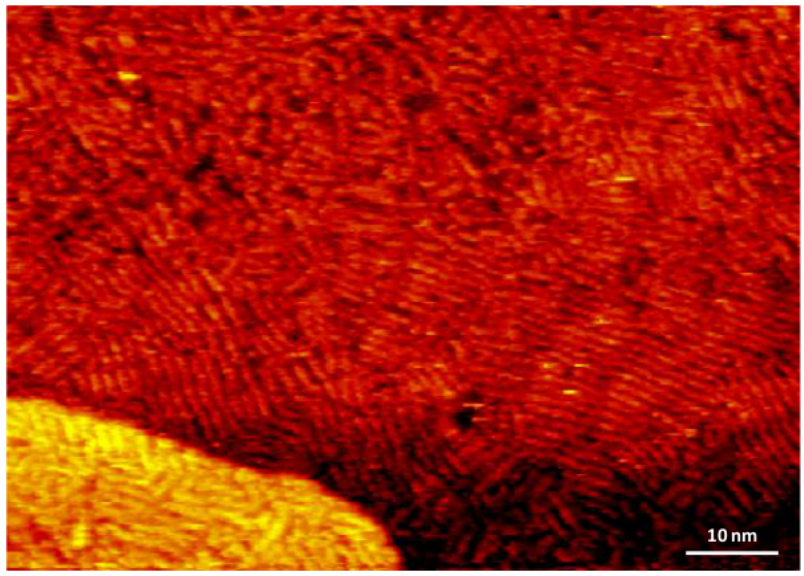

Figure 3.9: *STM images taken at 90 K of TTF/Au(111) (I_t=-0.07nA $V_t = -1375mV$).*

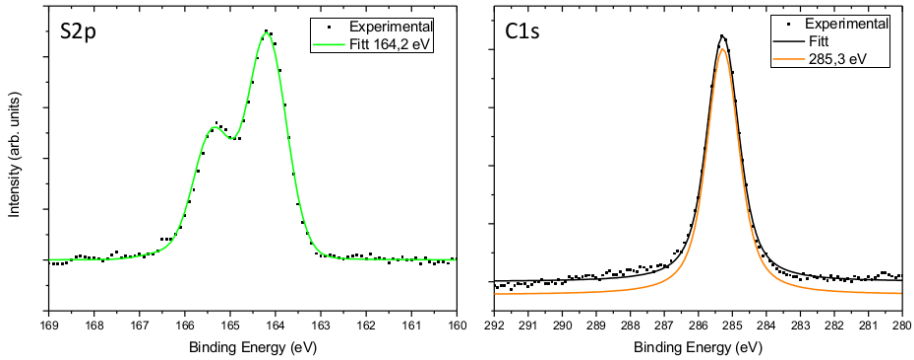

Figure 3.10: *The S2p spectrum is represented by a single peak at 164.2 eV with doublet separation of 1.18eV. The C1s spectrum is deconvoluted into a single peak centered at 285.3 eV reflecting the partial cationic environment of carbon atoms that are singly bound to each other and to sulfur atoms. A little shake-up satellite is located at 287.9 eV*

coverage the charge transfer is of 0.27 electrons from the molecules to the surface, which explains the electrostatic repulsion between molecules once deposited on Au(111) surface at low coverage. Strong chemisorptive sulfur-gold interactions, as found for thiol-based[41] and thiophene[42] molecules self-assembled on Au(111) surface, shows values of binding energy S_{2p} around 162.5 eV. Thus, for TTF/Au(111), TTF exhibits a less strong bonding character. Also C_{1s} XP spectrum seems to corroborate this assumption because the spectrum can be deconvoluted with a single peak centered at 285.3 eV with a FWHM of 0.9 eV reflecting the partial cationic environment of carbon atoms that are all singly bound to each other and to sulfur atoms as shown in fig.3.8. Also a little shake-up satellite for C_{1s} is located at 287.9 eV

3.4.2 Charge transfer complex TTF-TCNQ on Au(111)

The first metallic charge-transfer compound was the TTF-TCNQ salt discovered in 1973[43], which has been considered a prototype of low-dimensional organic metal, exhibiting a room temperature conductivity of $400\pm100\Omega cm^{-1}$[44]. The formation of the organic crystal results from anisotropic non-covalent interactions between TTF and TCNQ molecules. It crystallizes in a monoclinic structure with lattice constants: a=1.23 nm, b=0.38 nm, c=1.85 nm and build-up from similar stacks of the donor and acceptor molecule parallel to the short *b* axis, as shown in fig.3.11(a-b). In *b* direction the "ring double bond" overlap of molecular planes is characteristic of both molecule stacking, built up from homologous stacks of TTF and TCNQ[47]. The *a* direction of the crystal corresponds to alternate rows of TTF cations and TCNQ anions, stabilized by H-bonds[48]. The molecular packing maximized the overlapping integral and, consequently, the amount of the charge that can be delocalized along the stacks. The free carriers are generated in both π-stacked rows due to charge transfer between TTF and TCNQ that amounts to 0.59 e^-[49]. This transferred charge is delocalised along the *b* direction of the crystal resulting in a quasi-one-dimensional organic conductor, as it has been both described by theoretical calculations[50] and experimental work[51].
In a monolayer, the conditions for charge transfer can be significantly altered by competing processes, such as the interaction between molecular π and substrate orbitals can give rise to distinct and new adsorption unit cell geometry[52], inhibition or formation of new electronics bands[53], and so on. Hence, a comparison of the amount of charge transfer on the surface with the respective bulk material is *a priori* difficult. This difference may cause intriguing new physical processes and properties, such as magnetism and superconductivity[54, 55].

Deposition of both molecular species on clean Au(111) surface, held at room temperature, leads to a mixed phase structure characterized by the alternation of one-dimensional homomolecular chains as shown in STM image of large area in fig.3.12a. It is worth noticing that the formation of this structure is independent of the order of deposition of the building blocks. Such structure has a rhombic unit cell with vectors $a_1 \approx 8.0 \pm 1.0\mathring{A}$ and $a_2 \approx 20.0 \pm 1.0\mathring{A}$ (fig.3.12b). The unit cell contains one TTF and one TCNQ molecule (fig.3.12c). Therefore, the surface mixed phase is characterized by TTF 1:1 TCNQ stoichiometry, as in case of bulk. However, TTF and TCNQ molecules are found to adsorb almost planar on Au(111) surface[56] in contrast with bulk counterpart. As a consequence, the unit cell of surface structure results slightly larger than in the bulk case. Statistical anaysis of the STM images reveals that TTF and TCNQ molecules do not aggregate on surface in the bulk-like stacking. Therefore, the interaction of π electrons with the metal surface appears stronger than intermolecular π-stacking. The formation of the surface mixed phase is observed to occur with a yield of $\sim$100%, in fact all the TTF available assembles with the

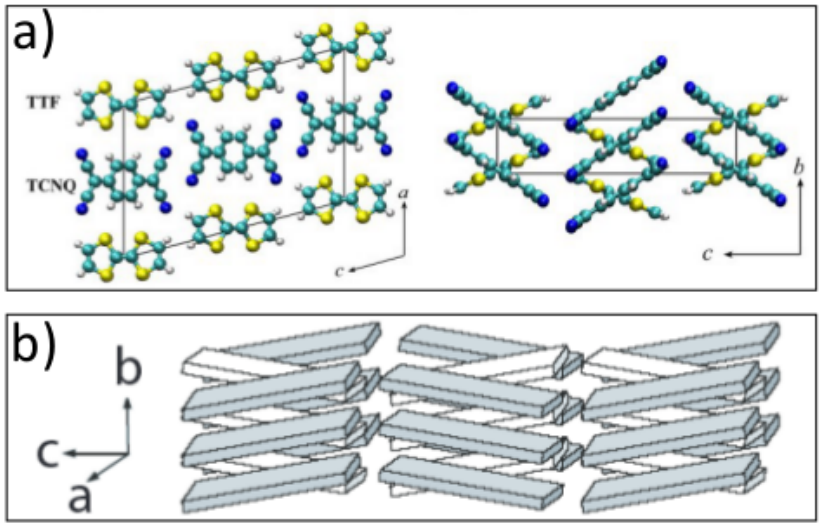

Figure 3.11: *(a)Crystal structure of the TTF-TCNQ complex showing the a,b,c directions. (left side) view along onto the ac directions, (right side) view along the bc directions[45]; (b) three-dimensional schematic view of crystal structure of TTF-TCNQ where gray building blocks represent the TTF, withe ones are TCNQ molecules[46].*

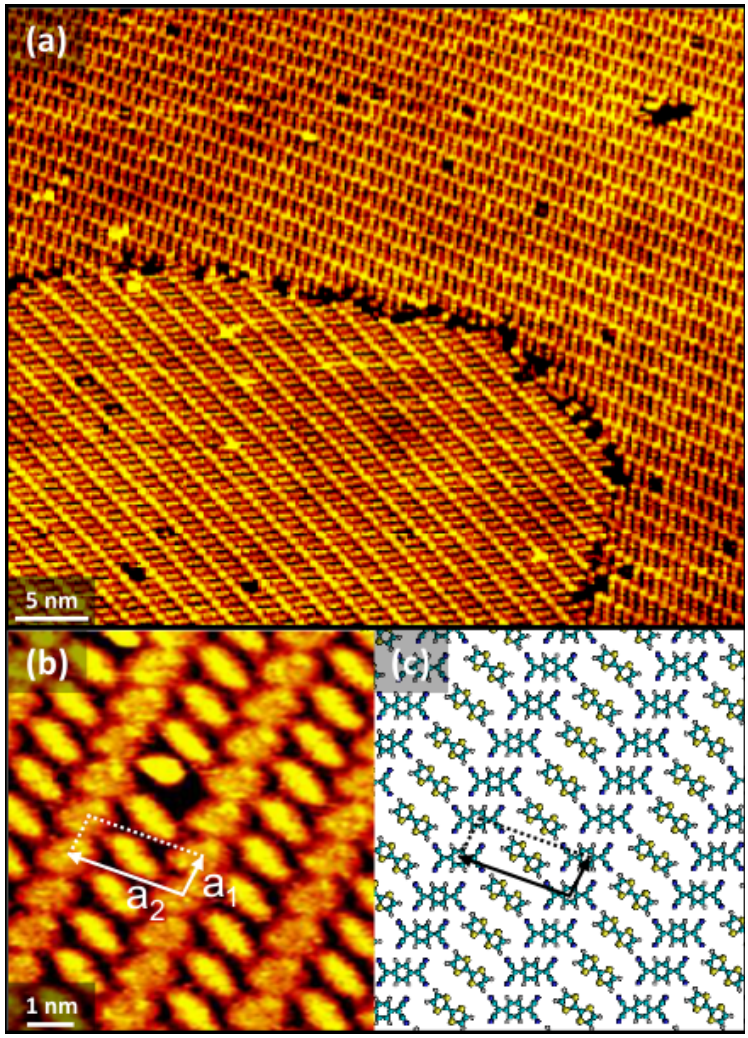

Figure 3.12: *(a) STM image of large scale (50x42nm^2) self-assembled domain with equal amount of TCNQ and TTF molecule in 1:1 stoichiometry (I_t=-0.34nA $V_t = -1520mV$); (b) Detail of TTF 1:1 TCNQ mixed phase with intra-molecular resolution (I_t=-0.11nA $V_t = -430mV$); (c) adsorption model of TTF 1:1 TCNQ mixed phase on Au(111) surface*

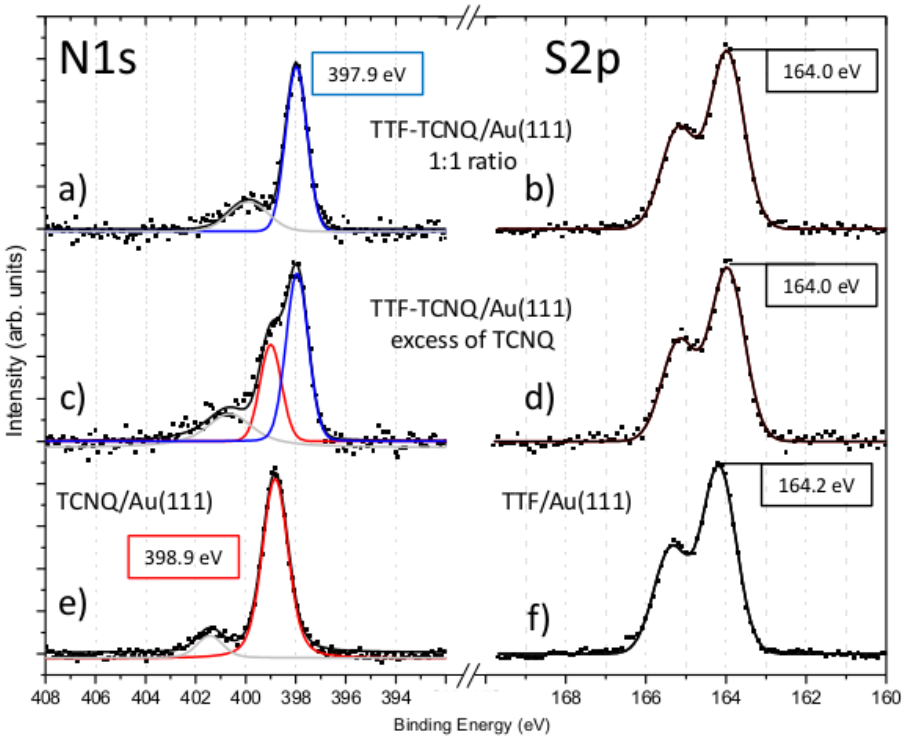

Figure 3.13: *upper pannel:(a-b)N1s and S2p XP spectra of about 1ML of TTF-TCNQ in 1:1 stoichiometry. The N1s spectrum, relatively to TCNQ molecules, is deconvoluted into a single peak centered at 397.9 eV plus a shake-up satellite; the S2p spectrum, relatively to TTF molecules, is represented by single peak at 164.0 eV with doublet separation of 1.18eV; (c-d) N1s ans S2p XP spectra of a sample prepared with an excess of TCNQ molecules that leads to contemporary presence of islands of TTF-TCNQ in 1:1 stoichiometry and pure TCNQ on Au(111) surface. The N1s XP spectrum can be deconvoluted as the sum of two component, each one reflecting the different chemical environments of TCNQ: the blue curve is centered at 397.9 eV, same value found for a complete monolayer of TTF-TCNQ plus red curve centered at 398.9 eV associate to TCNQ/Au(111). The S2p spectrum is identical in shape and position to b) spectrum, reflecting the situation that all TTF molecules present on surface are involveld in the formation of TTF-TCNQ phase; (e-f)N1s and S2p spectra of individual adsorption of TCNQ and TTF on Au(111) surface. The N1s is centered at 398.9 eV while the S2p at 164.2 eV*

TCNQ, and the surplus of TCNQ remains in homomolecular regions. No other structures were observed in the formation of the overlayer structure depending on the relative amount of each constituents on Au(111) surface.

Figure 3.13 shows the photoemission spectra of N_{1s} and S_{2p} of TCNQ and TTF respectively of different samples in order to underline the differences. Figure 3.13a and b show the photoemission spectra of N_{1s} and S_{2p} of almost 1ML of TTF-TCNQ mixture in 1:1 stoichiometry (STM images in fig.3.12). The N_{1s} XP spectrum relatively TCNQ clearly evidences one peak at 397,9 eV plus a shake-up satellite. The shift towards lower binding energy of N_{1s} is measured to be 1.0 eV with respect to neutral physisorbed TCNQ as shown in fig.3.13e. The direction of shift is compatible with the assumption that TCNQ molecules become negative charged once co-adsorbed with TTF molecules.
On the other hand the characteristic spin-orbit doublet of S_{2p} of fig.3.13b is centered at 164.0 eV (DS=1.18 eV). This value is not so different for what we measured in the case of TTF on Au(111) surface, that is characterized by the position in binding energy of the peak at 164.2 eV as shown in fig.3.13f. The experimentally observed shift of S_{2p} is towards lower binding energy, the opposite direction that we expect if TTF was donating electrons to TCNQ in the mixed phase. This suggests that the extra negative charge in TCNQ acceptor molecules does not come from TTF donor molecule.
Figure3.13c and d show the XP spectra relative to a sample prepared co-depositing TCNQ and TTF with an excess of TCNQ around islands of TTF-TCNQ in 1:1 stoichiometry. It is interesting to note that the spectrum of N_{1s} in fig.3.13c can be deconvoluted as the sum of two peaks reflecting the different chemical environments of TCNQ. One component is at 398.9 eV is associated to the excess of TCNQ in its physisorbed state on Au(111) surface (red spectrum, see fig.3.13e), and the second peak at 397.9 eV, associated to TTF-TCNQ sub-monolayer islands (blue spectrum, see fig.3.13a). The S_{2p} spectrum of this sample evidences only one component at 164.0 eV, confirming that all TTF molecules are involved in the formation of TTF-TCNQ phase.

Figure3.14 shows a comparison between the carbon XP spectra of the single molecules individually adsorbed on Au(111) surface and a complete monolayer of TTF-TCNQ in 1:1 ratio. In the bottom panel of figure3.14 is shown the C_{1s} spectrum of TCNQ/Au(111). As previously discussed, TCNQ can be considered in its neutral state once adsorbed on gold surface and it characterized by the two peaks, one at 285.9 eV and another at 284.5 eV with ratio $\sim$ 1:1, reflecting the different chemical environments of carbon atoms. The central panel shows the C_{1s} spectrum of TTF/Au(111) represented by a single peak centered at 285.3 eV. The upper panel shows the C_{1s} of a complete monolayer of TTF-TCNQ in

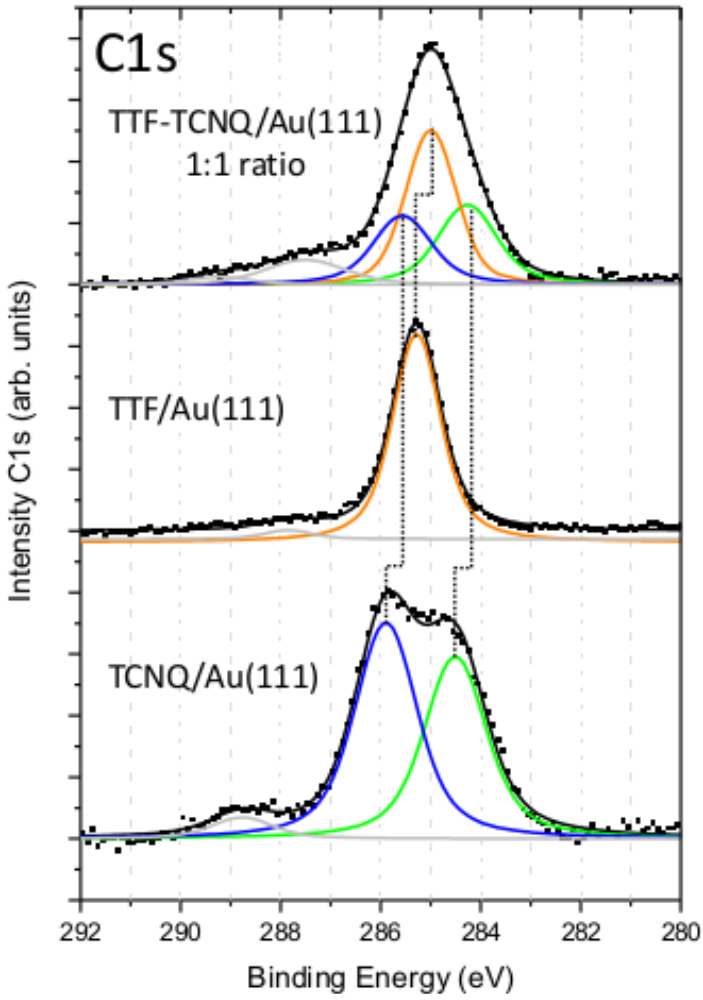

Figure 3.14: *Comparison of C1s XP spectra of TCNQ (bottom panel) and TTF (middle panel) individually adsorbed on Au(111) surface and a complete monolayer of TTF-TCNQ in 1:1 ratio (upper panel). A possible deconvolution of the latter peak, take into account the three components identified in individual deposition of both constituents, that appears rigidly shifted of ∼0.3 eV towards binding energy. The tail at higher binding energy of the peak is well fitted by two shake-up satellites.*

1:1 ratio. The main peak appears quite larger with a FWHM of $\sim$ 1.7 eV. A possible deconvolution of the peak into various components was done keeping in mind that neither evidence of changes in the chemical structures of both constituents were observed in STM images nor they are expected. Therefore we tried the deconvolution using the same components found for the C_{1s} spectra for TTF and TCNQ. The three components fit very well the experimental data and they result rigidly shifted of $\sim$0.3 eV towards binding energy. The tail at higher binding energy of the peak is well fitted by two shake-up satellites, approximatively to the same positions found for TTF and TCNQ respectively.

3.5 Discussion

From the experimental data discussed so far, the behaviour of TTF-TCNQ monolayer appears different from that observed in bulk phase, both from structural and electronic point of view. Even though the molecules are organized in homomolecular rows of TTF and TCNQ similar to the bulk distribution, the constriction imposed by the Au(111) surface makes the adsorption of molecules planar with a small difference in the dimensions of unit cell. From electronic point of view, in bulk the charge transferred occurs from the donor to the acceptor molecules. In monolayer phase we do not observe an opposite shift in binding energy between N_{1s} and S_{2p}. It means that the excess of negative charge that TCNQ shows in mixed phase with respect homomolecular phase does not come from TTF, otherwise we should measure a shift towards higher binding energy of S_{2p} as in the case of Fe donor centers in the MOCN. A possible mechanism able to explain this behaviour is that TCNQ accepts electrons not directly from TTF, but from gold substrate through the action of TTF molecules that will act as a sort of bridge between gold and TCNQ. Notice that in absence of TTF, TCNQ is not able to acquire such amount of charge from the substrate, as proved by the complementary STM and XPS study of individually TCNQ molecules on Au(111) surface. The small shift towards lower binding energy observed for S_{2p} of TTF in the mixed phase with respect to homomolecular deposition is probably due to screening effect of the excess of charge in TCNQ molecules.

Also the amount of transferred charge to TCNQ appears different with respect to bulk structure. As previously discussed, the pure organic CT complex TTF-TCNQ has only a fractional charge transfer (0.59 e^-) in the solid crystal[49], which is delocalized in extended electron bands along molecular π stacks[33]. Nevertheless Torrente *et al.*[57] have shown that a single molecular

layer of the TTF-TCNQ complex grown on a Au(111) surface exhibits a spin $-\frac{1}{2}$ degenerate ground state that is a free-radical state. The proof is the observation of the Kondo effect in transport experiment through the spectroscopic evidence using scanning tunneling microscope. They found that an unpaired electron is localized in a π orbital of the TCNQ molecules, which interacts very weakly with the underlying metal surface. Because of its π character, the unpaired electron appears strongly coupled to molecular vibrations, leading to the split of the Kondo resonance in various vibrational sidebands. The shift of 1 eV towards lower binding energy that we found for N_{1s} core level in TTF-TCNQ monolayer with respect to neutral TCNQ on Au(111) goes in this direction and fixes a reference value for N_{1s} binding energy.

Further comparison is relative to the substrates. In our group the same charge-transfer complex was studied on Ag(111)[58]. It was found that individually adsorption of TTF and TCNQ have an opposite behaviour for what found in this work. In fact, it was found that TCNQ strongly interact with silver surface becoming negative charge upon the adsorption on silver substrate. The calculations indicate that the molecule gets ~ 0.99 e^- from the silver substrate and the N_{1s} is centered at 398.3 eV in binding energy, in contrast with 398.9 eV found for N_{1s} for TCNQ/Au(111). On the other hand TTF molecules on Ag(111) surface show lower interaction donating 0.13 e^- per molecule to the silver substrate in contrast with the 0.6 e^- calculated for Au(111)[36]. The peak of S_{2p} for TTF/Ag(111) is centered at 164.5 eV while for TTF/Au(111) is at 164.2 eV. In other words TCNQ molecules interact more strongly with silver than with the gold surface and, on the other hand, TTF molecules donate more negative charge to Au(111) than to Ag(111), as shown by the the relative positions in binding energy registered by the XPS measurements. When both TTF and TCNQ are mixed on Ag(111) surface, they show four different phases depending on the relative amount of each molecules adsorbed on the surface, in contrast to the only mixed phase observed on Au(111) surface. The XPS results of the mixed phases on Ag(111) suggest that the negative charge in the TTF molecules increases, despite its donor character, with the TCNQ content. In fact, both C_{1s} and S_{2p} core levels shift to lower binding energy with excess of TCNQ, while the N_{1s} core level does not shift appreciably due to the strong interaction of TCNQ molecuels with the surface. This behaviour is opposite to what observed for the mixed phase on Au(111), where the S_{2p} substantially does not shift appreciably because TTF strongly interacts with the gold surface, while both C_{1s} and N_{1s} shift to lower binding energy indicating a charge transfer to TCNQ molecules. The difference of the behaviour of individually TCNQ and TTF molecules and their mixed phase on different substrates could

be explained considering that the interaction with the surface is predominant with respect to donor/acceptor character of the individual building blocks. This would suggests that in a mixed surface phase, independently from the individual character of the molecule in gas phase, the molecule that interacts less strongly with the surface is more able to receive and host electrons.

Final consideration regards the different nature of the charge transfer observed for TCNQ molecules in the supramolecular structures obtained by the intermixing of two different donor species on Au(111) surface. In the 2D-CT complex, one entire electron, responsible for the Kondo effect experimentally observed, is transferred from the substrate to TCNQ through the presence of TTF molecules which act as a kind of bridge between gold and TCNQ. For the 2D-MOCN the process of charge transfer occurs through the formation of coordination bonds between one iron atom and the dicyanomethylene groups through σ-donation π-backdonation mechanism. On the other hand, the initial physisorbed supramolecular islands of TCNQ do not interact strongly with the Au(111) surface and the TCNQ molecules can be considered almost neutral. Thus, TCNQ molecules can experience different quantities of negative charge on Au(111) surface by changing the specie with which TCNQ will self assemble at room temperature. The measure of the different negative charge is given by the relative positions of the peak in binding energy of nitrogen atoms into dicyanomethylene groups which give the electrophilic character to TCNQ molecule. Figure 3.15 shows the N1s XP spectra of TCNQ in the different supramolecular structure environments studied in this chapter. The range of extra charge accommodate in the TCNQ goes from zero as can be considered the homomolecular regions of TCNQ (398.9 eV red spectrum), to one as confirmed by the unpaired electron responsible for the experimental observation of Kondo effect in TTF-TCNQ mixed phase(397.9 eV blue spectrum). The Fe-TCNQ coordination network shows an intermediate value of N_{1s} binding energy (398.4 eV green spectrum). It might be reasonable suppose an electron donation of $\sim$0.5 e^- from Fe centers to TCNQ molecules, but the iron atoms involved in the coordination bond show a +3 oxidation state. The undistributed charge it might produce a screening effect masking the effective electron donation to TCNQ. In any case, it is important to underline the fact that depositing TCNQ molecules on Au(111) and mixing them with different entities we are able to modulate with a precision of $\pm$0.5 eV the total quantity of negative charge experienced by nitrogen in TCNQ molecules.

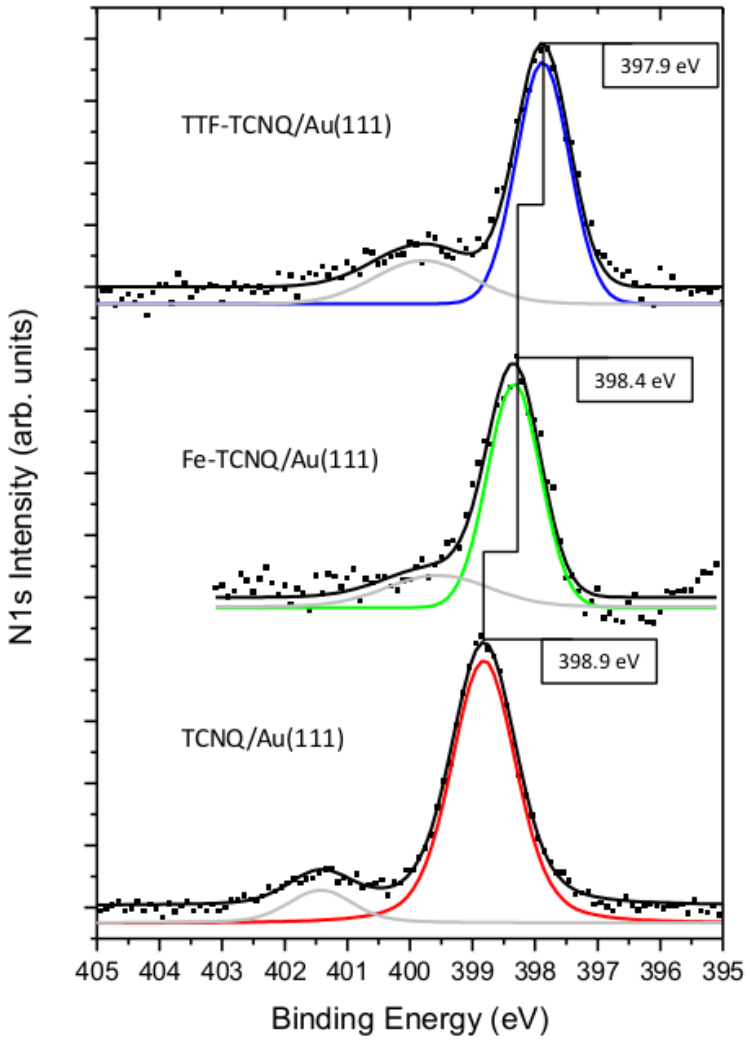

Figure 3.15: *Comparison between the N1s XP spectra of TCNQ in different environments on the same Au(111) surface leads to a modulation of the negative charged experienced by the TCNQ molecules as shown by the shifts in binding energy of the supramolecular superstructures studied in this work.*

3.6 Conclusions

In this chapter we studied different supramolecular structures obtained by intermixing of organic acceptor TCNQ molecules with two different donor species: metallic iron atoms and TTF molecule. In a first step the structural and electronic properties of TCNQ adsorbed on Au(111) reconstructed surface was studied. TCNQ molecules physisorb on gold substrate and self-assemble in highly ordered islands stabilized through hydrogen bonds between cyano groups and benzene rings (C≡N$\cdots$H-C). The physisorbed state, characterized by the lack of a true chemical bond between adsorbate and substrate, does not favour the natural tendency of TCNQ to accept charge, i.e. from the substrate in this case. Therefore TCNQ is considered essentially neutral on the Au(111) surface.

The addition of Fe atoms on Au(111) surface precovered with TCNQ monolayer leads to the formation of surface MOCN. The complete coordination of one monolayer of TCNQ is experimentally observed at a coverage of θ_{Fe}=0.18±0.05 ML, that represent the stoichiometric amount needed to coordinate a complete monolayer of TCNQ on Au(111). In the structural model that we proposed, one Fe atom is coordinated to four nitrogen atoms, each one belonging to a distinct cyano group and so to four distinct molecules. The addition of Fe atoms lowers the binding energies of N_{1s} of 0.5 eV with respect to neutral TCNQ. On the other side the Fe_{2p} shows a shift towards higher binding energy that is assigned in literature to a +2 or +3 oxidation state of iron. Such oxidation is due to the interaction with TCNQ molecules, since no presence of oxygen or any other contaminations was detected by the XPS survey.

The other donor specie is the organic molecule TTF, that forms surface patterned lattice based on long-range repulsive interaction of electrostatic nature upon charge transfer with the surface. The estimation of the electron donation from Au(111) is ∼0.6 e^-, which is indicative of strong interaction with the substrate. Deposition of donor TTF and acceptor TCNQ on Au(111) surface leads to a mixed structure with stoichiometry TTF 1:1 TCNQ. No other phases were observed for TTF-TCNQ on Au(111) surface depending on the concentration of the constituents as reported on other surface like Ag(111). We found for the 1:1 phase that N_{1s} shows a larger shift of 1.0 eV to lower binding energy with respect to TCNQ/Au(111). The S_{2p} as well is slightly shifted of ∼0.2 eV towards lower binding energy with respect to homo-molecular TTF adlayer. Such behaviour is counterintuitive for a donor-acceptor charge transfer complex. The mechanism that we proposed is that TTF molecules act as a kind of bridge between gold substrate and TCNQ molecules, since the latter are not able to obtain directly electrons from the substrate.

Finally, it is worth noting that TCNQ molecules can experience different negative charges on Au(111) surface by mixing and self assembling them with organic and metallic donor species. In fact with controlled deposition of the donor, it is possible to modulate with a precision of ± 0.5 eV the binding energy if N_{1s}, and so the negative charge experienced by nitrogen in TCNQ molecules. This make us able to discriminate three different charge states that can affect the charge transport on the same substrate for the realization of electronic nanodevices.

Bibliography

[1] Roberto Otero, José María Gallego, Amadeo L Vázquez de Parga, Nazario Martín, and Rodolfo Miranda. Molecular self-assembly at solid surfaces. *Advanced Materials*, 23(44):5148–5176, 2011.

[2] Johannes V Barth, Giovanni Costantini, and Klaus Kern. Engineering atomic and molecular nanostructures at surfaces. *Nature*, 437(7059):671–679, 2005.

[3] Johannes V Barth. Molecular architectonic on metal surfaces. *Annu. Rev. Phys. Chem.*, 58:375–407, 2007.

[4] Maya Schöck, Roberto Otero, Sladjana Stojkovic, Frauke Hümmelink, André Gourdon, Erik Lægsgaard, Ivan Stensgaard, Christian Joachim, and Flemming Besenbacher. Chiral close-packing of achiral star-shaped molecules on solid surfaces. *The Journal of Physical Chemistry B*, 110(26):12835–12838, 2006.

[5] Johannes V Barth. Fresh perspectives for surface coordination chemistry. *Surface Science*, 603(10):1533–1541, 2009.

[6] Sebastian Stepanow, Magalí Lingenfelder, Alexandre Dmitriev, Hannes Spillmann, Erik Delvigne, Nian Lin, Xiaobin Deng, Chengzhi Cai, Johannes V Barth, and Klaus Kern. Steering molecular organization and host–guest interactions using two-dimensional nanoporous coordination systems. *Nature materials*, 3(4):229–233, 2004.

[7] Davide Bonifazi, Stefan Mohnani, and Anna Llanes-Pallas. Supramolecular chemistry at interfaces: molecular recognition on nanopatterned porous surfaces. *Chemistry-A European Journal*, 15(29):7004–7025, 2009.

[8] Roberto Otero, Frauke Hümmelink, Fernando Sato, Sergio B Legoas, Peter Thostrup, Erik Lægsgaard, Ivan Stensgaard, Douglas S Galvão, and Flemming Besenbacher. Lock-and-key effect in the surface diffusion of large organic molecules probed by stm. *Nature materials*, 3(11):779–782, 2004.

[9] Christian Urban. Structural and chemical effects of charge transfer across metal organic interfaces. 2012.

[10] LR Melby, RJ Harder, WR Hertler, W Mahler, RE Benson, and WE Mochel. Substituted quinodimethans. ii. anion-radical derivatives and

complexes of 7, 7, 8, 8-tetracyanoquinodimethan. *Journal of the American Chemical Society*, 84(17):3374–3387, 1962.

[11] Andrew Zangwill. *Physics at surfaces*. Cambridge University Press, 1988.

[12] Isabel Fernández Torrente, Katharina J Franke, and Jose Ignacio Pascual. Structure and electronic configuration of tetracyanoquinodimethane layers on a au (111) surface. *International Journal of Mass Spectrometry*, 277(1):269–273, 2008.

[13] John M Lindquist and John C Hemminger. High-resolution core level photoelectron spectra of solid tcnq: determination of molecular orbital spatial distribution from localized shake-up features. *The Journal of Physical Chemistry*, 92(6):1394–1396, 1988.

[14] John M Lindquist and John C Hemminger. High energy resolution x-ray photoelectron spectroscopy studies of tetracyanoquinodimethane charge transfer complexes with copper, nickel, and lithium. *Chemistry of Materials*, 1(1):72–78, 1989.

[15] T Nakayama, K Inamura, Y Inoue, S Ikeda, and K Kishi. Adsorption of benzonitrile and alkyl cyanides on evaporated nickel and palladium films studied by xps. *Surface science*, 179(1):47–58, 1987.

[16] Alan D McNaught and Alan D McNaught. *Compendium of chemical terminology*, volume 1669. Blackwell Science Oxford, 1997.

[17] Sebastian Stepanow, Nian Lin, and Johannes V Barth. Modular assembly of low-dimensional coordination architectures on metal surfaces. *Journal of Physics: Condensed Matter*, 20(18):184002, 2008.

[18] Bence Lazarovits, Laszlo Szunyogh, and Peter Weinberger. Spin-polarized surface states close to adatoms on cu (111). *Physical Review B*, 73(4):045430, 2006.

[19] Alexander Langner, Steven L Tait, Nian Lin, Chandrasekar Rajadurai, Mario Ruben, and Klaus Kern. Self-recognition and self-selection in multicomponent supramolecular coordination networks on surfaces. *Proceedings of the National Academy of Sciences*, 104(46):17927–17930, 2007.

[20] Dirk Kühne, Florian Klappenberger, Wolfgang Krenner, Svetlana Klyatskaya, Mario Ruben, and Johannes V Barth. Rotational and constitutional dynamics of caged supramolecules. *Proceedings of the National Academy of Sciences*, 107(50):21332–21336, 2010.

[21] Pietro Gambardella, Sebastian Stepanow, Alexandre Dmitriev, Jan Honolka, Frank MF de Groot, Magalí Lingenfelder, Subhra Sen Gupta, DD Sarma, Peter Bencok, Stefan Stanescu, et al. Supramolecular control of the magnetic anisotropy in two-dimensional high-spin fe arrays at a metal interface. *Nature Materials*, 8(3):189–193, 2009.

[22] Tzu-Chun Tseng, Nasiba Abdurakhmanova, Sebastian Stepanow, and Klaus Kern. Hierarchical assembly and reticulation of two-dimensional mn-and ni–tcnq x (x= 1, 2, 4) coordination structures on a metal surface. *The Journal of Physical Chemistry C*, 115(20):10211–10217, 2011.

[23] Marisa N Faraggi, Nan Jiang, Nora Gonzalez-Lakunza, Alexander Langner, Sebastian Stepanow, Klaus Kern, and Andres Arnau. Bonding and charge transfer in metal–organic coordination networks on au (111) with strong acceptor molecules. *The Journal of Physical Chemistry C*, 116(46):24558–24565, 2012.

[24] John F Moulder, Jill Chastain, and Roger C King. *Handbook of X-ray photoelectron spectroscopy: a reference book of standard spectra for identification and interpretation of XPS data*. Perkin-Elmer Eden Prairie, MN, 1992.

[25] Toru Yamashita and Peter Hayes. Analysis of xps spectra of fe 2+ and fe 3+ ions in oxide materials. *Applied Surface Science*, 254(8):2441–2449, 2008.

[26] AP Grosvenor, BA Kobe, MC Biesinger, and NS McIntyre. Investigation of multiplet splitting of fe 2p xps spectra and bonding in iron compounds. *Surface and Interface Analysis*, 36(12):1564–1574, 2004.

[27] Naoki Toyota, Michael Lang, and Jens Müller. *Low-dimensional molecular metals*, volume 154. Springer Science & Business Media, 2007.

[28] Vita Solovyeva. *TTF-TCNQ-based thin films and microcrystals-growth and charge transport phenomena*. PhD thesis, 2011.

[29] Markus Schwoerer, Hans Christoph Wolf, and William D Brewer. *Organic molecular solids*, volume 80. Wiley Online Library, 2007.

[30] F Wudl, GM Smith, and EJ Hufnagel. Bis-1, 3-dithiolium chloride: an unusually stable organic radical cation. *Journal of the Chemical Society D: Chemical Communications*, (21):1453–1454, 1970.

[31] R Zahradnik, P Carsky, S Hünig G Kiesslich, and D Scheutzow. Conjugated radicals. vil* tetrathiofulvalene and a note on sulfur-containing conjugated radicals. *International journal of sulfur chemistry: Mechanisms of reactions of sulfur compounds*, 6:109, 1971.

[32] David L Coffen, James Q Chambers, Denis R Williams, PE Garrett, and ND Canfield. Tetrathioethylenes. *Journal of the American Chemical Society*, 93(9):2258–2268, 1971.

[33] Jordi Fraxedas. *Molecular organic materials: from molecules to crystalline solids*. Cambridge University Press, 2006.

[34] Nazario Martín. Tetrathiafulvalene: the advent of organic metals. *Chemical Communications*, 49(63):7025–7027, 2013.

[35] J Fraxedas, Sandra García-Gil, S Monturet, N Lorente, I Fernández-Torrente, KJ Franke, JI Pascual, A Vollmer, R-P Blum, N Koch, et al. Modulation of surface charge transfer through competing long-range repulsive versus short-range attractive interactions. *The Journal of Physical Chemistry C*, 115(38):18640–18648, 2011.

[36] I Fernandez-Torrente, Serge Monturet, KJ Franke, J Fraxedas, Nicolas Lorente, and JI Pascual. Long-range repulsive interaction between molecules on a metal surface induced by charge transfer. *Physical review letters*, 99(17):176103, 2007.

[37] F Wennmohs, V Staemmler, and Michael Schindler. Theoretical investigation of weak hydrogen bonds to sulfur. *The Journal of chemical physics*, 119(6):3208–3218, 2003.

[38] CJ Olson Reichhardt, Charles Reichhardt, and Alan R Bishop. Fibrillar templates and soft phases in systems with short-range dipolar and long-range interactions. *Physical review letters*, 92(1):016801, 2004.

[39] Giulia Tomba, Massimiliano Stengel, Wolf-Dieter Schneider, Alfonso Baldereschi, and Alessandro De Vita. Supramolecular self-assembly driven by electrostatic repulsion: the 1d aggregation of rubrene pentagons on au (111). *ACS nano*, 4(12):7545–7551, 2010.

[40] Christian Urban, David Ecija, Yang Wang, Marta Trelka, Iulian Preda, Antje Vollmer, Nicolás Lorente, Andrés Arnau, Manuel Alcamí, Leonardo Soriano, et al. Growth and structure of self-assembled monolayers of a ttf

derivative on au (111). *The Journal of Physical Chemistry C*, 114(14):6503–6510, 2010.

[41] M Zharnikov and M Grunze. Spectroscopic characterization of thiol-derived self-assembling monolayers. *Journal of Physics: Condensed Matter*, 13(49):11333, 2001.

[42] Eisuke Ito, Jaegeun Noh, and Masahiko Hara. Different adsorption states between thiophene and α-bithiophene thin films prepared by self-assembly method. *Japanese journal of applied physics*, 42(7B):L852, 2003.

[43] John Ferraris, DO Cowan, V t Walatka, and JH Perlstein. Electron transfer in a new highly conducting donor-acceptor complex. *Journal of the American Chemical Society*, 95(3):948–949, 1973.

[44] GA Thomas, DE Schafer, F Wudl, PM Horn, D Rimai, JW Cook, DA Glocker, MJ Skove, CW Chu, RP Groff, et al. Electrical conductivity of tetrathiafulvalenium-tetracyanoquinodimethanide (ttf-tcnq). *Physical Review B*, 13(11):5105, 1976.

[45] Isabel Fernández Torrente. *Local Spectroscopy of bi-molecular assemblies: screening, charge transfer, and magnetism at the molecular scale.* PhD thesis, 2008.

[46] Keizo Murata, Seiichi Kagoshima, Syuma Yasuzuka, Harukazu Yoshino, and Ryusuke Kondo. High-pressure research in organic conductors. *Journal of the Physical Society of Japan*, 75(5), 2006.

[47] Thomas J Kistenmacher, TERRY E Phillips, and Dwaine O Cowan. The crystal structure of the 1: 1 radical cation–radical anion salt of 2, 2'-bis-l, 3-dithiole (ttf) and 7, 7, 8, 8-tetracyanoquinodimethane (tcnq). *Acta Crystallographica Section B: Structural Crystallography and Crystal Chemistry*, 30(3):763–768, 1974.

[48] Norihiko Ara, Akira Kawazu, Hidemi Shigekawa, Kiyoshi Yase, and Masamichi Yoshimura. Structural studies of tetrathiafulvalene–tetracyanoquinodimethane thin films by scanning tunneling microscopy. *Applied physics letters*, 66(24):3278–3280, 1995.

[49] Denis Jérome. Organic conductors: From charge density wave ttf-tcnq to superconducting (tmtsf) 2pf6. *Chemical reviews*, 104(11):5565–5592, 2004.

[50] M Sing, Udo Schwingenschlögl, R Claessen, Peter Blaha, JMP Carmelo, LM Martelo, PD Sacramento, M Dressel, and Claus Schelde Jacobsen. Electronic structure of the quasi-one-dimensional organic conductor ttf-tcnq. *Physical Review B*, 68(12):125111, 2003.

[51] F Zwick, D Jérome, G Margaritondo, M Onellion, J Voit, and M Grioni. Band mapping and quasiparticle suppression in the one-dimensional organic conductor ttf-tcnq. *Physical review letters*, 81(14):2974, 1998.

[52] TR Umbach, I Fernandez-Torrente, JN Ladenthin, JI Pascual, and KJ Franke. Enhanced charge transfer in a monolayer of the organic charge transfer complex ttf–tnap on au (111). *Journal of Physics: Condensed Matter*, 24(35):354003, 2012.

[53] CH Schwalb, S Sachs, M Marks, A Schöll, F Reinert, E Umbach, and U Höfer. Electron lifetime in a shockley-type metal-organic interface state. *Physical review letters*, 101(14):146801, 2008.

[54] F Jäckel, UGE Perera, V Iancu, K-F Braun, N Koch, JP Rabe, and S-W Hla. Investigating molecular charge transfer complexes with a low temperature scanning tunneling microscope. *Physical review letters*, 100(12):126102, 2008.

[55] K Clark, A Hassanien, S Khan, K-F Braun, H Tanaka, and S-W Hla. Superconductivity in just four pairs of (bets) 2gacl4 molecules. *Nature nanotechnology*, 5(4):261–265, 2010.

[56] N Gonzalez-Lakunza, I Fernandez-Torrente, KJ Franke, N Lorente, Andrés Arnau, and JI Pascual. Formation of dispersive hybrid bands at an organic-metal interface. *Physical review letters*, 100(15):156805, 2008.

[57] I Fernández-Torrente, KJ Franke, and JI Pascual. Vibrational kondo effect in pure organic charge-transfer assemblies. *Physical review letters*, 101(21):217203, 2008.

[58] Jonathan Rodríguez Fernández. *Donor and Acceptor Molecules on Metal Surfaces: Supramolecular Self-Assembly, Metal-Organic Coordination Networks, and Charge-Transfer Complexes*. PhD thesis, 2014.

Chapter 4

Modification of metallic growth on Au(111) surface.

This chapter is focused on the study of the growth mechanism of iron on Au(111) surface. Starting from the scheme of growth reported by similar works, we have observed modifications of the expected growth. The factors that introduce such modifications are, on one hand the kinetic and thermodynamic limitations, on the other hand the presence of a monolayer of organic acceptor TCNQ molecule as modifier for Fe growth. The results are discussed considering both structural and electronic properties of the systems under investigation.

4.1 Introduction to heteroepitaxial growth

The heteroepitaxial growth of thin films on metal substrates is of fundamental interest for different branches in natural sciences and technological fields. Physical and chemical properties of these systems are particularly influenced by the interface with the underlying substrate[1]. Progresses in fields such as catalysis and magnetic nanostructures are critically dependent on the ability to prepare uniformly dispersed clusters with controlled characteristics[2]. The desired morphology depends on the specific application, for example, in some device applications it is important to be able to form regular arrays of nearly identical islands[3]. Understanding the basic mechanisms underlying cluster nucleation at surfaces[4], as well as those that could change an eventual ordered pattern[5], is essential in order to achieve control over the nanostructures.

The growth of films on the substrates is controlled by the interplay of thermodynamic and kinetic effects. In 1958, Ernst Bauer[6] introduced a classification of epitaxial growth modes based on thermodynamic considerations. When metal atoms are condensed on the surface of other metal, different growth modes may be distinguished according to the balance between the surface free energy γ_D of the deposited material, the surface free energy γ_S of the substrate, and the interface free energy $\gamma_{int} = \gamma_S + \gamma_D - \beta_{SD}$ where β_{SD} is the work required to separate substrate and deposit. In thermodynamical equilibrium, the growth morphology is determined by the balance of free energies involved in the process.

$$\Delta\gamma_{total} = \gamma_S + \gamma_{int} - \gamma_D \tag{4.1}$$

Three growth modes are identified in fig.4.1, depending on the balance of energy.

- $\Delta\gamma_{total} \leq 0$
  In this condition, the atoms of the deposited material are more strongly bound to the substrate than to each other. For that reason, the adotms tend to form a complete monolayer on the surface. For further deposition, each layer is fully completed before the next layer starts to grow. Therefore a 2D layer by layer growth, or *Frank-van der Merve*, takes place[7].

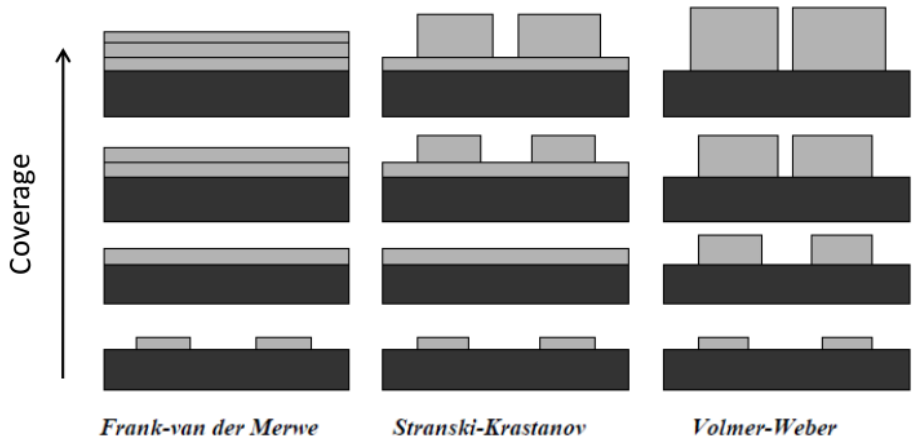

Figure 4.1: *The three epitaxial growth mechanisms: Layer by layer or Frank-van der Merve, Layer plus islands or Stranski-Krastanov, Islands Vollmer-Weber growth mode in function of the balance of free energy.*

- After the growth of one or more layers on the surface, the planar growth of further layer could become energetically unfavorable. Therefore from this point, the adatoms will condensate in 3D islands on top of the intermediated layer(s). This scenario defines the layer plus islands, or *Stranski-Krastanov*, growth mode[8]. This mode is typical of heteroepitaxial systems, for which $\gamma_D << \gamma_S$ and/or large misfit of lattice constants between adsorbed and substrate. After deposition of a certain number of layer, the chemical influence of the original substrate will be largely screened and $\gamma_S \approx \gamma_D$. However, the elastic influence of the original substrate will give rise to a positive, nonzero interface energy γ_{int} between layer n and $n+1$. At a given point the elastic energy accumulated in the film makes that $\Delta\gamma_{total} > 0$. From this moment, the deposited material condensates in 3D clusters, which its own bulk structure[9].

- $\Delta\gamma_{total} > 0$
  It is the case when film atoms are more strongly bound to each other than to substrate, therefore the growth will lead to the formation of three-dimensional islands on the substrate. This mode is named islands or *Volmer-Weber* growth mode[10].

In addition to these considerations, growth process occurs at conditions which are always far from equilibrium and the kinetic limitations, associated with the finite rates of mass transport processes, can greatly affect the actual growth mode. There are two diffusion processes of interest: intra-layer mass transport,

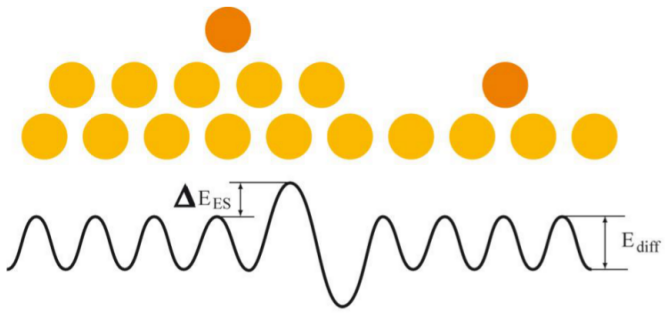

Figure 4.2: *A schematic image of potential surface topography near a stage. ΔE_{ES} is the Ehrlich-Schwoebel barrier that the atom on the surface (a dark circle) has to bridge in addition to the E_{diff} diffuse barrier on the terrace in order to cross the edge of stage and descend to the lower terrace.*

i.e. diffusion of atoms on a flat terrace, and inter-layer mass transport, i.e. diffusion of atoms across a step edge.
To characterize the inter layer transport let us consider the shape of the potential energy curve for an adatom near a step as shown in fig.4.2. A diffusing adatom in the lower terrace would stick to the step edge since in this position it has higher coordination and, hence, a higher binding energy: therefore upward diffusion is usually neglected. On the other hand, an adatom reaching the step edge from an upper terrace encounters a barrier to cross at lower terrace. The extra energy barrier E_{ES}, that needs to be added to the normal diffusion barrier in order for the atom to go move from the upper to the lower terrace, is known as the Erlich-Schwoebel barrier[11, 12]. It appears clearly that higher ES barrier leads to less efficient inter layer transport. Depending on the relative rate of inter and intra layer mass transport the kinetics effects can influence the growth according to one of the three possible growth modes schematized in fig.4.3. Step flow mode takes place when the growth proceeds under conditions close to equilibrium. In this case the intra-layer mobility is extremely high (low E_{diff} barrier) and all adatoms reach the step before the nucleation on the terrace sets in. If the terrace width exceeds the adatom diffusion length, the growth proceeds via nucleation and growth of islands on terraces. In this case, depending on the rate of inter-layer mass transport, layer-by-layer growth or multilayer growth take

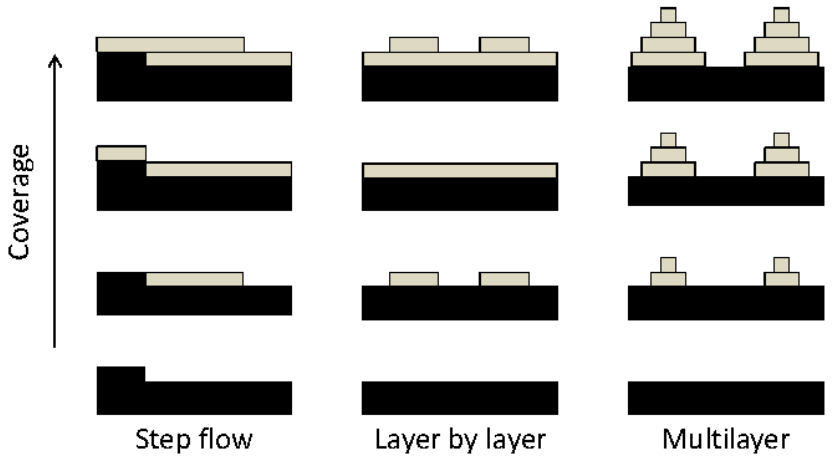

Figure 4.3: *Three Modes of growth: step-flow, layer-by-layer and multilayer growth.*

place. Layer-by-layer growth requires a sufficient inter-layer mass transport to ensure that all atoms, which are deposited onto the top of the growing island, would reach the island edge and jump to the lower layer before new adatoms are adsorbed on the island. Ideally a new layer starts to grow only after the previous layer has been entirely completed. If the inter-layer mass transport is suppressed, the adatoms cannot escape from the top of the island and promote there the earlier nucleation of the new layer. As a result, multilayer 3D growth takes place[13]

A more detailed theory of growth includes the new atomistic processes discovered in the last decades examining the initial stages of the growth of metals on metallic substrates. These phenomena include, among others, surface intermixing of bulk immiscible metals[14], preferential nucleation at certain features of surface reconstruction[15], relaxing strain[16] and surface diffusion by atomic exchange processes[17]. In particular the place exchange process can lead to the formation of a floating substrate layer that, in same case, acts as a surfactant for the growth of the deposited metals[18, 19]or to the formation of surface alloys with influent changes in catalytic activity[20]. In the following section we will focus our attention on the growth of iron on the clean Au(111) surface, looking for analogies and differences with similar systems.

4.2 Growth of Fe on Au(111)

The growth of ordered arrays of metal clusters supported on surfaces is of extreme interest both from a fundamental and a technological point of view. Nanoislands on nanopatterned surfaces are promising model systems due to their ability to self-organize over a very large scale[21]. The Au(111) surface represents an interesting and peculiar substrate for growing thin films due to its herringbone reconstruction that provides a natural template. The strain induced by the herringbone reconstruction plays also a fundamental role in determining the evolution of the growth to form a continuous film[22]. On the other hand, strongly enhanced magnetic moments have been predicted for 3d transition metals in reduced dimensionality on non-magnetic noble metal substrate by theoretical work[23]. Therefore a large number of experimental investigations of their growth on the Au(111) surface have been carried out so far.
Iron is a 3d transition metal present in three allotropic forms (fig.4.4)that condensate in solid state in three different structures: α-iron and δ-iron present bcc structure, while γ-iron is fcc. The growth of Fe on Au(111) has been previously investigated using TEM[24], STM[25] and various diffraction techniques[26, 27,

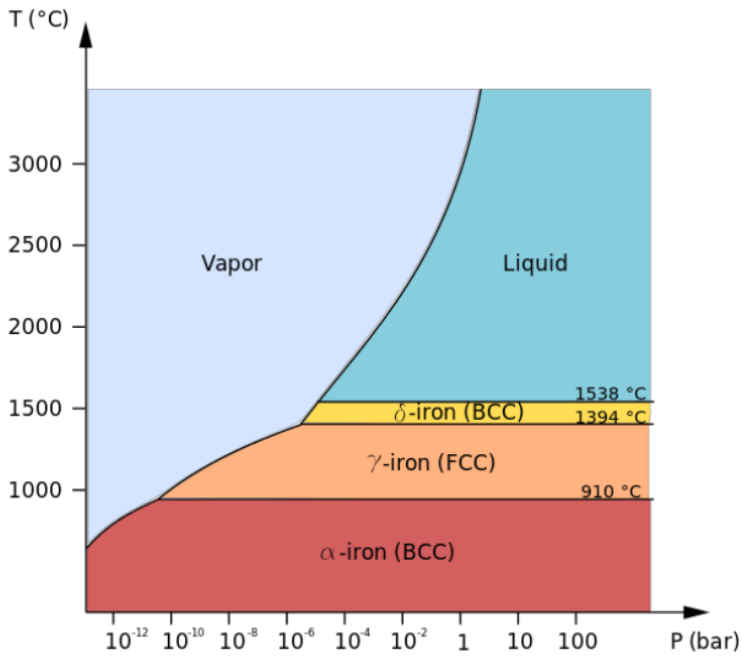

Figure 4.4: *Phase diagram of pure iron showing the allotropic forms: α and δ-iron condensate in body centered cubic (bcc) structure, while γ-iron is face centered cubic (fcc). T=300K and P=1×10^{-9}mbar lead to allotropic α-phase of the diagram*

28]. These studies found that Fe grows pseudomorphic on Au(111) forming a fcc phase, which is metastable at room temperature and expanded 12% compared to the high temperature fcc γ-Fe phase[25]. A transition from fcc to bcc structure occurs after a few layers have grown, when the film is no longer able to accommodate the substrate induced strain[27].

In our experiments iron was evaporated in situ keeping always the substrate at room temperature. The deposition rates were kept constant monitoring the emission current which is related to the flux of evaporated atoms. During the evaporation the pressure in the chamber was $\sim 10^{-9}$ mbar. The images here reported were obtained in the constant current mode with tunneling current of 0.1-1.0 nA and negative bias voltages ranging from 0.5 to 1.5 V. The deposition rates were calculated from statistical analysis on STM images in which only clearly separated islands were distinguishable.

4.2.1 Thermodynamic and kinetic effects

We start our investigation using a relative low deposition rate of about 0.02 ML/min. Figure 4.5a shows the result of deposition of 0.1 ML of iron into Au(111) surface. The islands of Fe are a single monolayer high with Fe-Au step height of 2.4±0.5$\mathring{A}$, while the Au-Au step height is found to be 2.6±0.5$\mathring{A}$ (values obtained in the voltage range used). Fe islands are observed to nucleate mainly at the corners of the Au(111) herringbone reconstruction. This preferential nucleation at elbows has been observed for other metals like Co[29], Ni[30], Pd[31], Pt[32]. The most accredited mechanism to explain this behaviour are understood in terms of a two-step process. In the first step, mobile adatoms displace Au atoms in the substrate via a place exchange process. In the second step, the substitutional adatoms act as a preferential nucleation sites, trapping the diffusing adatoms with high efficiency. In other words, the reason why some elements preferentially nucleate at the elbows of Au(111) does not depend on which is trapped most effectively at these specific sites, but rather which will undergo place exchange most easily and subsequently act as a nucleation site[33]. In fact for other metals such as Al[34], Ag[35] and Au[36], preferential nucleation was not observed. Since place exchange increases the coordination of the deposited atoms at the expense of the substrate atoms, the question of whether place ex-

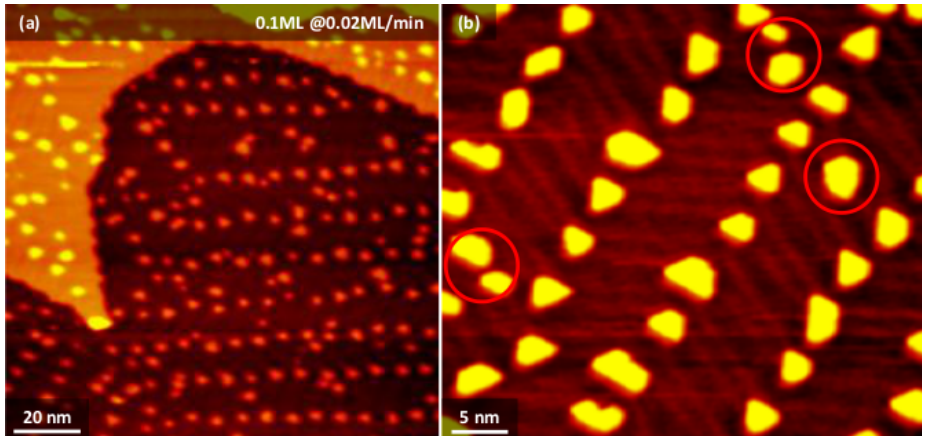

Figure 4.5: *θ_{FE}=0.1 ML of iron onto Au(111) with deposition rate=0.02ML/min. (a)large STM image area, nucleation occurs firstly at the elbows of the herringbone reconstruction. (b) Once the elbows are all occupied, nucleation out of elbows positions starts, as indicated by red circles.*

change is energetically favourable can be approached, in a first approximation, by comparing surface free energies and heats of sublimation of the substrate with those of the various admetals as a measure of the metal-metal bond strength. It was shown that the elements which have been observed to display preferential island formation at elbows of the Au(111) reconstruction have higher value of surface free energy and heat of sublimation than Au. Those which were not found to form islands preferentially at the elbows all have lower values of these two quantities[37]. Once all the corners of the herringbone reconstruction are occupied, new islands out of elbow positions start to appear (red circles in the inset of fig.4.5b), indicating that the nucleation at the elbows does not represent the only possibility for Fe to nucleate although was energetically favorable.
Increasing the coverage of iron up to 0.5 ML, where the portions of bare gold are well visible, it is observed a substantial modification of the gold herringbone reconstruction pattern, as shown in fig.4.6a-b upon the deposition of 0.3 and 0.4 ML respectively. This effect indicates strong interaction between the growing islands and the topmost Au(111) layer, as in the case of Pt[32] and Pd[4], where, crossing a threshold coverage located around 0.25ML, when the nucleation starts to occur at random positions outside the elbows, the reconstruction

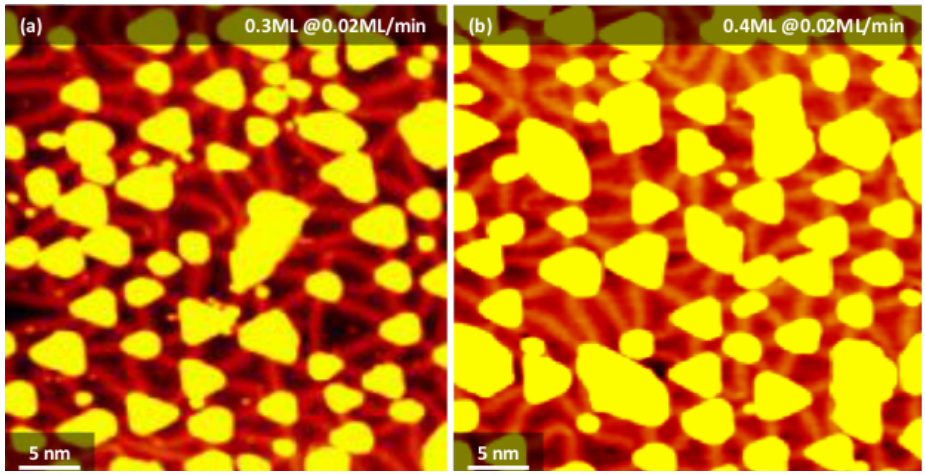

Figure 4.6: *(a)θ_{FE}=0.5 ML of iron onto Au(111) with deposition rate=0.02ML/min. Islands of second layer represented by the brightest area of the image start to appear. (b)θ_{FE}=0.3 ML, reconstruction pattern results very affected by the modification induced by the growing islands of iron.*

is literally "pushed away" by islands entirely lying on fcc or hcp domains. This common behaviour is probably due to the fact that the crossing of a ridge is expected to be energetically very unfavorable for islands, due to the change of lattice parameters and to the establishment of internal fcc/hcp mismatch.
When the coverage exceeds 0.5 ML, Fe islands grow laterally in size and coalesce leading to a quasi layer-by-layer growth, however a small but non-negligible fraction of Fe has begun to grow also in the second layer as shown in fig.4.7a. In fact the islands of second layer, represented by the brightest area in the STM images, are still limited in number and size, while almost the first layer is entirely covered, leaving a small fraction of the gold surface still visible. The dislocation lines appear on top of the islands, as indicated by blue arrows in fig.4.7b, and continue on the surface. This kind of behaviour is characteristic of a perturbed Au(111) clean surface in presence of defects that introduce strain at the point where they appear at the surface[38]. In other words, the characteristic reconstruction of the Au(111) surface undergoes to perturbation upon the insertion of Fe atoms in gold surface.
In order to obtain quantitative information about coalescence and random nucleation of islands, we performed a statistical analysis of islands in first layer of

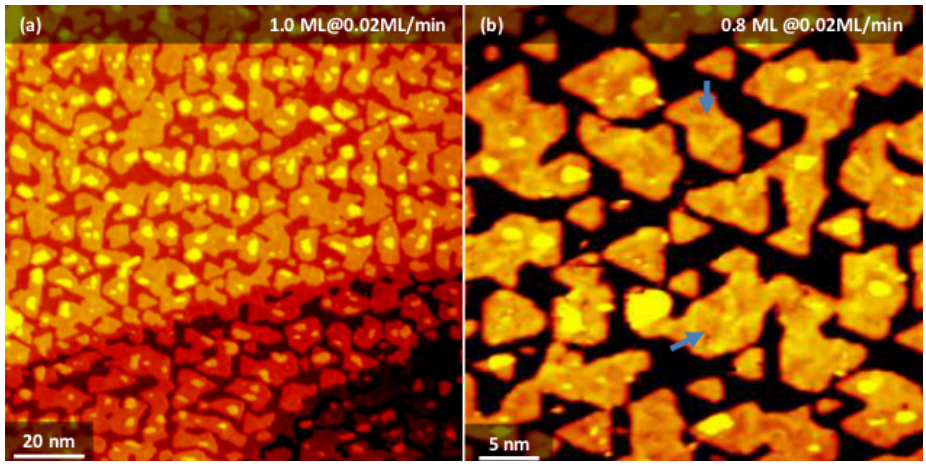

Figure 4.7: *(a)θ_{FE}=0.5 ML of iron onto Au(111) with deposition rate=0.02ML/min. Islands of second layer represented by the brightest area of the image start to appear. (b)θ_{FE}=0.3 ML, reconstruction pattern results very affected by the modification induced by the growing islands of iron.*

the STM images obtained at different Fe coverages. In fig.4.8a it is shown the number of islands per unit surface, in other words the density of islands (N), as function of coverage. Below 0.3ML we can identify a region (region I) where the density of islands increases with the coverage, while after that value it reaches a plateau (region II), and at approximatively 0.4-0.5ML it starts to decrease (region III), in agreement with the behaviour well described by the so called Deposition-Diffusion-Aggregation model[39]. . The islands density evolves with coverage as a result of two processes: the nucleation of new islands and the coalescence among them. In region I, the growth is dominated by the nucleation of new islands, while in region III the main mechanism is now the coalescence of the islands. In region II the two mechanisms take both place at similar rates. Since coalescence is a direct consequence of the increasing of islands size, fig4.8b shows the evolution of average island size (S) in first layer versus total coverage. The three regions are characterized by different growth regimes characterized by a linear increase of the average area with respect to the first layer coverage. The slopes for region I and II result equal, leading to a growth regime where Fe islands both increase their number and size at the same time. When coalescence among islands becomes the main mechanism for Fe growth, the island density starts to decrease while, on the other hand, the average island size increases.
As previously mentioned, the heteroepitaxial growth depends on both thermodynamic and kinetic effects. Therefore we tried to observe how the growth of Fe on Au(111) could be affected by changing the deposition rate, and so

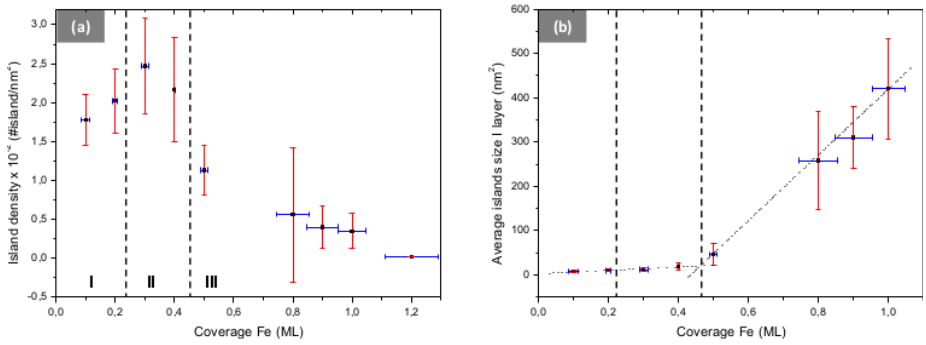

Figure 4.8: *(a)Surface density of islands as a function of the Fe coverage. Dotted lines separates the different regimes of growth(b) Average area of the Fe islands plotted as a function of the Fe coverage. Bars indicate the error of the measured parameters for each acquisition*

the dependence on kinetic of the growth due to a no-zero value of ES barrier. Four different covareges are shown in fig.4.9 with a deposition rate of about 0.2ML/min. Once again for low coverages up to 0.2 ML, the growth proceeds as in the previous study case, that is nucleation mainly at the elbows of the Au(111) herringbone reconstruction, followed by nucleation in out of elbows positions (see fig.4.9a and inset).
The herringbone reconstruction remains unaltered even when the coverage exceeds 0.2 ML, as shown in fig.4.9b-c for 0.4 and 0.6 ML respectively. As a consequence, islands grow in size and start coalescing along the $[11\bar{2}]$ directions, where the distance between two consecutive elbows is shortest (7.3 nm), leading to the formation of 1D structure (nano-stripes). Only when the coverage reaches values of $\sim$ 1.0 ML (fig.4.9d), the coalescence starts also along the $[1\bar{1}0]$, where typically distance is about 15 nm. In the islands of first layer, no evidence of dislocation lines were detected after the analysis of tens of STM images. The appearance of Fe islands in second layer is estimated to begin occurring, as in the previous case, at $\sim$0.5 ML.

Further increasing of the deposition rate leads to a situation shown in figure 4.10, where four coverages are shown, obtained with a deposition rate of $\sim$1.5 ML/min. No significative changes are observed with respect to fig.4.9, with the characteristic nucleation at the elbows of the herringbone reconstruction and no distortion of the latter from 0.3 ML (fig.4.10a); the appearance of islands of second layer around 0.5 ML (fig.4.10b) and consequently coalescence firstly along the $[11\bar{2}]$ and then along $[1\bar{1}0]$ directions (fig.4.10c), as consequence of the growth on unmodified gold pattern represented by the undistorted herringbone reconstruction. Figure4.10d shows the morphology of a sample covered by 3.0 ML. The first layer is totally fulfilled, while the second has begun to coalesce along the directions od symmetry. About third layer islands, it is possible observe that the islands follows the same growth scheme as the previous layers, since, at this coverage, the growth is still pseudomorphic with Au(111) surface.

Therefore, as it is reasonable to expect, the deposition rate affects the growth of Fe on Au(111) surface. The most significative change is represented by the modification of the herringbone reconstruction observed at low deposition rate of 0.02 ML/min (see fig.4.6a-b), as in the case of other elements, i.e. Pd and Pt. In previous studies of growth of Fe on Au(111), such behaviour never has not been observed [25, 40, 41, 42]. It has to be noted that the effect of modification of herringbone reconstruction disappears once the deposition rate become higher, suggesting a correlation with the growth kinetics. In fact, in the experiments cited above, the deposition rate used was of the order of 0.1ML/min. As previously discussed, the crossing of a ridge is expected to be energetically

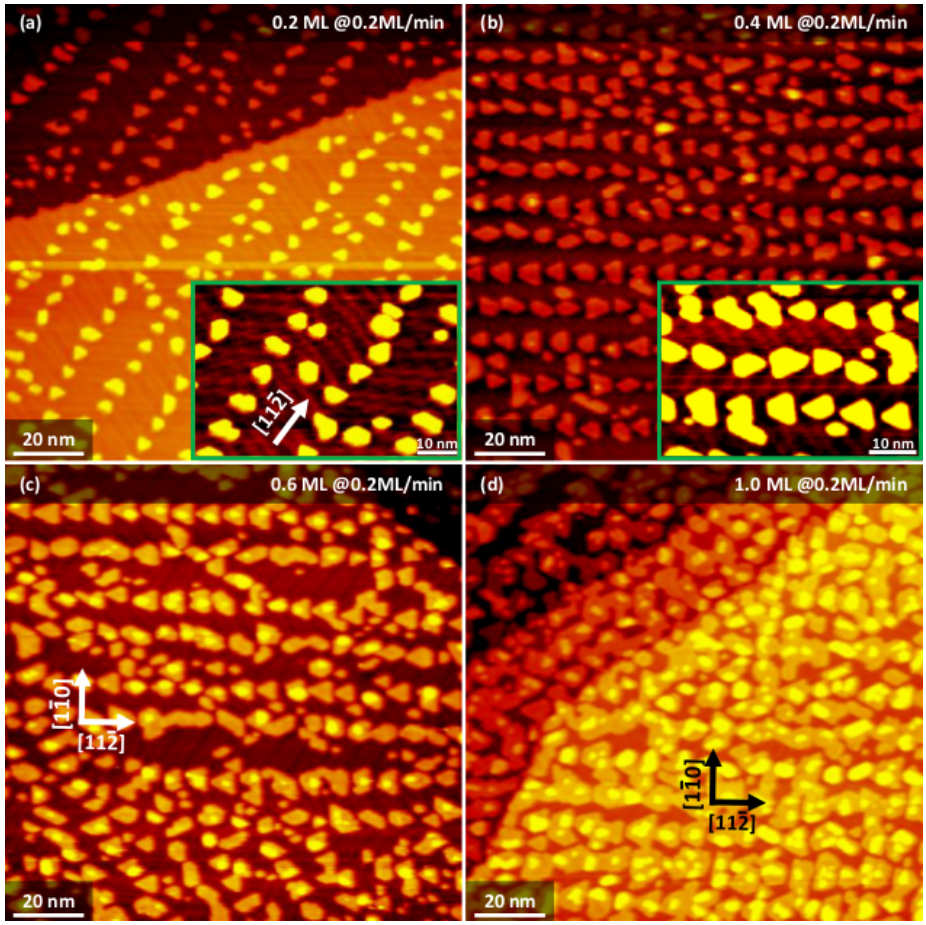

Figure 4.9: *STM images acquired after successive deposition of iron onto Au(111) with deposition rate=0.2ML/min. (a)*$\theta_{FE} = 0.2$ *ML, nucleation still occurs mainly at the elbows of the Au(111) herringbone reconstruction, followed by nucleation in out of elbows positions; (b)*$\theta_{FE} = 0.4$ *ML, islands become bigger in size but no modification of the underlying herringbone reconstruction is observed; (c)* $\theta_{FE} = 0.6$ *ML, as consequence of undistorted gold reconstruction, Fe islands start firstly to coalescence along the* $[11\bar{2}]$*, also the formation of islands in second layer is clearly visible; (d)* $\theta_{FE} = 1.0$ *ML, the coalescence starts also along the* $[1\bar{1}0]$.

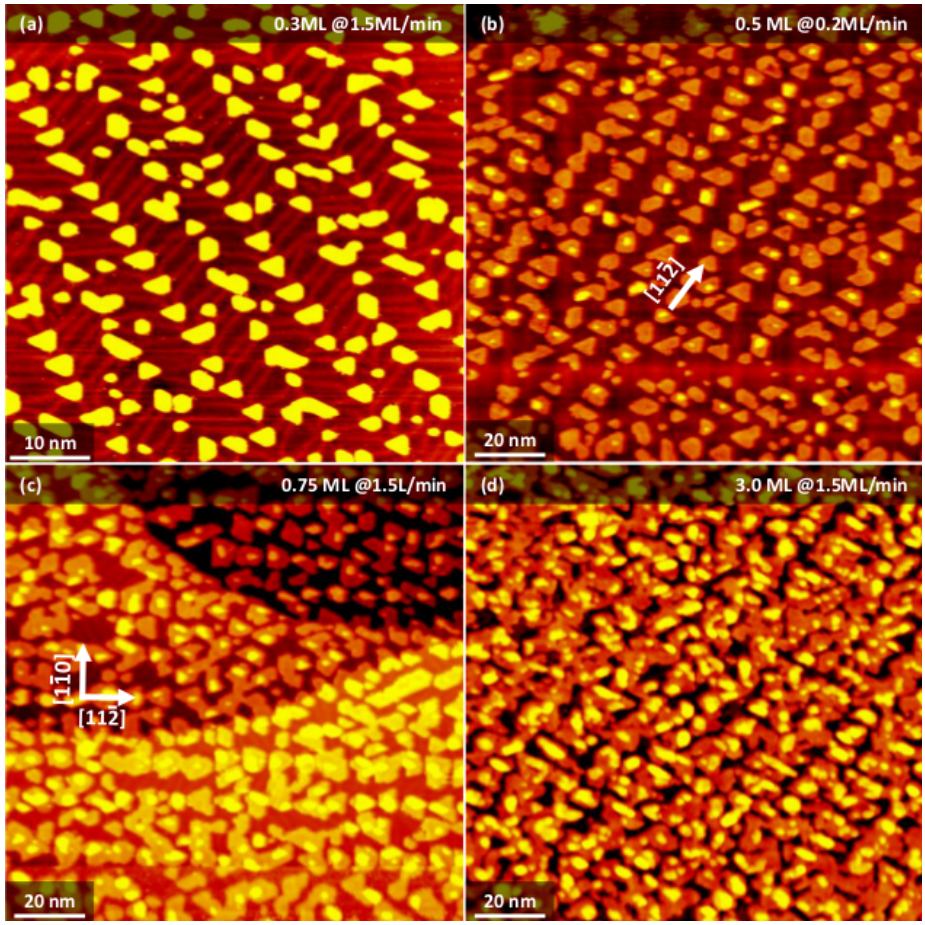

Figure 4.10: *STM images acquired after successive deposition of iron onto Au(111) with deposition rate=1.5ML/min. (a)θ_{FE} = 0.3 ML, nucleation still occurs mainly at the elbows of the Au(111) herringbone reconstruction, followed by nucleation in out of elbows positions. No appreciable modification of the underlying herringbone reconstruction is observed; (b)θ_{FE} = 0.5 ML, islands become bigger in size and also the formation of islands in second layer is clearly visible; (c) θ_{FE} = 0.75 ML, the coalescence of Fe islands along the* $[11\bar{2}]$ *and* $[1\bar{1}0]$ *is observed; (d) high coverage sample with θ_{FE} = 3.0 ML*

very unfavorable for islands, due to the change of lattice parameters and to the establishment of internal fcc/hcp mismatch. This mechanism is common to Pd and Pt and these experimental results suggest the idea that the mechanism can be generally valid for all the class of elements that show preferential nucleation at the elbows of herringbone reconstruction of the Au(111) surface only if the deposition rate is rather low, that permits a longer interaction between metallic adatoms and the surface.
Also the morphology of the films results affected by the deposition rate. Intuitively when the flux is higher, more Fe atoms reaches the surface for unit of time. Some of them will land on top of the island already formed, the second layer, but if the flux is rather low and they posses enough kinetic energy, they have time to cross the ES barrier coming down to first layer. If the flux is higher, the atoms landing in second layer in their diffusing movements can encounter other Fe atoms of second layer before to cross the ES barrier. If they form a stable cluster they start to behave as a new nucleation center and islands of second layer start to appear. The statistical analysis for different coverage at different rates confirms what it is expected: the higher the flux the higher the percentage of islands in second layer at equal amount of deposited Fe. Islands in second layer are also more numerous (higher value of N) and bigger (higher value of S). At the same time, opposite behaviour for islands in first layer is observed: higher the flux, lower the value of the parameters that characterize the growth in first layer.

4.2.2 Structural phase transition

The STM image upon the deposition of 6 ML Fe is shown in fig.4.11. A clear change in topography appears: together with the triangular shaped islands, some rectangular-shaped structures, also referred as crystallites, appear. As previously described, Fe starts to grow pseudomorphically on Au(111) but the fcc structure is a metastable phase for Fe at RT whose native structure is bcc. In fig.4.11 b the Au(111) hexagonal and the Fe(110) rectangular unit cell are shown. The Fe(110) lattice fits onto the Au(111) surface with a minimum of distortion when the $\langle 1\bar{1}0\rangle_{fcc}$ direction is parallel to the $\langle 001\rangle_{bcc}$ direction. For this orientation, the mismatch along $\langle 001\rangle_{bcc}$ is only 0.5% while along the $\langle \bar{1}10\rangle_{bcc}$ the Fe(110) lattice is contracted by 19% with respect to $\langle 11\bar{2}\rangle_{fcc}$ of underneath Au(111) lattice[43]. The stress resulting from the mismatch between the pseudomorphic fcc Fe on Au(111) and the stable bcc(110) phase can only be accumulated for a few atomic layers. Consequently, the pseudomorphic fcc(111) Fe film can only be maintained for few layers. This is the driving force for

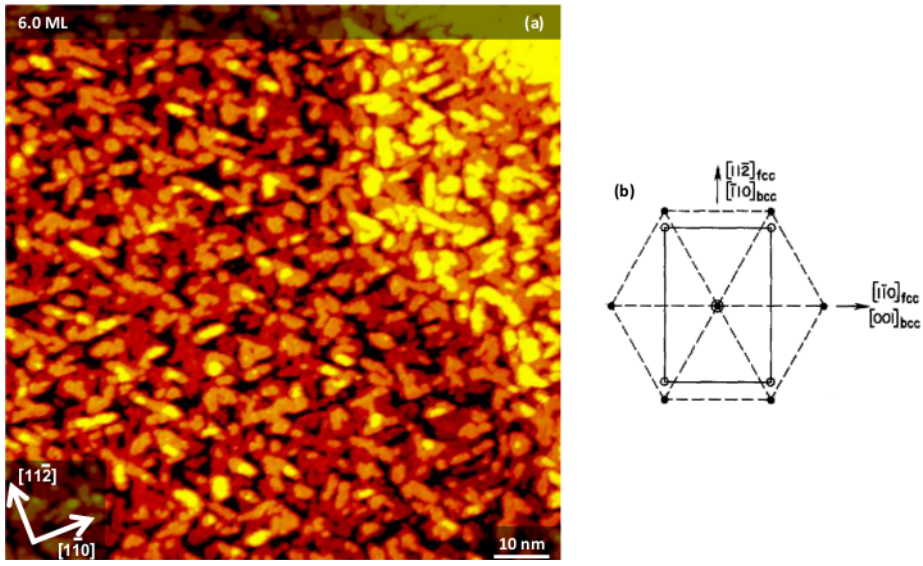

Figure 4.11: *(a)STM image of 6.0 ML of Fe/Au(111)* $(100 \times 100)nm^2$. *Fe crystallites appear as elongated islands along the* $\langle 1\bar{1}0 \rangle_{fcc}$ *directions. This indicate that a transition from coherent growth to bcc crystal structure occurred. (b)The Au(111) (black dots) and Fe(110) (white dots) unit cells showing the 19% contraction of the Fe(110) surface unit cell along the* $[\bar{1}10]$ *compared to the substrate[43].*

the phase transition from fcc(111) to bcc(110)[42]. Therefore the growth is not pseudomorphic any more and the described rectangular-shaped crystallites represent the relaxed bcc Fe crystal structure with (110) surface orientation.

4.2.3 Effect of annealing

In this section we will discuss the effects of increasing the kinetic energy in the morphology evolution of Fe films grown on Au(111) surface. The annealing experiments were conducted raising the temperature at the desired value and then kept constant for fifteen minutes. The results are shown in the collections of STM images of fig.4.12 and 4.13 for 0.5 ML and 1.0 ML of Fe respectively. For both coverages same trend appears: increasing the temperature of annealing, islands in first layer start to coalesce with no preferential direction and become bigger in size, leading to the disappearance of smaller islands. The results of the statistical analysis on the STM images, relatively to the first layer,

show that increasing the temperature of annealing (T), the average area of the islands (S) increases and, at the same time, the density of islands (N) decreases. The coverage in second layer tends to zero, as well S and N, at 100°C and 125°C for 0.5 ML and 1.0 ML. The disappearance of islands in second layer is ascribable to the increase kinetic energy of Fe atoms. In fact raising the annealing temperature, the atoms of the islands in second layer posses enough energy to break Fe-Fe stable bonds and to cross ES barrier "falling down" in first layer where they are incorporated in the islands.
The effect of the incorporation of the dislocation lines into the islands becomes visible, even after light annealing. In fact, for both coverage is possible to note the corrugation imposed by the reconstruction of Au(111) surface on top of the islands. It seems that the dislocation lines do not feel the presence of the islands since any apparent lateral displacements or changes in direction at the step edges are observed. Also the apparent height is different from that measured with no annealing. The new measured height is found to be $2.6\mathring{A}\pm0.3\mathring{A}$ in agreement with that measured for clean Au(111) at step edges. This reinforce the hypothesis of intermixing between Fe and Au atoms inside the islands and the surface layer, previously discussed for low rate of deposition. The increasing of annealing temperature, and so of the kinetic energy of the atoms, favours this behaviour. But this process does not seem to be the only one occurring. In fact, together with the progressive disappearance of islands in second layer, also the islands in first layer seems to disappear in such a way that is impossible to distinguish univocally the islands. The inability to distinguish Fe islands from Au(111) surface is observed at 125°C and 150°C for 0.5 ML and 1.0 ML respectively. Moreover, the herringbone reconstruction at these higher annealing temperatures tends to appear more like the regular reconstruction of clean Au(111), especially for STM images of fig.4.12 where the total amount of deposited Fe is lower. As previously mentioned, the distortion of the herringbone reconstruction is due to the presence of defects that introduce strain at the point where they appear at the surface. The reappearance of the "regular" Au(111) reconstruction is interpreted as the disappearance of these defects (iron atoms or islands) from the surface. This leads to the conclusion that a fraction of the iron has already disappeared from the topmost layer. This behaviour suggests that the intermixing of Fe and Au is a process that does not stop at the interface but continues in bulk. In other words, in the first steps of annealing experiments we observe an intermixing of Fe-Au at the surface leading to the formation of mixed Fe-Au islands, or surface alloy, while at higher temperature is observed that the Fe atoms have enough energy to cross the barrier of diffusion into the bulk of Au.

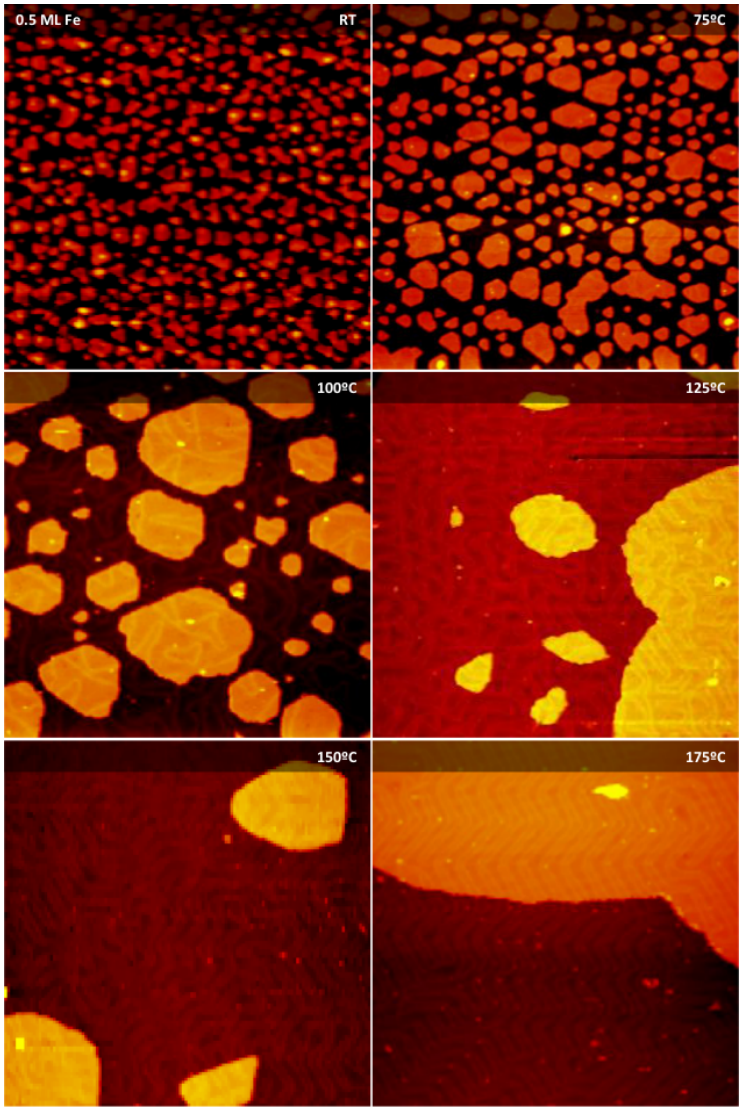

Figure 4.12: *0.5ML Fe on Au(111) and subsequent annealing experiments.*

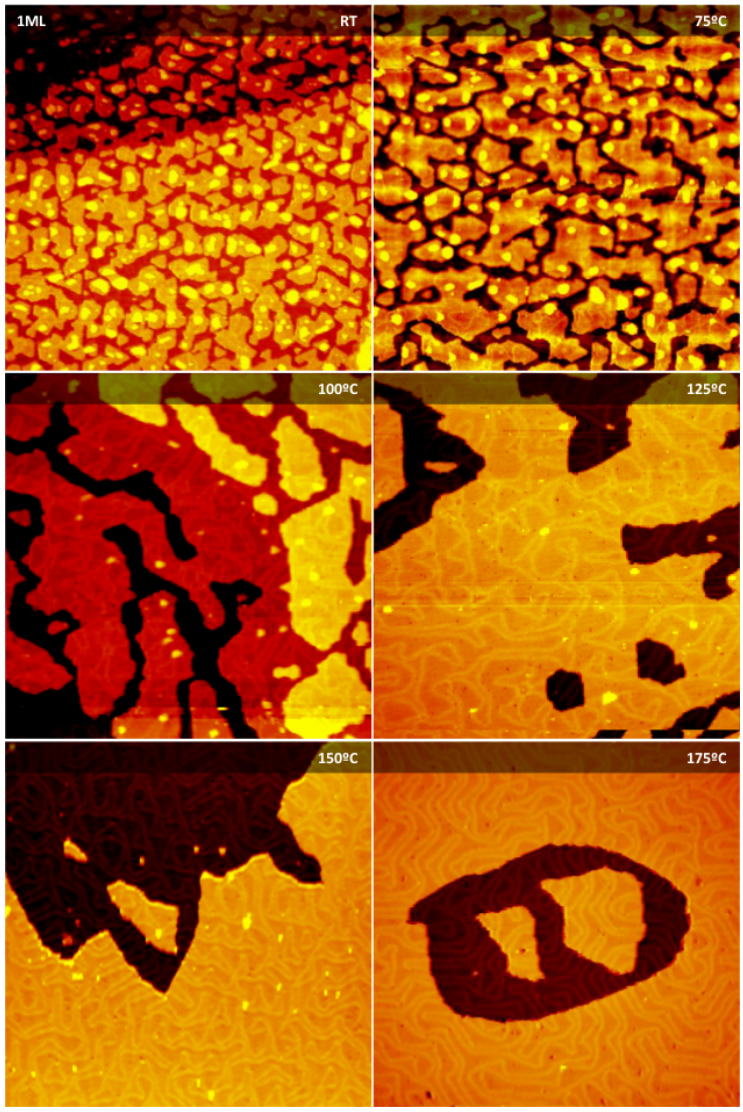

Figure 4.13: *1.0 ML Fe on Au(111) and subsequent annealing experiments.*

To have a more complete idea and to validate the hypothesis deduced so far, we performed XPS measurements on the system at the distinct annealing temperatures. The XPS spectra of 1.0 ML of Fe deposited at RT undergone to successive annealing experiments are shown in fig.4.14. It is important to keep in mind that, although XPS is a surface technique, X-rays have a certain penetration length, therefore the XPS signal of Fe_{2p} arises both from surface and from the first inner layer, estimated to be 3-5 layer at the energy we are measuring (1486.74 eV, see chapter 2). In order to simplify the following discussion, we will use only the expression "on surface" keeping in mind also the contri-

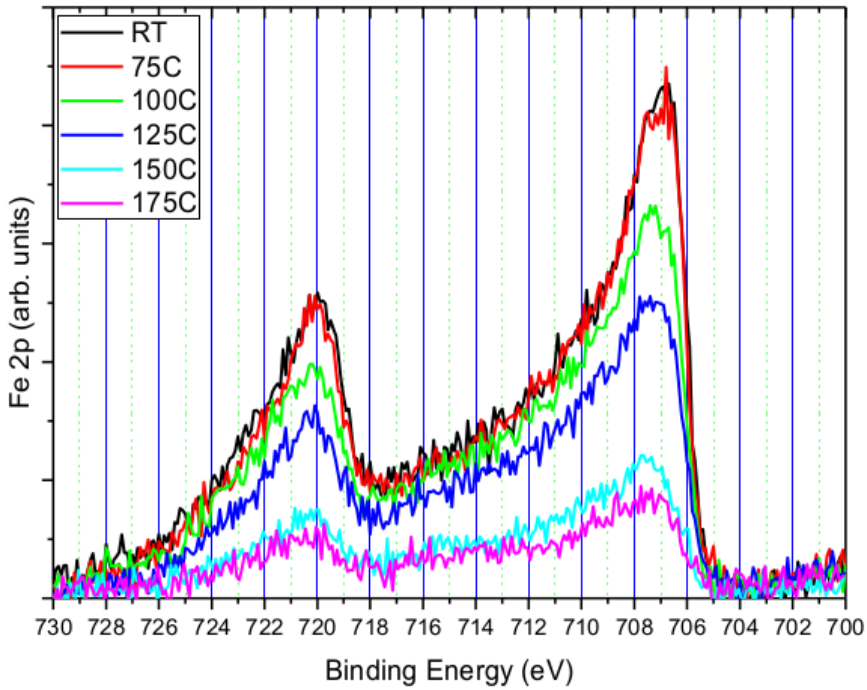

Figure 4.14: *XPS signal of Fe_{2p} 1.0 ML Fe on Au(111) deposited at RT temperature and successive annealing experiments. The area subtended by each spectra decreases progressively as the annealing temperature increases, indicating a diffusion into bulk combined with change in the morphology of the surface. The metallic character of Fe is conserved through the whole annealing experiments, as confirmed by the position of the peak of $Fe_{2p_{3/2}}$ located at 707.0 eV and separation energy between the doublet of Δ=13.10 eV.*

bution of the inner layer. The signals arising from 2p level of Fe maintain the characteristic metallic shape with the peak of $Fe_{2p_{3/2}}$ located at 707.0 eV and separation energy between the doublet of Δ=13.10 eV[44] during the annealing experiments, although a very small shift of 0.5 eV is measured for the spectra after 150 and 175°C (cyan and pink spectra respectively in fig.4.14) towards higher binding energy. The Fe_{2p} progressively shows lower slopes as the annealing temperature increases. Moreover, the area of the Fe XPS peak diminishes as consequence of the increasing of annealing temperature. This indicates that the deposited amount of Fe at room temperature on Au(111) surface (black spectrum) progressively disappears from the surface for effect of higher annealing. Normalizing to the area of the sample as soon as Fe is deposited (RT) the area of Fe_{2p} spectra after the annealing cycles, it is possible to give an estimation of the percentage of Fe diffusing into bulk as shown in table 4.1. Nevertheless the STM images of fig.4.13 reveals morphological differences from the sample at room temperature and consequently to the annealing processes. Therefore, from the combined measurements of STM and XPS, it appears plausible the idea of the mixed Fe-Au bimetallic surface[45], that might show different structural, electronic, chemical and catalytic properties.

4.3 Growth of Fe on Au(111) precovered with TCNQ monolayer

The molecule used as modifier for Fe growth is the acceptor molecule TCNQ. As previously discussed, a monolayer of TCNQ physisorbs on the clean Au(111) substrate and upon evaporation of Fe, one metal atom can coordinate to four nitrogen atoms leading to the formation of an extended MOCN. The coordination between Fe atoms and cyano groups occurs with a yield close to 100%. The completed monolayer coordination is experimetally observed at a coverage of θ_{Fe}=0.18±0.05ML, which is the stoichiometric amount needed to coordinate a complete monolayer of TCNQ on Au(111). The coordination process consists of mainly three steps: (1)the statistical impinging of iron atoms onto the surface, (2)the diffusion of the iron atoms and (3)morphological and electronic rearrangement of TCNQ (see chapter 3). No nucleation of Fe islands could be observed up to θ_{Fe}=0.18ML due to the fact that all metal atoms are "consumed" by the organic monolayer in the described coordination reaction. When the amount of deposited Fe surpasses 0.18 ML, an excess of Fe is present on the substrate.
STM images of θ_{Fe}=0.5ML (deposition rate=0.02ML/min) onto Au(111) pre-

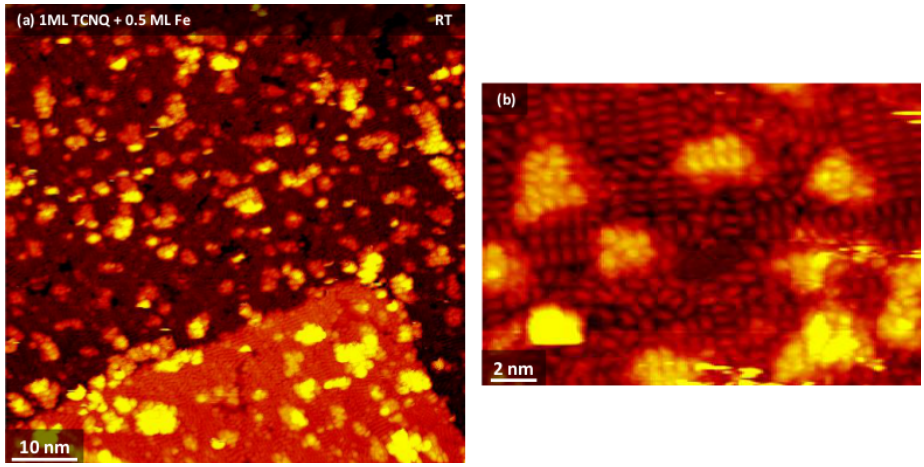

Figure 4.15: *(a) 0.5 ML of Fe deposited (deposition rate=0.02ML/min) on Au(111) precovered with TCNQ monolayer (I_t=-0.66 nA, V_t=-2219 mV); (b) Detail of the sample: brighter islands with TCNQ molecules floating on top, order imposed by the coordination of Fe and TCNQ appears perturbed due to the excess of Fe I_t=-1.02 nA, V_t=-1440 mV*

covered with a complete TCNQ monolayer are shown in fig.4.15. It is easy to distinguish a large number of islands that appear brighter, exhibiting an increased apparent height, which is measured to be 0.3 nm. Also, on these islands TCNQ molecules are still resolved seemingly "floating" on top (fig.4.15b). The rectangular arrangement imposed by the coordination between cyano groups and individual Fe atoms is only locally conserved (cf. chapter 3), which is a clear evidence that there is an excess of Fe atoms present on the surface. Therefore it is reasonable suppose the formation of flat Fe layer underneath the TCNQ molecules. The shape of these Fe islands do not appear clearly triangular or hexagonal as in the case of Fe on Au(111). Since these peculiar shapes are an evidence of pseudomorphic growth with fcc(111) underlying surface[9], it is possible that the pseudomorphic growth of Fe is hindered by TCNQ monolayer, even though more experimental observations are needed. No preferential growth of Fe islands at elbows is observed for Fe deposition onto Au(111) surface precovered with TCNQ monolayer. Neither the herringbone reconstruction appears visible as in the case of disordered area of MOCN (see chapter 3).
The statistical analysis over STM images of this sample reveals that 30% of the surface is covered by these islands with TCNQ floating on top. Also the average area of the islands (S) is estimated top be 8nm^2 while the density of the islands is 2.97$\times$10$^-$2[# islands/nm^2]. This values have to be compared with those referred to a deposition of 0.3ML Fe. This because, as previously discussed, $\sim$0.2ML are consumed in coordination bonds with TCNQ. The comparison between 0.3 ML Fe on Au(111) and 0.5 ML Fe on TCNQ/Au(111), shows that the islands cover an area compatible with our assumption: 28.83% for Fe/Au(111) vs 30% for Fe/TCNQ/Au(111). The density of islands results higher the latter systems (2.97 vs 2.47$\times$10$^-$2[# islands/nm^2]) while, on the other hand, the average area of the islands is bigger for Fe on clean gold(8 vs 12 nm^2).
Looking at experimental evidences, the model we propose looks at the cyano groups as diffusion traps for iron atoms more efficient than the elbows of the herringbone reconstruction. When the coverage of Fe exceeds 0.18 ML, that represents the stoichiometric amount of Fe to coordinate a complete monolayer of TCNQ on Au(111), Fe atoms start to nucleate around one of the equivalent Fe center involved in the coordination. Therefore the free diffusion length of the impinging iron atoms is now reduced with respect to the clean Au(111) surface, where it was limited by the distance between two elbows of the reconstruction. A reduced mobility of the deposited material lead to smaller islands with higher surface density, which is in line with the observations seen so far. The lack of preferential nucleation sites in the early stages of the growth leads to anisotropic growth of Fe on Au(111) precovered with TCNQ monolayer.

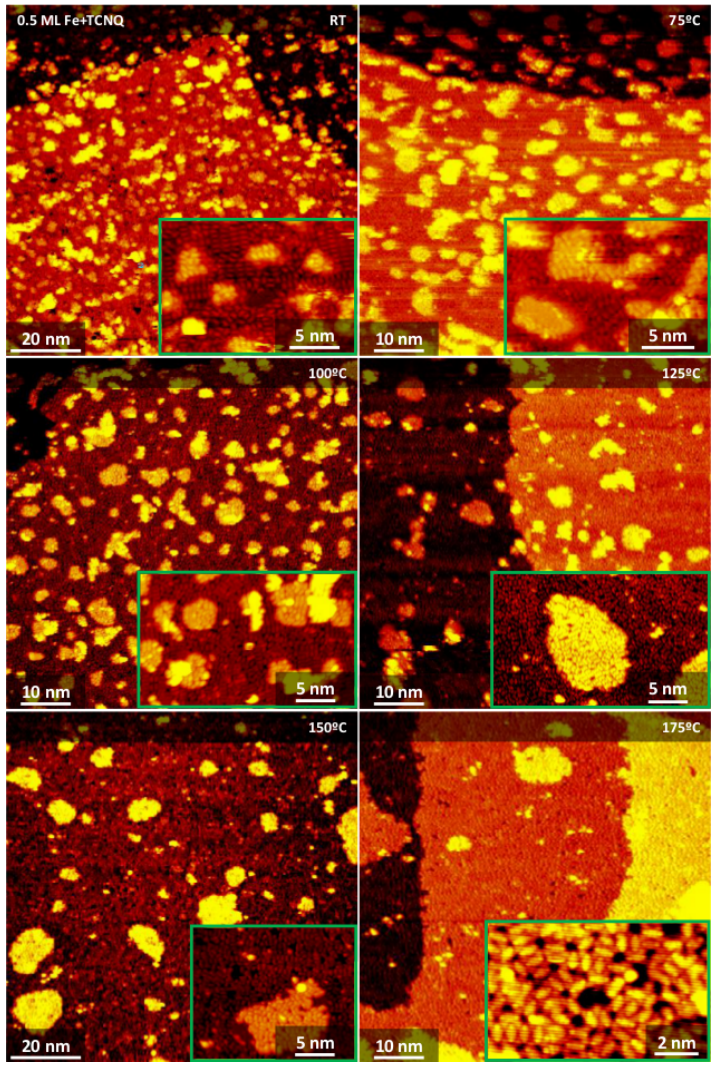

Figure 4.16: *Evolution of morphology in function of annealing temperature of 0.5 ML Fe onto a complete monolayer of TCNQ/Au(111) (RT I_t=-0.66 nA, V_t=-2219 mV; 75 °C I_t=-1.02 nA, V_t=-1440 mV; 75 °C I_t=-1.02 nA, V_t=-1440 mV; 75 °C I_t=-1.02 nA, V_t=-1440 mV; 75 °C I_t=-1.02 nA, V_t=-1440 mV; 75 °C I_t=-1.02 nA, V_t=-1440 mV*

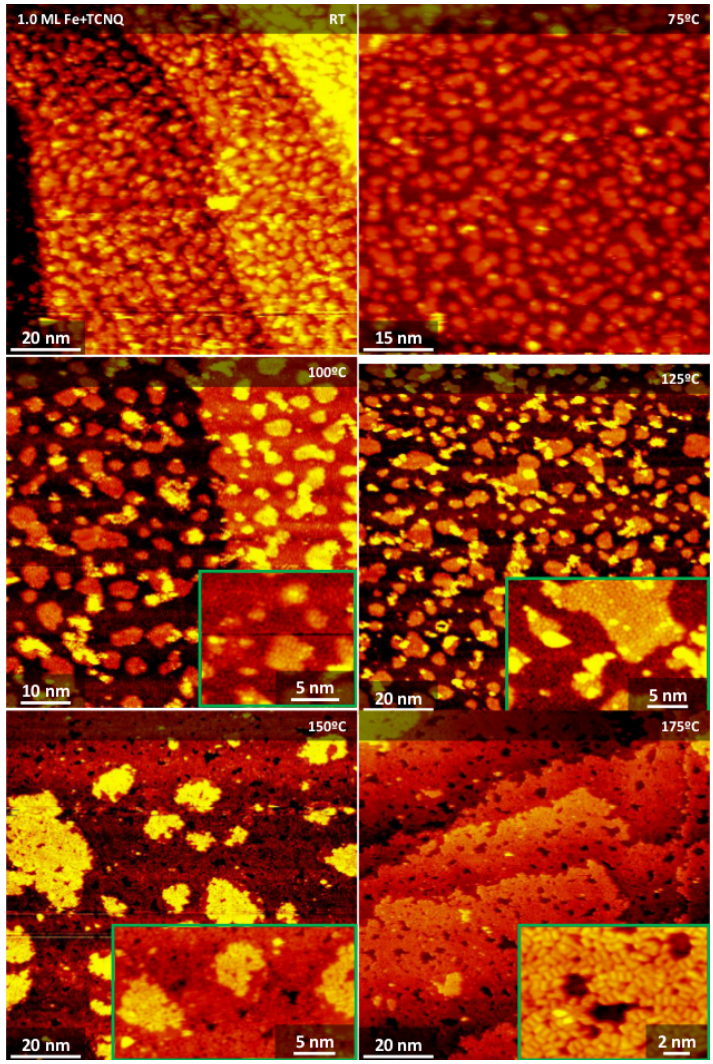

Figure 4.17: *(a) Evolution of morphology in function of annealing temperature of 1.0 ML Fe onto a complete monolayer of TCNQ/Au(111) (RT I_t=-0.66 nA, V_t=-2219 mV; 75 °C I_t=-1.02 nA, V_t=-1440 mV; 75 °C I_t=-1.02 nA, V_t=-1440 mV; 75 °C I_t=-1.02 nA, V_t=-1440 mV; 75 °C I_t=-1.02 nA, V_t=-1440 mV; 75 °C I_t=-1.02 nA, V_t=-1440 mV*

In order to compare also the evolution of the morphology as a function of annealing temperatures, we performed the same annealing experiments as in the case of Fe on clean gold. The STM images of fig.4.16 and 4.17 show the results of the annealing for 0.5 ML and 1.0 ML of Fe respectively on precovered TCNQ/Au(111) layer and subsequent annealing experiments. Increasing the temperature of annealing, islands start to coalesce again with no preferential direction and become bigger in size as in the case of Fe/Au(111). The most important common feature for both coverages is that well defined islands are still visible on the surface, even at the annealing temperatures that, in previous case, lead us unable to distinguish Fe island from modified Au(111) surface. In fact, for both coverages it is possible to note that islands of Fe with TCNQ on top are resolved on the up to 150 °C and also the TCNQ do not undergo to thermal degradation up to 175 °C. The results of the statistical analysis of the islands in first layer for 0.5 ML for 0.5 ML of Fe on TCNQ/Au(111) in function of annealing experiments are summarized in the table 4.1, where are reported together for 0.5 ML of Fe on Au(111). As expected, the values of density of islands (N) remain relatively high even at higher temperatures and the average area (S) does not shown dramatic changes upon annealing. A situation different from Fe /Au(111) where the islands become bigger and less numerous as function of annealing temperature up to intermix with the surface. In this case increasing the kinetic energy of Fe atoms, the presence of TCNQ makes less efficient the coalescence between islands, leading more numerous but smaller islands on the surface. Therefore the mobility intra-layer of Fe atoms is reduced by the presence of TCNQ molecules which lower the diffusivity of Fe

	0.5 ML Fe/TCNQ/Au(111)			**0.5 ML Fe/Au(111)**		
Temp. °C	I layer [%]	S [nm^2]	N 10^2[#/nm^2]	I layer [%]	S [nm^2]	N 10^2[#/nm^2]
RT	30	8	2.97	49.1	47	1.13
75	29.2	14	1.82	50.35	50	0.98
100	27	16	1.81	40.38	130	0.31
125	15.9	14	1.2	–	–	–
150	10.55	13	0.97	–	–	–
175	Unable to distinguish Fe islands from Au(111) surface.					

Table 4.1: Statistical analysis of islands in first layer for 0.5 ML of Fe on TCNQ/Au(111) and on Au(111)as a function of the temperature of annealing.

atoms.

To have a more detailed scenario of the effect of the presence of TCNQ in the growth of Fe, we performed XPS measurements. The N1s spectra at different annealing temperature for 1.0ML deposited at RT on Au(111) precovered with TCNQ monolayer are shown in fig.4.18. The shape of the peak of N_{1s} does not change during the annealing processes and it can be deconvoluted with only a peak, reflecting an unique chemical environment for nitrogen of TCNQ molecules. Neither the position of the peak change which results centered at 398.4 eV. This value for N_{1s} is the same found for MOCN system (see chapter 3). Therefore also in presence of an excess of Fe, the TCNQ molecules are able, through the cyano groups, to trap Fe atoms coordinating to them resulting negatively charged with respect to TCNQ/Au(111), as also confirmed by the

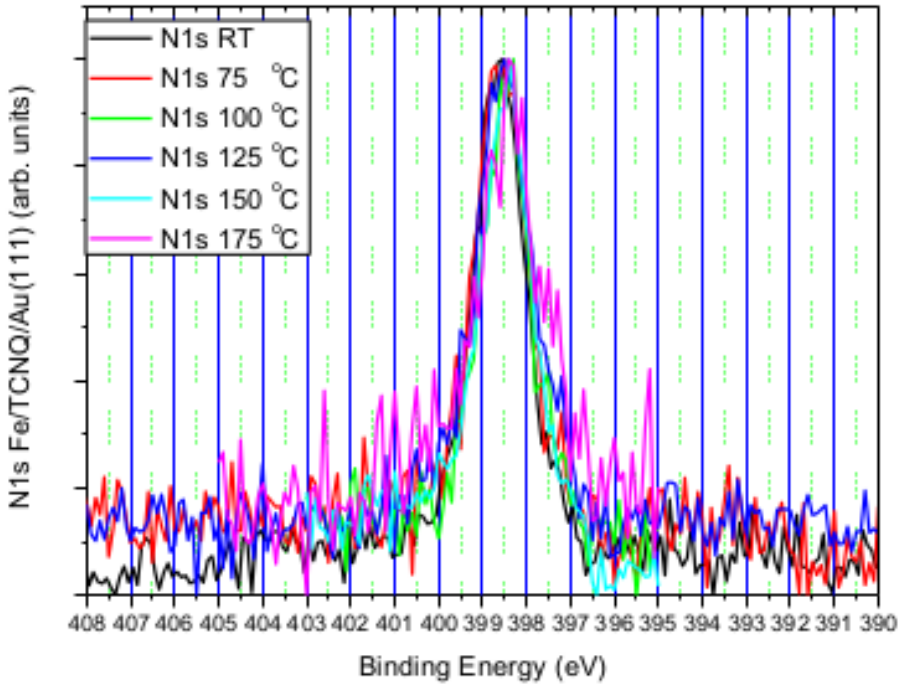

Figure 4.18: *1.0ML of Fe on TCNQ/Au(111) vs annealing. N1s at different annealing temperature. The shape and position is the same for what found for MOCN system and do not change during the annealing.*

change in shape of the orbital as shown in the insets of fig.4.16 and 4.17. Although the nitrogen atoms of TCNQ result with an excess of negative charge, the iron do not show any shift in opposite direction as in the case of MOCN. The amount of iron that is supplying electrons for nitrogen can be, therefore, considered negligible compared with the total iron on the Au(111) surface. The corresponding Fe_{2p} spectra for the different annealing temperature are shown in fig.4.19. In fact in all the spectra the main peak has the characteristic metallic shape with the peak of $Fe_{2p_{3/2}}$ located at 707.0 eV and separation energy between the doublet of Δ=13.10 eV. The Fe_{2p} shows again progressive lower slopes and gradual diminution of the intensity of Fe XPS signal as the annealing temperature increases. Following the same approach as in the previous case study, we compare the area beneath Fe_{2p} spectra. In table 4.2 are expressed

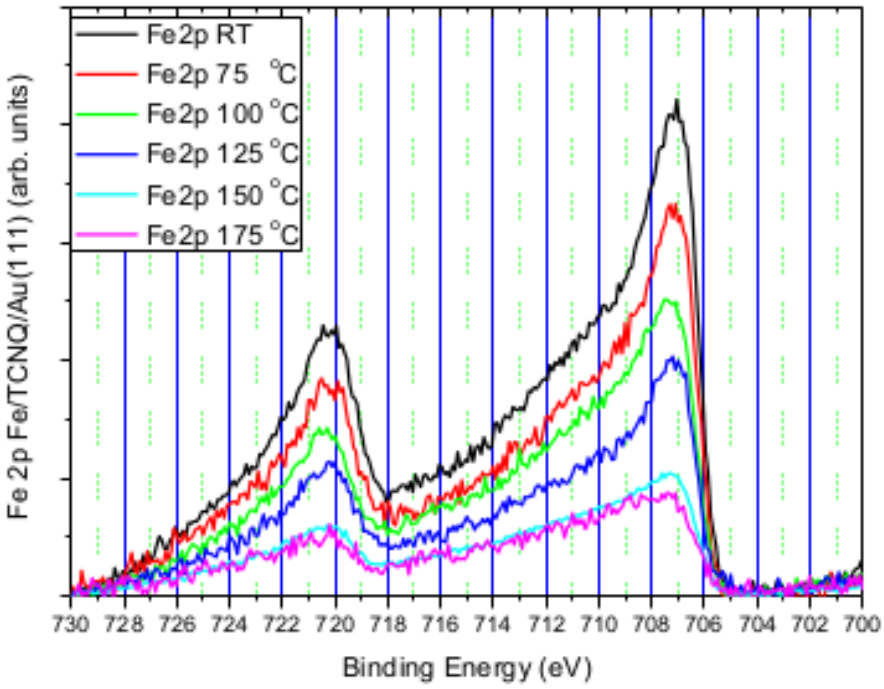

Figure 4.19: *1.0ML of Fe on TCNQ/Au(111) vs annealing. N1s at different annealing temperature. The shape and position is the same for what found for MOCN system and do not change during the annealing.*

the diminution (in percentage) of the Fe present on the surface normalized to the area of the sample as soon as Fe is deposited (RT) for both Fe/Au(111) and Fe/TCNQ/Au(111) respectively. The rate of interbulk diffusion of Fe atoms into the gold is the same till 125 °C for the two systems, while for higher temperature (150 and 175°C) the amount of Fe present on surface is considerably different. The variation for latter cases is estimated by XPS of about 20% that means ∼0.2ML, considering that the initial amount of Fe deposited was 1ML. But ∼0.2ML is the amount of Fe necessary to coordinate a complete monolayer of TCNQ and here we remember, from the previous chapter, that for MOCN systems the stability was proved up to 225°C.
Therefore we conclude that ∼0.2ML of Fe involved in the coordination with TCNQ molecules still acts as ion center as in the case of MOCN. The excess of Fe nucleates but the reduced diffusion length leads to a situation different from the case of Fe on clean Au(111) surface. The limitation in the diffusivity of Fe atoms on TCNQ/Au(111) is proven by the annealing experiments where the coalescence between islands does not lead to the same result for Fe/Au(111). The interbulk diffusion does not appear modified. The excess of Fe diffuses into gold substrate at the same rate in both cases under investigation. The difference in percentage expressed in table 4.2 at higher temperature has to be ascribed to the formation of coordination bonds that posses higher thermal stability.

Annealing Temperature	Fe/Au(111)	Fe/TCNQ/Au(111)
RT	100%	100%
75°C	97%	93%
100°C	87%	83%
125°C	73%	80%
150°C	27%	46%
175°C	20%	41%

Table 4.2: Results of the ratio between the area of Fe_{2p} at distinct annealing temperature and the area of the initial deposited amount of Fe at RT. The percentage give an indication of how much Fe is still present onto surface after the annealing cycles

4.4 Conclusions

In this chapter we studied growth mechanisms for iron in different conditions. In a first step the pseudomorphic growth of Fe on the clean Au(111) surface was studied. It was found that, independently from initial conditions, the Fe atoms are trapped in the elbows of the herringbone reconstruction and undergo to a place exchange with Au atoms of the surface and, consequently act as a nucleation site. The preferential nucleation of Fe on Au(111) surface is common for all that class of metallic elements which show higher values of surface free energy and heats of sublimation than Au. Significative differences were found when the deposition rate is rather slow when the thermodynamic effects result predominant. For low deposition rate (R=0.02 ML/min), the cross of a dislocation lines is expected to be energetically unfavorable and the islands, entirely lying on fcc or hcp domains, literally push away the reconstruction. This behaviour was also observed for other elements such as Pd and Pt. When the coverage exceeds 0.5 ML, Fe islands grow laterally in size and coalesce leading to a quasi layer-by-layer growth, however a small but non-negligible fraction of Fe has begun to grow also in the second layer. Dislocation lines appear on top of the islands and continue on the surface without any apparent lateral displacement or even a change in direction at step edge. This kind of behaviour is characteristic of a perturbed Au(111) clean surface in presence of defects, represented by the Fe atoms inserted into gold surface. On the other hand, when the deposition rate increases, the kinetic effects appears to be predominant and no inclusion of dislocation lines neither distortion of the underlying herringbone reconstruction has been observed. As a consequence the growth of Fe proceed on a natural templated substrate and, increasing the coverage, it is possible to note an initial coalescence along $[11\bar{2}]$ direction, which creates 1D structures, followed by coalescence along $[1\bar{1}0]$ directions. The pseudomorphic growth with underlying substrate is maintained up to few layers when the accumulated strain cannot be accommodated anymore and then the transition from fcc to bcc occurs, followed by topological change in the shape of the islands.
The morphology of thin films can be modified performing annealing experiments. At low annealing temperature up to 100°C the intermixing between Fe and Au is favored in the topmost layer, leading to the disappearance of islands in second layer and to drastic changes in the herringbone reconstruction which become incorporated in the islands. At higher temperatures of annealing, the interbulk diffusion is activated leading to a progressive disappearance of Fe atoms from surface and the reappearance of regular herringbone reconstruction.
On the other hand we can observe a modification of the behavior of iron on

Au(111) in presence of a monolayer of TCNQ, organic acceptor molecule. For low coverages up to θ_{Fe}=0.18 ML no growth of iron islands occurs because the Fe atoms are completely "consumed" by the coordination reaction with TCNQ. Therefore cyano groups act as diffusion traps for iron atoms better than elbows of the herringbone reconstruction. At higher coverages Fe atoms start to nucleate around one of the equivalent Fe center involved in the coordination. The free diffusion length of the impinging iron atoms is therefore reduced and this leads to smaller islands with higher surface density. Additional kinetic energy, furnished by annealing experiments, do not favour the coalescence between islands. In other words, the coordination bonds limit the intra-diffusion of Fe atoms encapsulating the islands. The interbulk diffusion instead does not result altered.

Bibliography

[1] F. Donati, G. Fratesi, M. Passoni, C. S. Casari, a. Mairov, C. E. Bottani, M. I. Trioni, and a. Li Bassi. Strain effect on local electronic properties of Fe nanoislands grown on Au(111). *Physical Review B*, 83(15):153404, April 2011.

[2] D. Weller M.L. Plumer, J. van Ek. *The Physics of Ultra-High-Density Magnetic Recording*. Springer, 2001.

[3] Karina Morgenstern, Jakob Kibsgaard, Jeppe V. Lauritsen, Erik Læ gsgaard, and Flemming Besenbacher. Cobalt growth on two related close-packed noble metal surfaces. *Surface Science*, 601(9):1967–1972, May 2007.

[4] C. Casari, S. Foglio, F. Siviero, a. Li Bassi, M. Passoni, and C. Bottani. Direct observation of the basic mechanisms of Pd island nucleation on Au(111). *Physical Review B*, 79(19):195402, May 2009.

[5] J E Prieto, J De Figuera, and R Miranda. Surface energetics in a heteroepitaxial model system : Co/Cu(111). *Physical Review B*, 62(3):2126–2133, 2000.

[6] Ernst Bauer. Phänomenologische theorie der kristallabscheidung an oberflächen. i. *Zeitschrift für Kristallographie-Crystalline Materials*, 110(1-6):372–394, 1958.

[7] FC Frank and Jan H van der Merwe. One-dimensional dislocations. i. static theory. *Proceedings of the Royal Society of London. Series A, Mathematical and Physical Sciences*, pages 205–216, 1949.

[8] IN Stranski and L Krastanov. Sitzungsberichte der akademie der wissenschaften in wien, abteilung iib, vol. 146. 1937.

[9] Thomas Michely and Joachim Krug. *Islands, mounds, and atoms: patterns and processes in crystal growth far from equilibrium*. Springer Berlin, 2004.

[10] M Volmer and A Weber. Keimbildung in übersättigten gebilden. *Z. phys. Chem*, 119:277–301, 1926.

[11] Gert Ehrlich and FG Hudda. Atomic view of surface self-diffusion: Tungsten on tungsten. *The Journal of Chemical Physics*, 44(3):1039–1049, 1966.

[12] Richard L Schwoebel and Edward J Shipsey. Step motion on crystal surfaces. *Journal of Applied Physics*, 37(10):3682–3686, 1966.

[13] Kenjiro Oura, VG Lifshits, AA Saranin, AV Zotov, and M Katayama. *Surface science: an introduction*. Springer Berlin, 2003.

[14] L. Pleth Nielsen, F. Besenbacher, I. Stensgaard, E. Laegsgaard, C. Engdahl, P. Stoltze, K. Jacobsen, and J. Nø rskov. Initial growth of Au on Ni(110): Surface alloying of immiscible metals. *Physical Review Letters*, 71(5):754–757, August 1993.

[15] S. Chiang D.D. Chambliss, R.J. Wilson. Nucleation of Ordered Ni Island Arrays on Au(111) by Surface-Lattice Dislocations. *Physical Review Letters*, 66(13):1721–1724, 1991.

[16] Harald Brune. Microscopic view of epitaxial metal growth: nucleation and aggregation. *Surface science reports*, 31(4):125–229, 1998.

[17] Peter J. Feibelman. Diffusion path for an al adatom on al(001). *Phys. Rev. Lett.*, 65:729–732, Aug 1990.

[18] R. Miranda O.S. Hernan, A.L. Vazquez de Parga, J.M. Gallego. Self-surfactant effect on Fe/Au (100): place exchange plus Au self-diffusion. *Surface Science*, 415:106–121, 1998.

[19] V. Blum, Ch. Rath, S. Müller, L. Hammer, K. Heinz, J. García, J. Ortega, J. Prieto, O. Hernán, J. Gallego, a. Vázquez de Parga, and R. Miranda. Fe thin-film growth on Au(100): A self-surfactant effect and its limitations. *Physical Review B*, 59(24):15966–15974, June 1999.

[20] Jose A Rodriguez and D Wayne Goodman. The Nature of the Metal-Metal Bond in Bimetallic Surfaces. *Science*, 257(August):897 – 903, 1992.

[21] Alexandre Delga, Jérôme Lagoute, Vincent Repain, Cyril Chacon, Yann Girard, Madhura Marathe, Shobhana Narasimhan, and Sylvie Rousset. Electronic properties of Fe clusters on a Au(111) surface. *Physical Review B*, 84(3):035416, July 2011.

[22] C Giinther, J Vrijmoeth, R Q Hwang, and R J Behm. Strain Relaxation in Hexagonally Close-Packed Metal-Metal Interfaces. *Physical Review Letters*, 74(5):754–757, 1995.

[23] C. L. Fu, A. J. Freeman, and T. Oguchi. Prediction of strongly enhanced two-dimensional ferromagnetic moments on metallic overlayers, interfaces, and superlattices. *Phys. Rev. Lett.*, 54:2700–2703, Jun 1985.

[24] Goro Honjo, Kunio Takayanagi, Kunio Kobayashi, and Katsumichi Yagi. Ultra-high-vacuum in situ electron microscopy of growth processes of epitaxial thin films. *Journal of Crystal Growth*, 42(0):98 – 109, 1977.

[25] Joseph a. Stroscio. Microscopic aspects of the initial growth of metastable fcc iron on Au(111). *Journal of Vacuum Science & Technology A: Vacuum, Surfaces, and Films*, 10(4):1981, July 1992.

[26] D. Dekadjevi, B. Hickey, S. Brown, T. Hase, B. Fulthorpe, and B. Tanner. Structural phase transition of Fe grown on Au(111). *Physical Review B*, 71(5):054108, February 2005.

[27] H. Bulou, F. Scheurer, P. Ohresser, a. Barbier, S. Stanescu, and C. Quirós. Structure of self-organized Fe clusters grown on Au(111) analyzed by grazing incidence x-ray diffraction. *Physical Review B*, 69(15):155413, April 2004.

[28] Tetsuo Okuyama. Crystallographic and magnetic properties of fe/au(001) and fe/au(111) superlattice films. *Japanese Journal of Applied Physics*, 30(9R):2053, 1991.

[29] Christian Tflkes, Peter Zeppenfeld, A Krzyzowski, and George Comsa. Growth and stability of cobalt nanostructures on gold (111). *Surface Science*, 394:170–184, 1997.

[30] Susumu Shiraki, Hideki Fujisawa, Masashi Nantoh, and Maki Kawai. The growth of Fe, Ni and Co on vicinal Au(111) surfaces. *Applied Surface Science*, 237(1-4):284–290, October 2004.

[31] C. S. Casari, S. Foglio, M. Passoni, F. Siviero, C. E. Bottani, and a. Li Bassi. Energetic regimes and growth mechanisms of pulsed laser deposited Pd clusters on Au(111) investigated by in situ scanning tunneling microscopy. *Physical Review B*, 84(15):155441, October 2011.

[32] Y. Nahas, V. Repain, C. Chacon, Y. Girard, and S. Rousset. Interplay between ordered growth and intermixing of Pt on patterned Au surfaces. *Surface Science*, 604(9-10):829–833, May 2010.

[33] Andrew W Stephenson, Christopher J Baddeley, Mintcho S Tikhov, and Richard M Lambert. Nucleation and growth of catalytically active Pd islands on Au (l l l) studied by scanning tunnelling microscopy. *Surface Science*, 398:172–183, 1998.

[34] B Fischer, JV Barth, A Fricke, L Nedelmann, and K Kern. Growth and surface alloying of al on au (111) at room temperature. *Surface science*, 389(1):366–374, 1997.

[35] M. M. Dovek, C. A. Lang, J. Nogami, and C. F. Quate. Epitaxial growth of ag on au(111) studied by scanning tunneling microscopy. *Phys. Rev. B*, 40:11973–11975, Dec 1989.

[36] CA Lang, MM Dovek, J Nogami, and CF Quate. Au (111) autoepitaxy studied by scanning tunneling microscopy. *Surface Science*, 224(1):L947–L955, 1989.

[37] JA Meyer, ID Baikie, E Kopatzki, and RJ Behm. Preferential island nucleation at the elbows of the Au(111) herringbone reconstruction through place exchange. *Surface Science Letters*, 365:647–651, 1996.

[38] J. V. Barth, H. Brune, G. Ertl, and R. J. Behm. Scanning tunneling microscopy observations on the reconstructed au(111) surface: Atomic structure, long-range superstructure, rotational domains, and surface defects. *Phys. Rev. B*, 42:9307–9318, Nov 1990.

[39] L Bardotti, P Jensen, A Hoareau, M Treilleux, B Cabaud, A Perez, and F Aires. Diffusion and aggregation of large antimony and gold clusters deposited on graphite. *Surface science*, 367(3):276–292, 1996.

[40] F. Donati, a. Mairov, C.S. Casari, M. Passoni, and a. Li Bassi. Nucleation and growth mechanisms of Fe on Au(111) in the sub-monolayer regime. *Surface Science*, 606(7-8):702–710, April 2012.

[41] Neetha a. Khan and Christopher Matranga. Nucleation and growth of Fe and FeO nanoparticles and films on Au(111). *Surface Science*, 602(4):932–942, February 2008.

[42] T Allmers and M Donath. Growth and morphology of thin Fe films on flat and vicinal Au(111): a comparative study. *New Journal of Physics*, 11(10):103049, October 2009.

[43] N.M. Amer B. Voigtlander, G. Meyer. Epitaxial growth of Fe on Au(111): a scanning tunneling microscopy investigation. *Surface Science Letters*, 255:529–535, 1991.

[44] John F Moulder, Jill Chastain, and Roger C King. *Handbook of X-ray photoelectron spectroscopy: a reference book of standard spectra for identification and interpretation of XPS data*. Perkin-Elmer Eden Prairie, MN, 1992.

[45] JoséA. Rodriguez. Physical and chemical properties of bimetallic surfaces. *Surface Science Reports*, 24(7-8):223–287, January 1996.

Chapter 5

Organic Surface Chemistry: two examples on Au(111)

This chapter is focused on the study of chemical reactions that relatively complex organic adsorbates can undergo on a metallic surface. The role of the surface can be to promote or hinder the covalent coupling between organic precursors. Also it acts like a mechanical support imposing 2D confinement. The experiments reported in this chapter will describe the possibility to exploit well-known gas phase chemical reactions in order to produce new polymers on gold surface.

5.1 Introduction

The direct and covalent interconnection of individual precursor molecules at surfaces has emerged as one promising alternative route for the bottom-up synthesis of nanostructures, in contrast with the "classic" supramolecular protocols based on non-covalent interactions[1]. In fact, a serious limitation with the supramolecular structures arises from the nature of the stabilizing forces, which are relatively weak, and so the developed bonds are reversible. Moreover these structures tend to have limited chemical and thermal stability and, hence, are too weak for applications involving templating or catalysis[2].
On the other hand by using on-surface synthesis, the structure of a superlattice can be simply programmed by the specific design of the corresponding monomers as well as by the chosen type of chemical reaction. In the literature

the structures so formed are referred as Surface Covalent Organic Frameworks (SCOFs). The advantages of this technique are numerous and very attractive. In fact the formation of non-reversible and stable covalent bonds between the molecules confers a high thermal and chemical stability to the so formed structure. Moreover, the on-surface and UHV environment allow us to use a much broader range of reaction temperatures, where the sublimation cell or substrate temperatures can be easily controlled from 4 to 600 K without risk of air oxidation or solvent decomposition. Other important aspect is the 2D confined geometry imposed by substrate that could favor some reactions that are not usually observed in solution. This can arise as result of entropic and kinetic effects or through interaction with the substrate (charge transfer)[3]. Finally the SCOFs, especially those created with precursors with extended π conjugated backbones, may also exhibit interesting in-plane carrier transportation across the new covalent bonds created[4]. However, despite those advantages, the lack of structural uniformity of such covalent networks is still a major drawback[5]. Quite generally, it originates from the irreversible character of the intermolecular coupling reactions, causing a propagation of structural defects through the entire network in combination with a possible conformation flexibility of the monomers that are used[6].
From the pioneering works in this field up to the present, several reliable chemical reactions have been studied and developed for preparing various fascinating nanostructures in UHV: Ullmann coupling[7, 8], dehydration and esterification of boronic clusters[9], imine[10] and Schiff base formation[11], and many others[12]. The surface-confined polymerization of organic adsorbates by covalent reactions is proving to be a versatile area of surface chemistry.

5.2 The polyester condensation

We will start to illustrate the power of the on-surface polymerization methods with the example of polyester condensation, which is a result of a collaboration with the groups of Prof. Jose Marìa Gòmez-Rodrìguez, Fèlix Zamora at the Department of Condensed Matter Physics of Universidad Autònoma de Madrid (Spain) and the Department of Physics of Universidade Federal de Minas Gerais (Brazil)[13]. Our contribution to this results consists mainly in the measurement of the XP spectra before and after the reaction has taken place.

In organic chemistry an ester group (O=C–OR') is a chemical compound consisting of a carbonyl (O=C–R) linked to an ether (R–OR'). Thus polyester is a category of polymers which contain ester functional group in the backbone.

In this work we take advantage of the well-established chemistry of condensation of polyesters that should allow to design on demand a wide variety of molecular architectures with a chemically inert framework. In fact, with a proper choice of reactants, structure and functionality of 2D polymers can be varied once the mechanism of polyester condensation on surface is controlled.

The reaction that we carried out involves the condensation of acylchlorides and alcohols between the benzene-1,3,5,-tricarbonyl trichloride (TMC, fig.5.1a) and the 1,3,5-tris(4-hydroxyphenyl) benzene (TPB, fig.5.1b) respectively on Au(111) surface without the use of any catalyst. The expected covalent network is porous (fig.5.1c), which confer high stability to the structure, and the pore walls are functionalized through ester bridges.

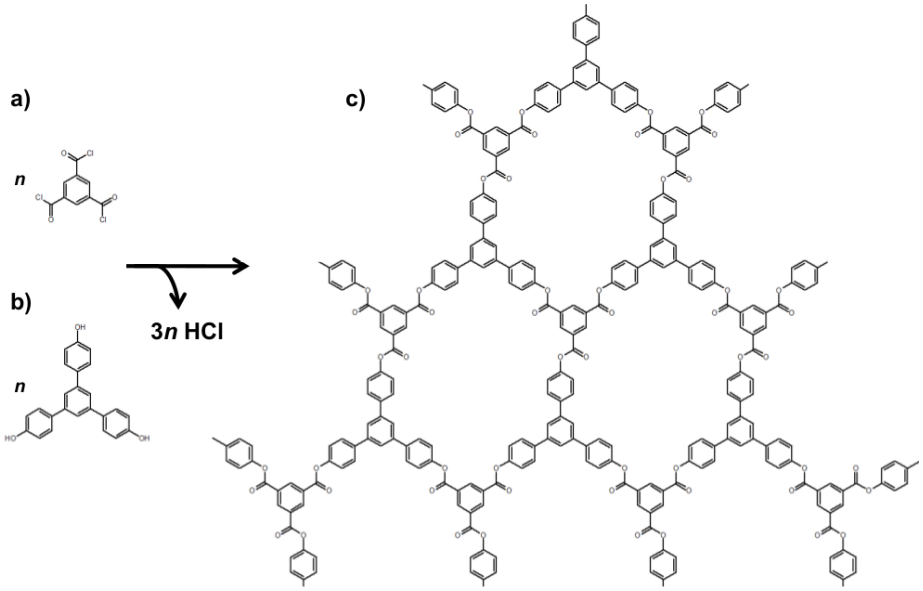

Figure 5.1: *Polyester condensation reaction scheme between (a) TMC and (b) TPB molecules to form (c) polyester-based SCOF via desorbtion of 3nHCl. The polymeric structure is strongly connected through ester groups that confer chemical and thermal stability.*

5.2.1 TPB and TMC molecules

In order to obtain the extended and regular nanoporous network of fig.5.1c, a fine tuning of reaction conditions is necessary to avoid disordered patterns. In first place it is necessary taking into account the correct stoichiometry that consists in equimolar amounts of TPB and TMC molecules. This control is achieved by a previous determination of the deposition rate for both molecules. For TPB molecules the sublimation temperature was 100 °C, that leads to a deposition rate of 0.1 ML/min on Au(111) surface. We observed that it is mandatory to have less than one monolayer of TPB on Au(111) surface, in order to leave enough space to the formation of the desired structure we want to create. The partial coverage allows the diffusion of TPB molecules over the surface, which is also a necessary condition to get later the SCOF phase. Figure 5.2 shows the STM image of a well-ordered islands of TPB molecules, that are stabilized through H-bonds between the alcohol groups. STM observations of ordered superstructure of TPB in a partially covered gold surface require low

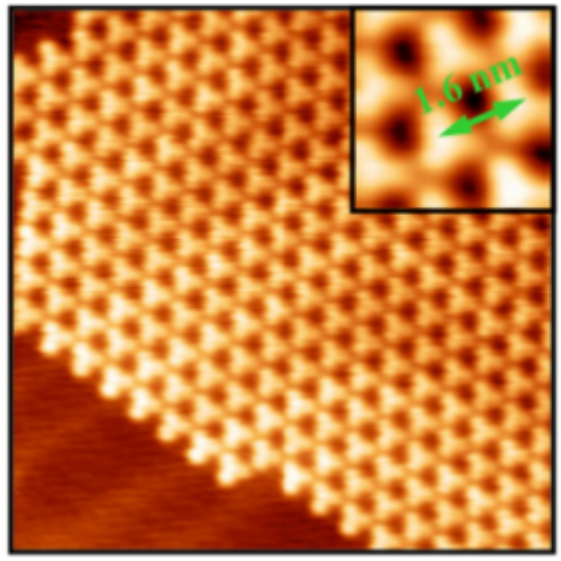

Figure 5.2: *STM image* $(25 \times 25nm^2)$ *measured at 110K of TPB on Au(111) showing well-ordered array stabilized by H–bonding. The inset shows a zoom-in view* $(4 \times 4nm^2)$*. Tunneling parameters: I=-50 pA, V=-1.6 V. Image from ref[13]*

temperature measurements(∼120 K). In fact, the high diffusivity on Au(111) surface hampers, at room temperature, the formation of homomolecular order TPB islands. In any case diffusion at room temperature of TPB molecules is something desired for the intermixing of the two reactants. On the other hand we were unable to observe homomolecular TMC superstructures due to the high mobility even at the lowest temperature we can cool down the sample during STM scans. Last parameter that had to be taken into account is the surface temperature. At room temperature the reaction does not occur on the Au(111) and a possible strategy is to heat the the surface. On the other hand, too high temperature would provoke desorption or chemical damage the organic reactants.

5.2.2 Formation of Surface Covalent Organic Frameworks

Considering all the factors presented above, we optimized the procedure to maximize the coverage and the quality of the regular extended SCOF. Typical conditions were as follows: in a base pressure $\sim 1 \times 10^{-10}$ mBar environment TPB was deposited on Au(111) at room temperature at coverage close to 0.5 ML. Then the reaction with TMC was allowed by increasing the Au(111) temperature to 575 K during 10 min while TMC was dosed through a leak valve at a partial pressure of 2×10^{-9} mBar. After that process the sample was transferred to the STM and examined at low temperature. Fig.5.3(a) shows a large-scale STM image of nearly one monolayer of the designed SCOF. In fact, the high resolution image of fig.5.3(b) presents a structure consistent with the product of the expected condensation reaction proposed in fig.5.1. The structure consists of an array of slightly irregular hexagonal cavities with an average lattice distance ∼2nm.

Figure 5.3(c) shows the Cl_{2p} and O_{1s} XP spectra taken after the deposition at room temperature of both TPB and TMC molecules on Au(111) surface (before that the reaction takes place, top) and after annealing to 575 K (bottom). The most evident change upon annealing is the almost complete disappearance of the Cl_{2p} signal as expected if the condensation reaction of fig.5.1 has occurred. On the other hand, the O_{1s} signal decreases only by ∼25%, probably due to an excess of TMC in the sample. As soon as deposited, the oxygen spectrum can be decomposed into two components: the component at 532.7 eV arises from the oxygen atoms in the hydroxyl group of TPB (C-OH), as confirmed by XP measurements of a homomolecular layer of TPB on the gold surface, while the second component is centered at 531.8 eV and corresponds to the oxygen atoms in the carbonyl (C=O) group of TMC[14]. After the annealing, the car-

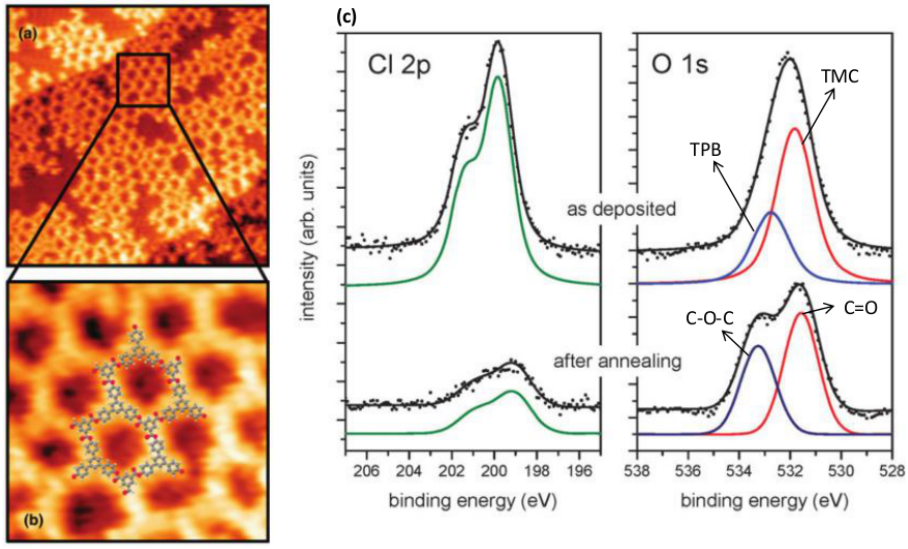

Figure 5.3: *(**a**) STM image of the SCOF formed by reaction of TPB and TMC on Au(111), ($35 \times 35 nm^2$) I=-89 pA, V=-1.6 V. (**b**) High resolution STM image ($7.5 \times 7.5 nm^2$) measured on the square area outlined in (**a**). The SCOF structure is overlaid on the STM image I=-81 pA, V=-1.8 V. (**c**) Cl 2p and O 1s photoemission spectra TPB + TMC on Au(111) at room temperature: as deposited (top) and after annealing to 575 K (bottom)[13]*

bonyl signal is still present (now at 531.6 eV due to the change of the chemical environment), but the hydroxyl peak has disappeared and a new component appears at 533.3 eV, which can be assigned to the C-O-C oxygen atom in the ester bridge(see fig.5.1)[15].
Also the carbon environment shows differences before and after annealing as shown in the fig.5.4. Contrary to the Cl_{2p} signal, and similar to the O_{1s} signal, there is only a small decrease of the total intensity (∼15%). Before the reaction takes place, the C_{1s} XP spectrum can be clearly decomposed in three components at 284.0, 285.0 and 288.7 eV. The first one is due to the carbon atoms in the benzene rings of TPB, as confirmed by XP measurements of a homomolecular layer of TPB on the gold surface. The higher binding energy signals are assigned to TMC: the component at 285.0 arises from the carbon atoms in the

benzene ring, while the peak at 288.7 eV is attributed to the carbon atoms in the Cl-C=O configuration[16]. A tentative deconvolution of the spectra after annealing is shown in the bottom panel. The signal at 288.7 eV still remains, coming from the carbon atoms in the carbonyl group of the polyester compound. In addition, there are peaks at 284.3 eV (the TPB phenyl rings), 285.0 eV, (the TMC phenyl ring)s, and a new contribution at 286.6 eV, probably due to the carbon atoms in the TPB-related rings bonded to the ester-O.

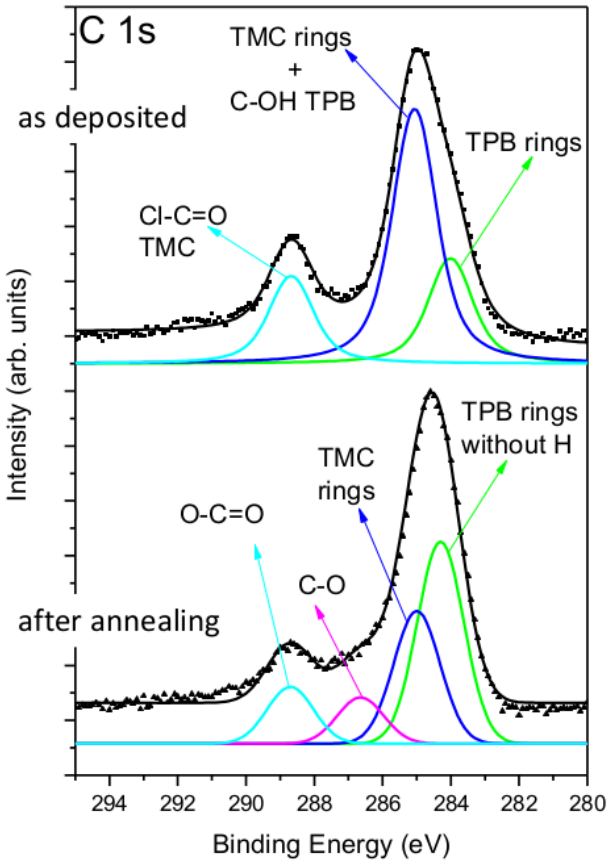

Figure 5.4: *XPS data showing the C1s spectra taken after depositing TPB + TMC on Au(111) at room temperature (top) and after annealing to 575 K (bottom).*

In conclusion this example demonstrates that condensation of polyester is a feasible strategy to generate a new family of 2D-COFs on surface. Despite the free rotation around single bonds could prevent the organized growing of 2D material on the surface, fine tuning of the reaction conditions allowed us to obtain an organized and extended porous 2D SCOF. The functionality of ester bridges allow us to envisage their potential use in molecular recognition processes. Moreover, the judicious choice of adequate building blocks will result in tuning the structure of polymer, offering a tool to tailoring on demand different levels of porosity.

5.3 Carbon homo and hetero atom bonds

The synthesis of carbon-based structure needs to distinguish between chemical reactions that lead to the formation of carbon-carbon or carbon-heteroatoms bonds. This is of fundamental importance in order to design the polymeric structure on surface with specific physical properties. Carbon-based scaffolds or novel two-dimensional materials, including graphene, are examples of all-carbon polymers[17, 18]. On the other hand, many structures of biological and technological interest are condensation polymers of small subunits stitched together by carbon-heteroatoms bonds[19].
However the number of applicable bond-forming processes at interfaces is still limited to a few reactions, recently much effort has been spent for the transposition on noble metallic surfaces of two types of well-known chemical reactions able to connect the molecular building blocks through C-C or C-X bonds respectively.

Glaser-Hay coupling

The copper mediated coupling of terminal alkyne groups was first discovered in 1869 by Carl Glaser[20]. The coupling was modified in 1962 by Allan S. Hay who used a chemical compound as solubilizing ligand for copper [21]. Nowadays the homo-coupling between alkynes through C-C covalent bond formation (fig.5.5) is commonly referred as Glaser-Hay coupling.

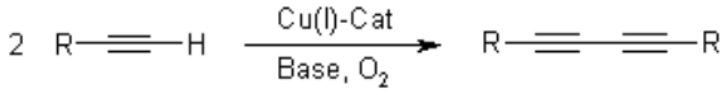

Figure 5.5: *The Glaser-Hay coupling reaction scheme between alkynes*

Very recently the alkyne homo-coupling has been been achieved on the noble surfaces[22, 23, 24, 25], showing that the Glaser coupling can be used highly efficiently to generate linear oligomer/polymer chains in spatial confined environment, which is impossible in conventional solution schemes. In fact each surface acts, more or less efficiently, as a 2D supporting system allowing to the molecules to adsorb and orient in two-dimensional space and actively takes part to mediate the reaction.

Azide-alkyne 1,3-dipolar Huisgen cycloaddition

Huisgen or 1,3-dipolar cycloaddition is a chemical reaction between a molecular 1,3-dipole (that is a dipolar compound with delocalized electrons and a separation of charge over three atoms) and a dipolarophile (that is any compound that react with 1,3-dipoles in a cycloaddiction reaction) to form a five-membered ring as illustrated in fig.5.6a. Examples of dipolarophiles are alkenes and alkynes while typical 1,3-dipolar compounds are azides or in general nitrocompound with a charged dipole. The reaction mechanism and synthetic application were established in the 1960s by Rolf Huisgen [26]. Nowadays the term Huisgen cycloaddition is often used to specifically describe the 1,3-dipolar cycloaddition between an organic azide and an alkyne to generate 1,2,3-triazole. The uncatalyzed version of this reaction requires elevated temperatures and produces mixtures of 1,4- and 1,5-triazole regioisomers as illustrated in fig. 5.6b respectively. However, it is possible to select the regioselectivity by using catalyzed version of the reaction, in particular the copper-catalyzed cycloaddition selectively produces 1,4-triazole while a ruthenium-catalyzed version gives the opposite regioselectivity.
The Huisgen cycloaddition belongs to a set of powerful, highly reliable, and selective reactions for the rapid synthesis of useful new compounds through heteroatom links (C–X–C). This approach is called "click chemistry"[27]. The criteria to belong to click reactions are very selective and include reactions that must be wide in scope, give very high yields, generate only inoffensive

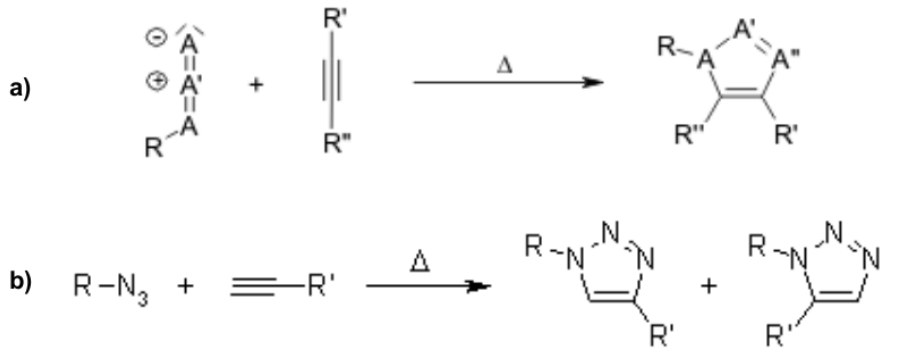

Figure 5.6: *(a) Huisgen (1,3-Dipolar) cycloaddition reaction scheme; (b) Uncatalyzed azide-alkyne 1,3-dipolar Huisgen cycloaddition generates 1,2,3-triazole in 1,4- and 1,5-triazole regioisomers, respectively.*

byproducts, stereospecific and simple to perform. Such kind of reactions have been used, in solution phase processes, for the modification of surfaces [28] and materials[29] and also for the preparation of biologically active compounds for drug discovery[30]. Recently two examples of successful azide-alkyne cycloaddition on Cu(111)[31] and Au(111)[32] have been published, however on both surfaces, the on-surface reaction shows an incredible low yield compared with solution phase.

5.3.1 Hierarchical organic reactions on Au(111)

In collaboration with the group of Prof. Tomàs Torres at the Department of Organic Chemistry of Universidad Autònoma de Madrid, we have synthesized the 1-(azidomethyl)-4-((4-((4-ethynylphenyl)ethynyl)phenyl)ethynyl) benzene molecule shown in figure5.7. In order to simplify the following discussion, we will refer to this molecule as "Click 1" molecule.

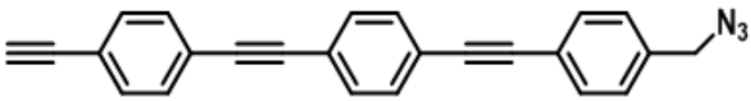

Figure 5.7: *The 1-(azidomethyl)-4-((4-((4-ethynylphenyl)ethynyl)phenyl)ethynyl)benzene molecule: the backbone chain is formed by three phenyl rings connected by carbon-carbon triple bonds. The boundaries are functionalized with the azide and alkyne groups respectively in order to study a hierarchical pattern in the chemical reactions on the Au(111) surface. In order to simplify the following discussion, we will refer to this molecule as "Click 1" molecule.*

The "Click 1" molecule is composed by a linear chain of three phenyl rings connected each other through triple bonds that confer high rigidity to the structure and assure an adsorption almost planar on surface. The boundaries are functionalized with the azide and alkyne groups respectively. The design of the molecule permits us to explore both reactions presented above on Au(111) surface. In fact, due to the proper choice of terminal groups, both Glaser coupling and Huisgen cycloaddition can take place depending to the way they approach each other. Also the role of the surface is of primary importance, in fact, acting as 2D mechanical support on which the molecules arrange their position, the developed interactions can selectively promote or hinder a specific covalent coupling. Therefore the role of the surface can lead to a hierarchical classification scheme for the on surface chemical reactions.

The deposition of "Click 1" molecules on Au(111) surface at room temperature leads to a situation shown in figure5.8. Long linear chains characterized by the alternation of bright and dark lobes appear on surface. The periodicity between brightest lobes is experimentally estimated $\sim 50\mathring{A} \pm 5\mathring{A}$ in both directions they appear. Also the smaller and darker lobes has a periodicity of $\sim 50\mathring{A} \pm 5\mathring{A}$. Such distance is not compatible with the length of one molecule, which is estimated to be 23 Å in gas phase. It is worth noting that between the dark and bright lobes appears three consecutive small protrusions which have a distance compatible with the expected phenyl-phenyl distance. This configuration leads to two different hypothesis.

Hypothesis 1: each molecule approaches the following with the right orientation to perform the azide-alkyne cycloaddition. In other words alkyne (azide) group belonging to a molecule approaches the azide (alkyne) group belonging to a neighboring molecules. The alternation between dark and bright lobes, in this view, is due to different spatial arrangement of the triazoles that explains the different STM contrast.

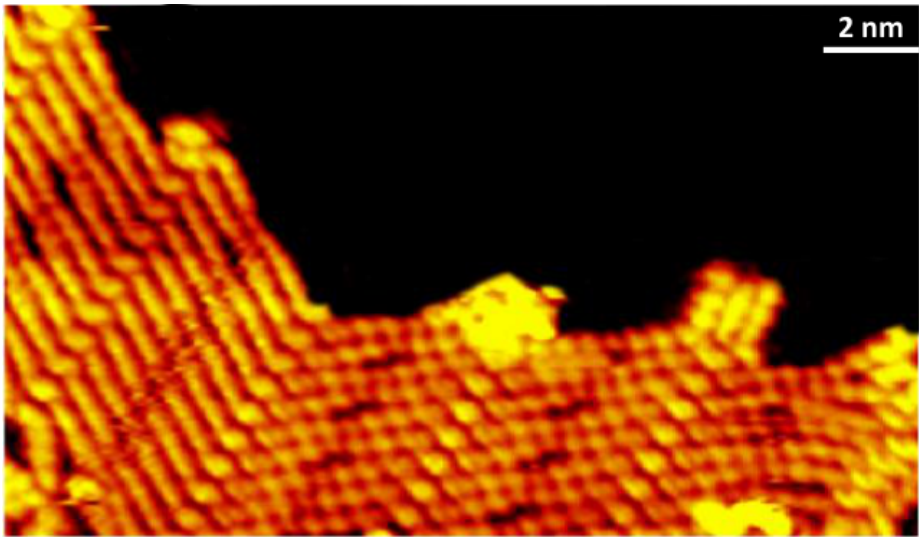

Figure 5.8: *STM image ($197 \times 115\mathring{A}^2$) of Click 1 molecules deposited at RT on Au(111) surface. Long linear chains appear on surface characterized by the alternation of bright and dark lobes each tree protrusions compatible with the expected phenyl-phenyl distance (I_t=-0.12 nA ; V_t=-1170 mV).*

Hypothesis 2: each molecule approaches the following with the opposite orientation. It means that the molecules tend to approach each others by the same functionalized group, azide with azide and alkyne with alkyne. Within this hypothesis, the Huisgen reaction cannot occur and the alternation of bright and dark lobes is the result of homo-coupling between alkynes groups and the azides. Thus the alternation between dark and bright lobe is due to different chemical species.

Triazole and azide references

Within this scenario, to definitively validate one of the hypotheses presented above, it is important to compare the N_{1s} environment experienced by "Click 1" molecules to the triazole moiety lying intact on Au(111) surface, that will correspond to the case of successful Huisgen cycloaddition (the final product of the reaction in fig.5.6 b). On the other hand, it is also important have a reference for the azide un-reacted environment. For these reasons, we decided to perform control experiments with organic molecules properly functionalized with the chemical groups that will correspond to the situations described by the hypothesis 1 and 2 for the nitrogen atoms. Figure 5.9a shows the chemical formula of 4-Phenyl-1-(1-pyrenemethyl)-1H-1,2,3-triazole, composed by pyrene and phenyl moieties connected through a triazole ring. The hypothesis 1 leads to the same chemical environment for nitrogen atoms due to the reaction of the alkyne and azide groups. The molecule shows in fig.5.9b is the 1-(azidomethyl)-pyrene and it will be used as reference for the un-reacted azide group, a situation similar to what experienced by nitrogen atoms if the hypothesis 2 occurred.

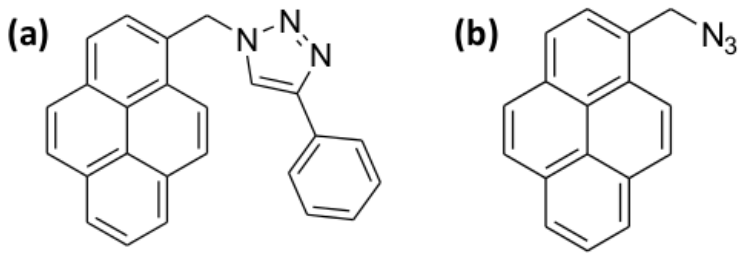

Figure 5.9: *(**a**)The 4-Phenyl-1-(1-pyrenemethyl)-1H-1,2,3-triazole contains the triazole as in the case of the occurrence of the hypothesis 1; (**b**) the 1-(azidomethyl)-pyrene with the un-reactide azide group is associated with the hypothesis 2.*

Deposition at room temperature of the molecule in fig.5.9(a) on Au(111) surface leads to a situation shown in the STM image of fig.5.10a. An order superstructure is formed by asymmetric protrusions whose shape and the geometrical parameters fit a simple molecular model in gas phase. This would suggest that the triazole moiety remains unaltered upon the adsorption on Au(111) surface. The N_{1s} spectrum in fig.5.10(b) shows a peak at 399.7 eV and can be deconvoluted in two contributions: the first more intense peak at 399.6 eV (FWHM=1.5 eV) and another at 401.1 eV (FWHM=0.94 eV) with a 2:1 ratio of the peak areas reflecting two distinct chemical environments for nitrogen (nitrogens in 1 and 3 position in the triazole in cyano and 2 in orange). The energy difference of 1.5 eV between these two peaks and the area ratio 2:1 is a common XPS fingerprint of 1,2,3-triazole group[31, 33, 34, 35]. Thus, it is possible to affirm that the triazole moieties lie on the surface without undergoing decomposition or irreversible chemical changes on Au(111) surface. This assures that the product of the Huisgen cycloaddition will survive after a successful surface reaction process.

On the other hand, figure5.11a shows the STM image of deposition of the azide test molecule molecule (fig.5.9b) at room temperature. The STM image confirms the presence of adsorbed molecules however no details are available with STM measurements. The corresponding N_{1s} XP spectrum is shown in fig.5.11b (red curve) together with the triazole reference (blue curve). The dif-

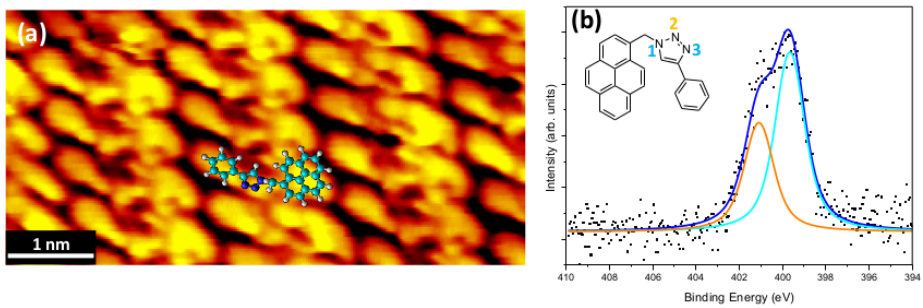

Figure 5.10: *(**a**)Molecules present shape and dimensions that fit very well the molecular model in gas phase. STM details:87×34Å^2 I=-0.210 nA ; V=-1650 mV; (**b**) N1s spectrum of final product of 1,3-Huisgen cycloaddition reaction. N atoms in position 1,3 in the triazole have the same chemical environment (blue curve), while N atoms in position 2 has a different one (dark cyan curve). The expected ratio 2:1 is confirmed by the ratio of the areas below each component.*

ference between the position in binding energy of the peaks of the N_{1s} spectra is measured to be $\sim$ 1.6 eV. In particular the azide (red) spectrum results centered at 398.0 eV, shifted towards lower binding energy with respect to triazole (blue) spectrum. In any case we are not able to discriminate if the azide group undergoes to chemical changes upon the adsorption on Au(111) surface. What is important to underline is that there is a clear difference in the nitrogen environment detectable by XPS between the N_{1s} spectra of triazole and azide.

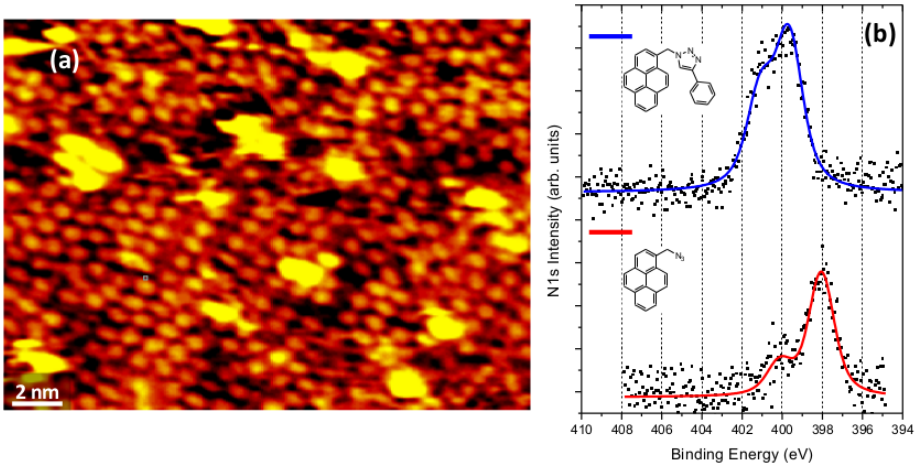

Figure 5.11: *(**a**)Deposition of 1-(azidomethyl)-pyrene on Au(111) surface at room temperature. The STM image confirms the presence of adsorbed molecules (210×154Å^2 I=-0.2 nA ; V=-870 mV); (**b**) Comparison between N1s spectra of the test molecules of fig.5.9. The difference of 1.7 eV between the peak positions permits a clear identification of the distinct nitrogen environment.*

5.3.2 Glaser coupling vs Huisgen cycloaddition

At this point, to validate one of the two initial hypothesis upon deposition of "Click 1" molecules on Au(111) surface, we have compared in fig.5.12the XP spectra for N_{1s} of the triazole (blue), the unreacted azide (red) with the "Click 1" molecule (green).
It clearly appears that the N_{1s} XP spectrum of the "Click 1" molecules (in green) resembles to the spectrum of the unreacted azide (in red). Both have the position of the peak centered at 398.0 eV and shifted by 1.6 eV towards

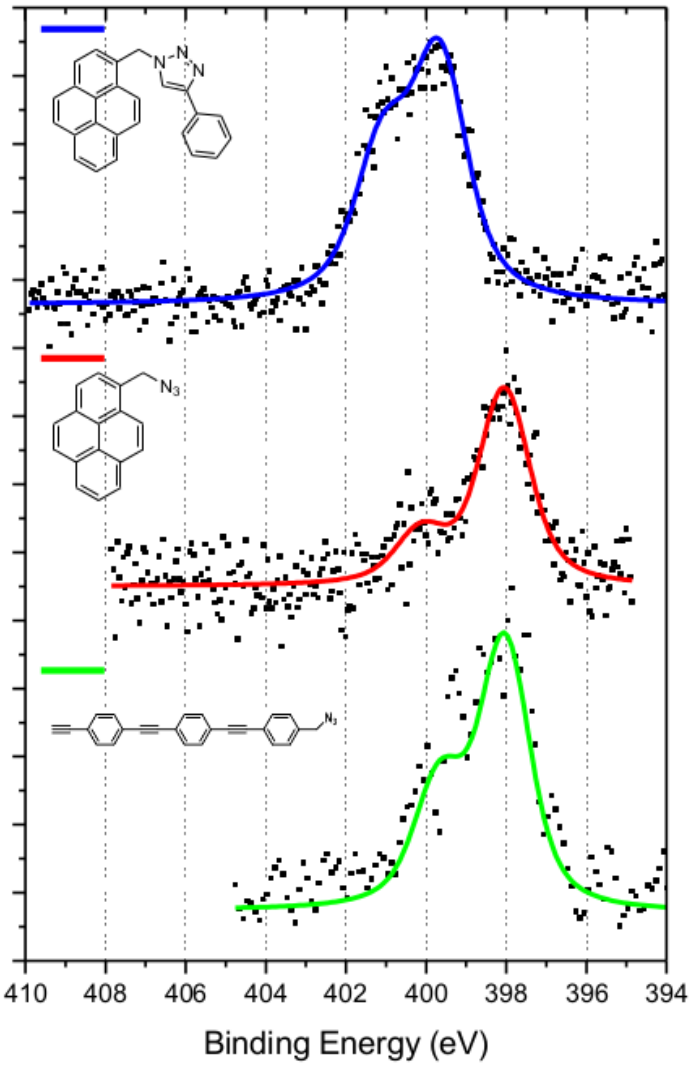

Figure 5.12: *Comparison between the N1s XP spectra of triazole group (blue), unreacted azide group (red) and nitrogen environment of "Click I"(green) on Au(111) surface.*

lower binding energy with respect to triazole reference. This result consolidates the Hypothesis 2 that assigns the alternation of dark and bright lobes in the STM image upon the adsorption of "Click 1" molecules (fig.5.8) to the result of interactions between alkyne-alkyne and azide-azide groups. In this picture, a dimer of "Click 1" obtained through Glaser coupling of alkyne groups has a theoretical bond length obtained by simple model in the gas phase of 48.4$\mathring{A}$, that is in agreement with the bright lobe-to-lobe distance measured to be 49$\mathring{A}\pm$ 5$\mathring{A}$ as shown by the model of a Glaser-dimered "Click 1" molecules superimposed to the STM image in figure5.13. It is worth noticing that the Glaser dimers in the STM images do not appear perfectly linear, but sometimes they appear bent where the Glaser coupling has occurred. The difference in arrangement could be due either to steric hindrance imposed by 2D confinement. Other possible explanation is that, together with the dehydrogenative homocoupling of two alkyne functionalities (which is the proper Glaser coupling as shown in fig.5.5), other types of hydroalkynylation processes, that are the reaction with alkynes with consequent losing of hydrogen atoms, can occur as shown by recent similar works on Au(111) surface[22, 23].

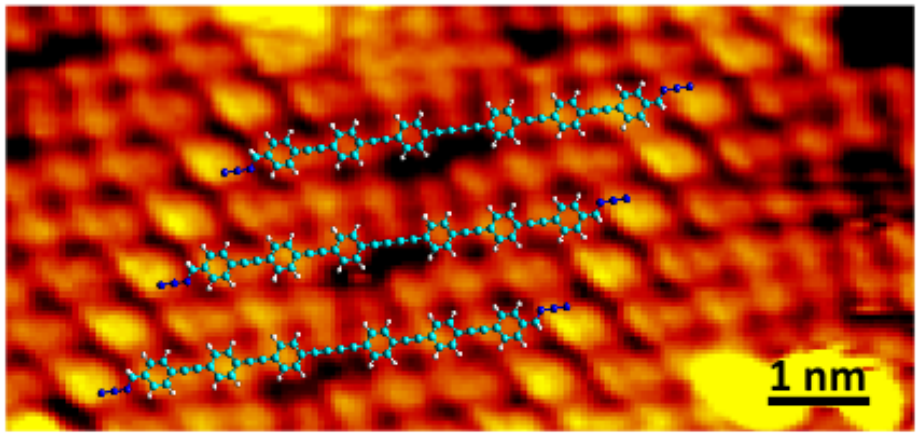

Figure 5.13: *STM image (156×57Å^2) with superimposed model of dimer consisting of two "Click 1" molecules bound through Glaser coupling between alkyne group. The Glaser dimer has a theoretical bond length in the gas phase of 48.4Å, that is in agreement with the bright lobe-to-lobe distance measured to be 49Å± 5Å. The azide groups of the molecules are supposed un-reacted and probably the interaction of two of them produce the bright lobe(I=-0.04 nA ; V=-2152 mV).*

In order to study if the preferential Glaser coupling with respect to Huisgen cycloaddition is a process that is thermally dependent, we deposited the "Click 1" molecules on Au(111) surface at low temperature. The STM image in figure5.14(a) is acquired upon the deposition at low temperature ($\sim$ 100 K) of "Click 1" molecules. At low temperature it is possible to observe the lack of linear chains with an alternation between bright and dark lobes that characterize the room temperature deposition. Molecules seem to chaotically disposed on Au(111) surface and no formation of order supramolecular structure is observed. When the temperature is raised up to room temperature, the STM image in figure5.14(b) reveals a situation similar to that described when molecules are directly deposited on Au(111) substrate at room temperature, confirming that the process is thermally activated. Figure 5.14(c) shows the XP spectra of N_{1s}

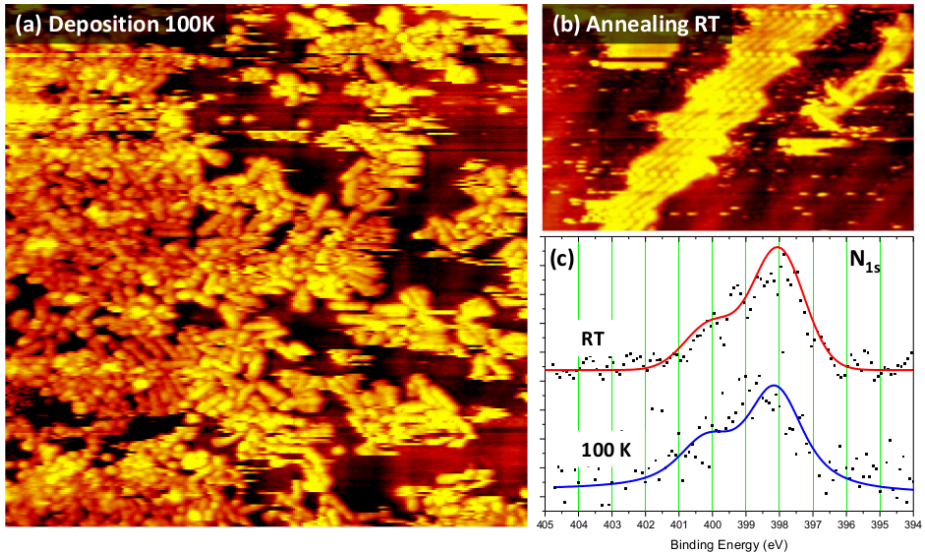

Figure 5.14: *(**a**) Click I deposited on Au(111) at $\sim$100 K, molecules appear chaotically ordered and no linear chains appears on the surface; (**b**) Consequent annealing up to RT shows the characteristic alternation between bright and dark lobes. (**c**) N1s spectra of the samples **a** at low temperature (blue spectrum) and **b** at room temperature (red spectrum). No changes neither in position nor in the shape of the XP spectra it is observed. The morphological variation are thus due to changes in the carbon chemical environment, although the resolution of our detector does no chemical distinguish with the necessary precision such variation.*

of the samples in fig.5.14a and b respectively. Both spectra have the maximum peak centered at 398.0 eV and no significative difference in shape are appreciable. This suggests that there is no difference in nitrogen environment between cold and room temperature deposition despite the difference in STM images. Therefore, only a variation in the chemical environment of the carbon atoms can be the responsible of the chemical changes that appear in STM images of fig.5.14a and b. Unfortunately the resolution of our detector does no permit to distinguish with the necessary precision such variation.

5.3.3 Discussion

The validation of the Hypothesis 2 leads to the conclusion that the alkyne groups on Au(111) surface at room temperature tends to recognize each others and to react between themselves. The carbon homo-coupling behaviour of this group is thus a preferential strategy with respect to carbon hetero atoms coupling. In order to understand why, we deposited much more than 1ML of "Click 1" molecules in order to form a thick multilayer on Au(111) surface. This strategy is useful to understand the role of the substrate. In fact, molecules in multilayer are not in direct contact with surface and they, increasing the thickness of the film, tend to behaviour as they was in condensed bulk structure.
The XPS N_{1s} of multilayer structure is shown in yellow in the fig.5.15 together with the other nitrogen environments studied so far. The N_{1s} XP spectrum of the multilayer reveals a structure formed by a main peak centered at 399.3 eV and a less intense peak at 404.5 eV which is unusual for an organic nitrogen. In literature this peak is a commonly accepted signature for azide group, that is assigned to the central, electron-deficient nitrogen atoms in the molecular 1,3-dipole[34, 35, 36]. The N_{1s} spectra of azide in contact with Au(111) substrate (red and green spectra) show a different behaviour. The lack of the peak at higher binding energy and the shift of the peak towards lower energy suggests the idea that Au(111) surface compensates the inhomogeneity in the charge separation over the nitrogen atoms in azide 1,3-dipolar group. To be sure of that we also performed chromatography of the "Click 1" molecules before and after sublimation in UHV environment. The results confirm that the molecules neither undergo to a degradation nor to homo-coupling for effect of thermal sublimation. This lead to the conclusion that the only responsible of the observed behaviour is the Au(111) surface. Such electrical compensation hinders the Huisgen cycloaddition, probably due to the lowering of the reactivity of the azide groups. This interpretation explains the low yield shown by the on-surface click reaction (about 1%) in recent works.

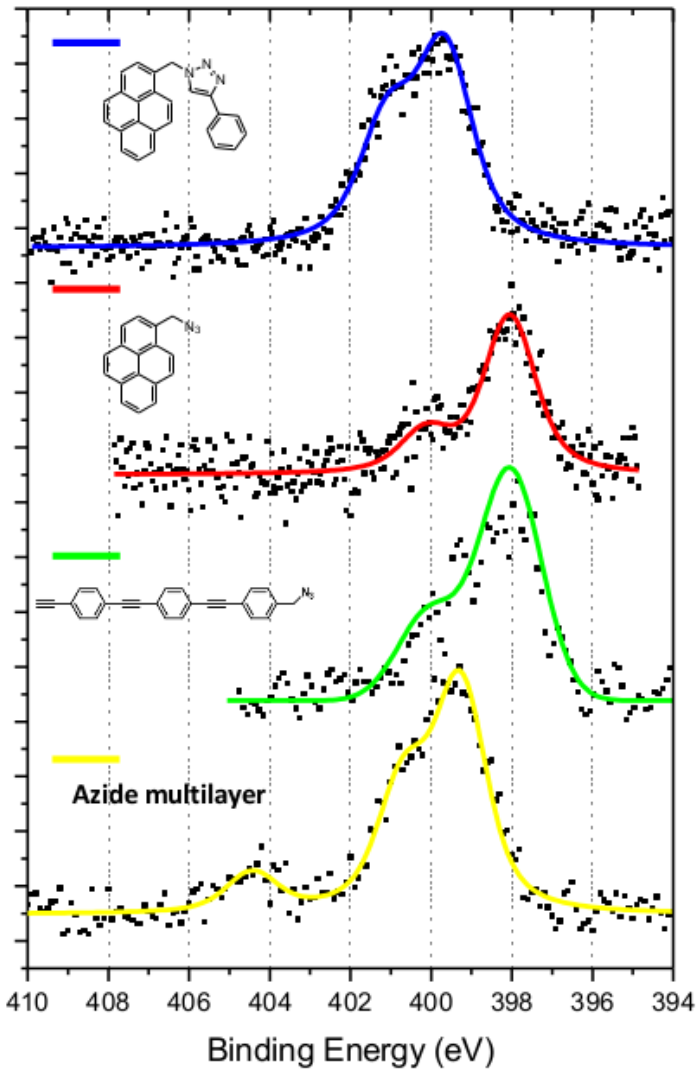

Figure 5.15: *Comparison between the N1s XP spectra of triazole group (blue), unreacted azide group (red), nitrogen environment of "Click I"(green) and "Click 1" multilayer (yellow) on Au(111) surface.*

Simple theoretical calculations suggests the ideas that an azide group with compensated charge over the group shows the tendency to react with neighboring azide losing 1 molecule of molecular nitrogen (fig.5.16a) or to form a coordination network with an Au atom of the surface (fig.5.16b).

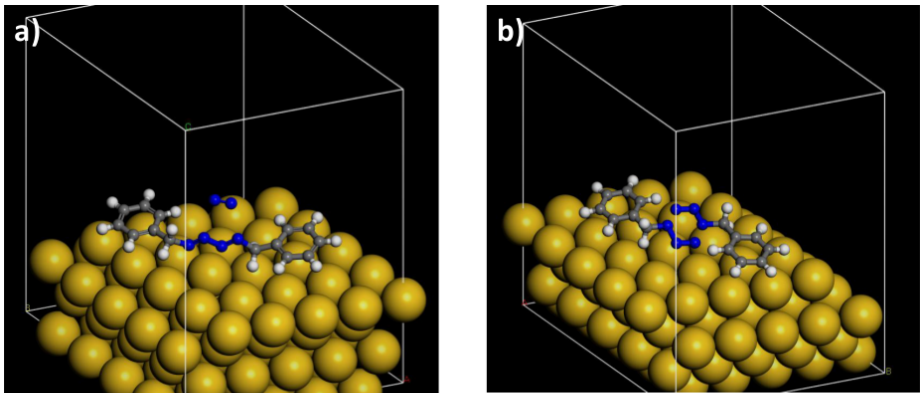

Figure 5.16: *Simple theoretical calculations reveals that an azide group with compensated charge over the group shows the tendency (**a**) to react with neighboring azide losing 1 molecule of molecular nitrogen; (**b**) to form a coordination network with an Au atom of the surface*

5.4 Conclusion

In this chapter we studied the transposition on Au(111) surface of some well-known liquid phase chemical reactions. The polyester condesation is the first example and it was obtained by intermixing two molecular units with the boundaries funtionalized with acylchloride and alcohol groups. The polymerization occurs through the reaction of these two groups with the release of hydrochloric acid to form ester bridges that covalently connect the subunits. The high resolution STM image shows that the structure so formed is consistent with the product of the expected condensation, as well as the XPS results. In fact drastic reduction of chlorine signal upon soft annealing confirms that hydrochloric acid leaves the surface. Also the oxygen and carbon environment changes, revealing the formation of ester bridges by the appearance of new peaks at specific binding energies. The mechanism of polyester condensation on surface is thus a good strategy for the controlled of extended polymers and the well-established chemistry of condensation of polyesters can be used to design on demand a wide variety of molecular architectures with chemically inert framework on surface. The optimization and the application of this approach can be reliably used for nano-engineering.

In order to complete manage the on-surface reactions it is important to distinguish between chemical reactions that lead to the formation of carbon-carbon over carbon-heteroatoms bonds. To this purpose we used a molecules that, due to the proper choice of terminal groups, allow both Glaser coupling and Huisgen cycloaddition on Au(111) surface. In order to search an hierarchical order of the on-surface reaction, we performed several experiments. In first place we proved that triazole moiety adsorbs intact on Au(111) surface at room temperature, which leads to the conclusion that at least the product of the Huisgen cycloaddition can survive on surface without undergoing to chemical degradation. Although this fact, the molecules on Au(111) surface prefer to approach the following ones with the orientation to perform Glaser coupling. The reason why the carbon homo-coupling is a preferential strategy with respect to carbon hetero atoms coupling has to search in the effect of the Au(111) surface on the azide groups. In fact, an azide group is characterized by separation of charge over three nitrogen atoms and delocalization of electrons among them. Once absorbed on the surface, the substrate tries to compensate the imbalance of charge donating electrons and probably lowering the reactivity of the azide groups. This interpretation would also give an explanation to the observed low yield of the Huisgen cycloaddition onto noble metallic surfaces.

Bibliography

[1] Andre Gourdon. On-surface covalent coupling in ultrahigh vacuum. *Angewandte Chemie International Edition*, 47(37):6950–6953, 2008.

[2] J Greenwood and CJ Baddeley. Formation of imine oligomers on au under ambient conditions investigated by scanning tunneling microscopy. *Langmuir*, 29(2):653–657, 2013.

[3] Grégory Franc and André Gourdon. Covalent networks through on-surface chemistry in ultra-high vacuum: state-of-the-art and recent developments. *Physical Chemistry Chemical Physics*, 13(32):14283–14292, 2011.

[4] Xuan-He Liu, Cui-Zhong Guan, San-Yuan Ding, Wei Wang, Hui-Juan Yan, Dong Wang, and Li-Jun Wan. On-surface synthesis of single-layered two-dimensional covalent organic frameworks via solid–vapor interface reactions. *Journal of the American Chemical Society*, 135(28):10470–10474, 2013.

[5] Dmitrii F Perepichka and Federico Rosei. Chemistry. extending polymer conjugation into the second dimension. *Science (New York, NY)*, 323(5911):216–217, 2009.

[6] Christoph H Schmitz, Julian Ikonomov, and Moritz Sokolowski. Two-dimensional polyamide networks with a broad pore size distribution on the ag (111) surface. *The Journal of Physical Chemistry C*, 115(15):7270–7278, 2011.

[7] Saw-Wai Hla, Ludwig Bartels, Gerhard Meyer, and Karl-Heinz Rieder. Inducing all steps of a chemical reaction with the scanning tunneling microscope tip: towards single molecule engineering. *Physical review letters*, 85(13):2777, 2000.

[8] Leonhard Grill, Matthew Dyer, Leif Lafferentz, Mats Persson, Maike V Peters, and Stefan Hecht. Nano-architectures by covalent assembly of molecular building blocks. *Nature nanotechnology*, 2(11):687–691, 2007.

[9] Nikolas AA Zwaneveld, Rémy Pawlak, Mathieu Abel, Daniel Catalin, Didier Gigmes, Denis Bertin, and Louis Porte. Organized formation of 2d extended covalent organic frameworks at surfaces. *Journal of the American Chemical Society*, 130(21):6678–6679, 2008.

[10] Sigrid Weigelt, Carsten Busse, Christian Bombis, Martin M Knudsen, Kurt V Gothelf, Erik Lægsgaard, Flemming Besenbacher, and Trolle R Linderoth. Surface synthesis of 2d branched polymer nanostructures. *Angewandte Chemie International Edition*, 47(23):4406–4410, 2008.

[11] Lirong Xu, Xin Zhou, Yanxia Yu, Wei Quan Tian, Jun Ma, and Shengbin Lei. Surface-confined crystalline two-dimensional covalent organic frameworks via on-surface schiff-base coupling. *ACS nano*, 7(9):8066–8073, 2013.

[12] Florian Klappenberger. Two-dimensional functional molecular nanoarchitectures–complementary investigations with scanning tunneling microscopy and x-ray spectroscopy. *Progress in Surface Science*, 89(1):1–55, 2014.

[13] Antonela C Marele, Rubén Mas-Ballesté, Luigi Terracciano, Jonathan Rodríguez-Fernández, Isadora Berlanga, Simone S Alexandre, Roberto Otero, José M Gallego, Félix Zamora, and José M Gómez-Rodríguez. Formation of a surface covalent organic framework based on polyester condensation. *Chemical Communications*, 48(54):6779–6781, 2012.

[14] Dietmar Payer, Alessio Comisso, Alexandre Dmitriev, Thomas Strunskus, Nian Lin, Christof Wöll, Alessandro DeVita, Johannes V Barth, and Klaus Kern. Ionic hydrogen bonds controlling two-dimensional supramolecular systems at a metal surface. *Chemistry-A European Journal*, 13(14):3900–3906, 2007.

[15] Gabriel P López, David G Castner, and Buddy D Ratner. Xps o 1s binding energies for polymers containing hydroxyl, ether, ketone and ester groups. *Surface and interface analysis*, 17(5):267–272, 1991.

[16] Dietmar Payer, Alessio Comisso, Alexandre Dmitriev, Thomas Strunskus, Nian Lin, Christof Wöll, Alessandro DeVita, Johannes V Barth, and Klaus Kern. Ionic hydrogen bonds controlling two-dimensional supramolecular systems at a metal surface. *Chemistry-A European Journal*, 13(14):3900–3906, 2007.

[17] François Diederich and Milan Kivala. All-carbon scaffolds by rational design. *Advanced Materials*, 22(7):803–812, 2010.

[18] JA Rogers, MG Lagally, and RG Nuzzo. Synthesis, assembly and applications of semiconductor nanomembranes. *Nature*, 477(7362):45–53, 2011.

[19] Hartmuth C Kolb and K Barry Sharpless. The growing impact of click chemistry on drug discovery. *Drug discovery today*, 8(24):1128–1137, 2003.

[20] C Glaser. Beiträge zur kenntniss des acetenylbenzols. *Berichte der deutschen chemischen Gesellschaft*, 2(1):422–424, 1869.

[21] Allan S Hay. Oxidative coupling of acetylenes. ii1. *The Journal of Organic Chemistry*, 27(9):3320–3321, 1962.

[22] Hong-Ying Gao, Jörn-Holger Franke, Hendrik Wagner, Dingyong Zhong, Philipp-Alexander Held, Armido Studer, and Harald Fuchs. Effect of metal surfaces in on-surface glaser coupling. *The Journal of Physical Chemistry C*, 117(36):18595–18602, 2013.

[23] Hong-Ying Gao, Hendrik Wagner, Dingyong Zhong, Jörn-Holger Franke, Armido Studer, and Harald Fuchs. Glaser coupling at metal surfaces. *Angewandte Chemie International Edition*, 52(14):4024–4028, 2013.

[24] Hong-Ying Gao, Dingyong Zhong, Harry Mönig, Hendrik Wagner, Philipp-Alexander Held, Alexander Timmer, Armido Studer, and Harald Fuchs. Photochemical glaser coupling at metal surfaces. *The Journal of Physical Chemistry C*, 118(12):6272–6277, 2014.

[25] Yi-Qi Zhang, Nenad Kepčija, Martin Kleinschrodt, Katharina Diller, Sybille Fischer, Anthoula C Papageorgiou, Francesco Allegretti, Jonas Björk, Svetlana Klyatskaya, Florian Klappenberger, et al. Homo-coupling of terminal alkynes on a noble metal surface. *Nature communications*, 3:1286, 2012.

[26] Rolf Huisgen. 1.3-dipolare cycloadditionen rückschau und ausblick. *Angewandte Chemie*, 75(13):604–637, 1963.

[27] Hartmuth C Kolb, MG Finn, and K Barry Sharpless. Click chemistry: diverse chemical function from a few good reactions. *Angewandte Chemie International Edition*, 40(11):2004–2021, 2001.

[28] James P Collman, Neal K Devaraj, Todd PA Eberspacher, and Christopher ED Chidsey. Mixed azide-terminated monolayers: a platform for modifying electrode surfaces. *Langmuir*, 22(6):2457–2464, 2006.

[29] Himabindu Nandivada, Xuwei Jiang, and Joerg Lahann. Click chemistry: versatility and control in the hands of materials scientists. *Advanced Materials*, 19(17):2197–2208, 2007.

[30] Christian W Tornøe, Caspar Christensen, and Morten Meldal. Peptidotriazoles on solid phase:[1, 2, 3]-triazoles by regiospecific copper (i)-catalyzed 1, 3-dipolar cycloadditions of terminal alkynes to azides. *The Journal of organic chemistry*, 67(9):3057–3064, 2002.

[31] Fabian Bebensee, Christian Bombis, Sundar-Raja Vadapoo, Jacob R Cramer, Flemming Besenbacher, Kurt V Gothelf, and Trolle R Linderoth. On-surface azide–alkyne cycloaddition on cu (111): Does it "click" in ultrahigh vacuum? *Journal of the American Chemical Society*, 135(6):2136–2139, 2013.

[32] Oscar Díaz Arado, Harry Mönig, Hendrik Wagner, Jörn-Holger Franke, Gernot Langewisch, Philipp Alexander Held, Armido Studer, and Harald Fuchs. On-surface azide–alkyne cycloaddition on au (111). *ACS nano*, 7(10):8509–8515, 2013.

[33] Bin Guan, Simone Ciampi, Guillaume Le Saux, Katharina Gaus, Peter J Reece, and J Justin Gooding. Different functionalization of the internal and external surfaces in mesoporous materials for biosensing applications using "click" chemistry. *Langmuir*, 27(1):328–334, 2010.

[34] Anando Devadoss and Christopher ED Chidsey. Azide-modified graphitic surfaces for covalent attachment of alkyne-terminated molecules by "click" chemistry. *Journal of the American Chemical Society*, 129(17):5370–5371, 2007.

[35] James P Collman, Neal K Devaraj, Todd PA Eberspacher, and Christopher ED Chidsey. Mixed azide-terminated monolayers: a platform for modifying electrode surfaces. *Langmuir*, 22(6):2457–2464, 2006.

[36] Gilad Zorn, Li-Hong Liu, Líney Árnadóttir, Hui Wang, Lara J Gamble, David G Castner, and Mingdi Yan. X-ray photoelectron spectroscopy investigation of the nitrogen species in photoactive perfluorophenylazide-modified surfaces. *The Journal of Physical Chemistry C*, 118(1):376–383, 2013.

Chapter 6

Summary

This thesis presents the investigation of structural and electronic properties emerging at the interface with Au(111) surface by combined STM and XPS measurements. The research work has involved three important fields of surface science.

Chapter 3 was dedicated on the study of charge transfer in different supramolecular structures obtained by intermixing of organic acceptor TCNQ molecules with two different donor species: metallic iron atoms and TTF molecule. TCNQ is considered essentially neutral on the Au(111) surface and the peak on N_{1s} centered at 398.9 eV can be taken as reference. The addition of Fe atoms on Au(111) surface precovered with TCNQ monolayer leads to the formation of 2D-MOCN, in which one Fe atom is coordinated to four nitrogen atoms in rectangular unit cell. The binding energy of N_{1s} lowers to a value of 398.4 eV while Fe_{2p} shows a shift of about 4 eV towards higher binding energy indicating a +3 oxidation state. Accordingly to the structural model, only a part of the electrons that Fe centers are able to supply are transferred to TCNQ molecules, the remaining electrons are probably dispersed into gold substrate. The other donor specie is the organic molecule TTF which exhibits a strong interaction with Au(111) surface. The intermixing with TCNQ leds to mixed phases with different stoichiometries depending on relative concentration of both molecules. Here we studied in detail the TCNQ 1:1 TTF phase, where the N_{1s} shows a larger shift to lower binding energy up to 397.9 eV, while the S_{2p} remains almost unaltered. The mechanism that we proposed is that TTF molecules act as a kind of bridge between gold substrate and TCNQ molecules, since the latter are not able to obtain directly electrons from the substrate. Moreover we give a

further experimental confirmation to similar works that observed Kondo effect in TTF-TCNQ on Au(111) surface, which implies an unpaired electron localized in a π orbital of the TCNQ molecule. A comparison between the same TTF and TCNQ molecules on different substrates seems to indicate that the interaction with the surface is predominant with respect to Donor-Acceptor interactions. In other words, independently from the individual character (donor or acceptor) of the single building blocks, the molecules that less strongly interact with the surface are more able to receive and host electrons from the surface itself.

In the chapter 4 we studied the pseudomorphic growth of iron thin films on natural templated Au(111) surface. Fe atoms are trapped in the elbows of the herringbone reconstruction undergoing to a place exchange with Au atoms of the surface and consequently act as a nucleation site, leading to creation of preferential nucleation sites. For low deposition rate (R=0.02 ML/min), the Fe islands literally push away the reconstruction and then, when coverage increases, the dislocation lines result incorporated into the islands, resulting a perturbed reconstruction due to the defects that Fe atoms, included into the surface, represent. On the other hand, when the deposition rate increases, the kinetic effects appears to be predominant and no inclusion of dislocation lines neither distortion of the underlying herringbone reconstruction has been observed. As a consequence the growth of Fe proceed on a natural templated substrate leading to the formation of nano-strips along the $[11\bar{2}]$ directions. It follows the coalescence along $[1\bar{1}0]$ directions leading to a quasi layer-by layer growth. The pseudomorphic growth with underlying substrate is maintained up to few layers when the accumulated strain cannot be accommodated anymore and then the transition from fcc to bcc occurs. The morphology of thin films can be modified performing annealing experiments. At low annealing temperatures, the intermixing between Fe and Au is favored in the topmost layer, leading to the disappearence of islands in second layer and to drastic changes in the herringbone reconstruction. At higher temperatures, the interbulk diffusion is activated leading to a progressive disappearance of Fe atoms from surface and to the reappearance of regular herringbone reconstruction. On the other hand we can observe a modification of the behavior of iron on Au(111) in presence of a monolayer of TCNQ, organic acceptor molecule. Up to θ_{Fe}=0.18 ML no growth of iron islands occurs because cyano groups act as diffusion traps for iron atoms better than elbows of the herringbone reconstruction. At higher coverages, Fe atoms start to nucleate around one of the equivalent Fe center involved in the coordination. The free diffusion length of the impinging iron atoms is therefore reduced and this leads to smaller islands with higher surface density. Additional kinetic energy do not favour the coalescence between islands

but active the interbulk diffusion that does not result altered.

In the chapter 5 we studied the transposition on surfaces of two very common and very powerful reactions in gas phase: the polyester condensation and the azide-alkyne 1,3-dipolar cycloaddition. About the polyester condensation we proved that is possible design on surface a large and extended Surface Covalent Network Frameworks (SCOF) through the reaction of acylchlorides and alcohols groups. In the case of azide-alkyne Huisgen cycloaddition, the degradation of azide group and homo-coupling between alkyne groups makes impossible the efficient application of this strategy, even on the less reactive noble surfaces Au(111).

In summary, the works presented in this thesis show the fundamental role that interactions with metallic interface play in different fields of surface science. We proved, in fact, that Au(111) surface plays an active role in the modification of structural, electronic and catalytic properties of organic and hybrid structures.

Conclusiones Generales

Esta tesis presenta una disertación sobre la investigación de las propiedades estructurales y electrónicas en la interfaz con la superficie Au(111) mediante medidas con STM y XPS. El trabajo de investigación ha implicado tres importantes campos de la ciencia de las superficies.

El capitulo tres es dedicado al estudio de la transferencia de carga in diferentes estructuras supramoleculares obtenidas mesclando la molécula orgánica aceptora de electrones TCNQ con dos especies donoras de distintas natura: átomos de hierro metálicos y la la molécula orgánica donora TTF. El TCNQ se puede considerar básicamente neutra sobre la superficie Au(111) y el pico de N_{1s} a 398.9 eV se puede tomar como referencia. La adición de átomos de hierro en la superficie Au(111) pre-cubierto con una mono capa de TCNQ conduce a la formación de un 2D-MOCN, en el cual un átomo de hierro está coordinado a cuatro átomos de nitrógeno en una celda unitaria rectangular. La energía de ligadura del N_{1s} baja en 398.4 eV mientras el Fe_{2p} muestra un corrimiento de casi 4 eV hacia energías de ligadura más alta, indicando un estado de oxidación +3. En conformidad con el modelo estructural, solo una parte de los electrones que el hierro es capaz de suministrar son transferidos a la molÃ©culas de TCNQ. La remanente parte de los electrones está probablemente dispersa en el substrato de oro. La otra especie donora es la molécula TTF que enseña una fuerte interacción con la superficie Au(111). La mezcla con el TTF conduce a distintas fases mixtas con diferentes estequiometrias dependiendo de la concentración relativa de ambas moléculas. En esta tesis hemos estudiado en detalle la fase TCNQ 1:1 TTF, donde el N_{1s} muestra un corrimiento más grandes hacia energía de ligadura más baja hasta 397.9 eV, mientras el S_{2p} se queda casi en la misma posición. El mecanismo que proponemos mira al TTF que actúa como una especie de puente entre el substrato de oro y la moléculas de TCNQ, en cuanto la ultima no es capaz de coger electrones directamente del substrato. Además hemos fornido una comprobación experimental a trabajos

similares que han observado el efecto Kondo en TTF-TCNQ/Au(111), lo cual implica un electrón no pareado localizado en el orbital π de las molÃ©culas de TCNQ. Una comparación entre las mismas molÃ©culas TTF y TCNQ en distintos substratos parece indicar que la interacción con la superficie es predominante con respecto a las interacciones Donor-Acceptor. En otras palabras, independientemente del carácter individual (donor o aceptor) de cada uno de los *building block*, las molÃ©culas que meno fuertemente interactúan con la superficie son más capaces de recibir y acomodar electrones de la superficie misma.